

# DEVELOPMENT OF SPECIALLY SHAPED LASER BEAMS FOR THE OPTIMIZED ACCELERATION OF PARTICLES

Dissertation  
zur Erlangung des Doktorgrades  
der Naturwissenschaften

vorgelegt beim Fachbereich Physik  
der Johann Wolfgang Goethe-Universität  
in Frankfurt am Main

von  
Dipl.-Phys. Christian Gregor Brabetz  
aus Groß-Gerau



Frankfurt am Main, 2014

D 30

vom Fachbereich Physik der  
Johann Wolfgang Goethe-Universität als Dissertation angenommen.

Dekan: Prof. Dr. Joachim Stroth  
Gutachter: Prof. Dr. Oliver Kester  
Prof. Dr. Oliver Boine-Frankenheim  
Datum der Disputation: 13 Oktober 2014

---

# Contents

---

<b>1</b>	<b>Introduction</b>	<b>1</b>
<b>2</b>	<b>Theoretical background</b>	<b>7</b>
2.1	Laser beam shaping . . . . .	7
2.1.1	Laser beam diffraction . . . . .	8
2.1.2	Laser phase . . . . .	13
2.1.3	Laser aberrations . . . . .	15
2.2	Laser-driven ion acceleration in the TNSA regime . . . . .	20
2.2.1	Laser/electron interaction . . . . .	20
2.2.2	Relativistic self focusing . . . . .	23
2.2.3	Electron acceleration . . . . .	24
2.2.4	Target normal sheath acceleration - TNSA . . . . .	25
2.3	Ion acceleration with shaped laser beams . . . . .	28
2.3.1	Laser transport and focal spot simulation . . . . .	28
2.3.2	TNSA simulation . . . . .	31
<b>3</b>	<b>Beam properties of high-energy laser systems</b>	<b>37</b>
3.1	The laser system PHELIX . . . . .	37
3.2	Sources of aberrations in a laser system . . . . .	40
3.2.1	Pre-amplifier aberrations . . . . .	42
3.2.2	Main-amplifier aberrations . . . . .	42
3.3	Adaptive optics at PHELIX . . . . .	44
3.3.1	Shack-Hartmann wave-front sensor - SHS . . . . .	46
<b>4</b>	<b>The hollow laser beam</b>	<b>49</b>
4.1	Phase mask for hollow beam creation . . . . .	50

4.2	Hollow laser beam propagation . . . . .	52
4.3	On-shot focus diagnostic - OSFD . . . . .	56
<b>5</b>	<b>Results of TNSA experiments</b>	<b>61</b>
5.1	Magnetic electron spectrometer . . . . .	63
5.2	Radiochromic film - RCF . . . . .	66
5.2.1	RCF analysis software . . . . .	68
5.2.2	Proton energy spectrum reconstruction . . . . .	71
5.2.3	Proton envelope divergence . . . . .	73
5.2.4	Spectrally and spatially resolved proton particle profile with graphical deconvolution . . . . .	74
5.3	Ion acceleration with strongly astigmatic beams . . . . .	76
5.4	TNSA-dependency on focal spot geometry . . . . .	78
5.4.1	Proton energy dependence on laser intensity . . . . .	78
5.4.2	Proton energy scaling with target thickness . . . . .	80
5.4.3	Envelope divergence with different focal spot geometries and central proton intensities . . . . .	83
5.5	Ion acceleration with improved laser beam control . . . . .	85
<b>6</b>	<b>Conclusion</b>	<b>89</b>
6.1	Perspectives . . . . .	94

---

## Abstract

---

In the frame of this thesis laser-driven proton acceleration was studied within the target normal sheath acceleration (TNSA) regime with focus on control of the laser beam parameters to manipulate the generated proton beam. The experiments for this thesis were conducted at the PHELIX laser facility at the GSI Helmholtzzentrum für Schwerionenforschung GmbH. High intensity laser beams ionize atoms of the target, produce a plasma, and accelerate electrons through the target. On the rear side a strong electric field is generated and the strong charge separation leads to an acceleration of ions, mostly protons. The ions and electrons expand into the vacuum behind the target as a quasi-neutral plasma cloud. Such particle beams, originating from the target rear side contamination layer, have outstanding properties like ultra-low emittance and a pulse duration in the range of the laser pulse duration.

The goal of this work at hand was to change the initial conditions of the emitted ion beam from the TNSA source. The accelerated proton beam exhibit a large divergence angle. To reduce this up to  $60^\circ$  opening angle this work aims at shaping the rear side electron sheath using specially shaped laser beams. This can be done using specially designed helical phase plates. The result is a hollow focal spot on the target with an intensity minimum in the center. Therefore it was necessary to study and control the propagation of such a special laser beam through a complete laser amplification beam line. Numerical simulations were developed to assist identifying limitations on the laser beam quality and find possibilities for improvement.

Two successful experimental campaigns on laser-driven ion acceleration as well as one dedicated beam time for laser wave-front improvements were carried out during this thesis. The main diagnostic for generated protons within the conducted experiments were the radiochromic films (RCF). The analysis

## IV

software for these films was improved and new functions were developed to obtain two-dimensional energy-wise resolved particle numbers. Up to now it was assumed to have the same laser intensity distribution on the target as it was measured before a high-energy shot. Therefore, a new imaging system was implemented to image the real laser focal spot on target during the laser-matter interaction with a reasonable quality.

It was the first time that laser-driven ion acceleration with a hollow laser beam was experimentally demonstrated. The experimental data are in agreement with the simulations. Improvements on the laser-driven ion acceleration with shaped laser beams were demonstrated and compared to laser-driven ion acceleration with Gaussian focal spots. The initial proton beam parameter, the envelope divergence, was reduced by  $(3.07 \pm 0.42)^\circ$  or roughly 10 %. The scaling of the maximum proton energy  $E_{protons,max}$  with the square root of the laser intensity  $\sqrt{I_{laser}}$  was experimentally verified for experiments with a hollow laser focus. It appeared that the highest proton energies were achieved with the hollow laser beam exceeding 34.6 MeV. Also the dependency of the proton energy as well as the divergence angle on the target thickness was demonstrated within the thickness range of 5  $\mu\text{m}$  to 20  $\mu\text{m}$ . The study of the laser beam aberrations and the improvements made on it, resulted in the best ever achieved wave-front of the laser system, deduced from the reached maximum proton energies.

---

## Kurzfassung

---

Im Rahmen dieser Doktorarbeit wurde die lasergetriebene Protonenbeschleunigung im Bereich der TNSA (*target normal sheath acceleration*) untersucht, mit Schwerpunkt auf der Kontrolle der Laserstrahleigenschaften um den erzeugten Protonenstrahl zu beeinflussen. Die Experimente für diese Doktorarbeit sind an dem PHELIX Lasersystem der GSI Helmholtzzentrum für Schwerionenforschung GmbH durchgeführt worden. Hochintensitäts-Laserstrahlen ionisieren Atome eines Targets, erzeugen ein Plasma und beschleunigen Elektronen durch das Target. Auf der Rückseite wird ein starkes elektrisches Feld erzeugt und durch diese starke Ladungstrennung werden Ionen, hauptsächlich Protonen, beschleunigt. Die Elektronen und Protonen expandieren dann als quasineutrale Plasmawolke in das Vakuum hinter dem Target. Solche Teilchenstrahlen, die von den Verunreinigungen der Targetrückseite herrühren, haben herausragende Eigenschaften, wie z.B. besonders kleine Emittanz und Pulslängen die im Bereich der Laserpulsdauer liegen.

Das Ziel dieser vorliegenden Doktorarbeit war es die anfänglichen Eigenschaften des ausgehenden Ionenstrahl der TNSA Quelle zu beeinflussen. Der beschleunigte Protonenstrahl weist einen großen Divergenzwinkel auf. Um diesen bis zu  $60^\circ$  großen Öffnungswinkel zu reduzieren, zielt diese Arbeit auf die Formgebung der rückseitigen Elektronenschicht, mittels speziell geformter Laserstrahlen, ab. Diese können mit speziell entworfenen spiralförmigen Phasenplatten realisiert werden. Das Ergebnis ist ein ausgehöhlter Fokuspunkt auf dem Target mit einem Intensitätsminimum in der Mitte. Daher war es notwendig die Ausbreitung eines solch speziellen Laserstrahls durch ein komplettes Lasersystem zu untersuchen und zu kontrollieren. Numerische Simulationen wurden entwickelt, um bei der Identifizierung von Schwachstellen auf die Strahlqualität zu helfen und Möglichkeiten zur Verbesserung zu finden.

Zwei erfolgreiche Experimentkampagnen zur Ionenbeschleunigung mit Laserstrahlen und auch eine gesonderte Strahlzeit zur Verbesserung der Wellenfront wurden während dieser Arbeit durchgeführt. Die Hauptdiagnostik für die erzeugten Protonen während der Experimente waren radiochromatische Filme. Die Software zur Auswertung der Filme ist verbessert worden und neue Funktionen wurden implementiert um die energieaufgelösten, zwei-dimensionalen Teilchenzahlen zu erhalten. Bisher wurde angenommen, dass dieselbe Laserintensitätsverteilung bei einem Hochenergie-Experiment auf das Target trifft, als zuvor im Justagemodus gemessen wurde. Deshalb wurde ein neues Abbildungssystem eingebaut mit dem es möglich war, den realen Laserfokus während der Laser-Materie-Wechselwirkung mit guter Qualität zu messen.

Es war das erste Mal, dass Experimente zu lasergetriebener Ionenbeschleunigung mit einem Hohlstrahl durchgeführt worden sind. Die experimentellen Ergebnisse sind in guter Übereinstimmung mit den Simulationen. Verbesserungen der lasergetriebenen Ionenbeschleunigung mit geformten Laserstrahlen wurden nachgewiesen und mit Daten von Experimenten mit einem Gaußschen Fokusprofil verglichen. Der anfänglichen Protonenstrahlparameter, die Divergenz, konnte um  $(3,07 \pm 0,42)^\circ$  reduziert werden was ungefähr 10 % entspricht. Die Skalierung der maximalen Protonenenergie  $E_{protons,max}$  mit der Quadratwurzel der Laserintensität  $\sqrt{I_{laser}}$  konnte experimentell auch für Hohlstrahlen verifiziert werden. Es zeigte sich, dass die höchsten Protonenenergien bei Experimenten mit dem Hohlstrahl auftraten und 34.6 MeV überschritten. Auch die Abhängigkeit der Protonenenergie und des Divergenzwinkels von der Targetdicke konnten in einem Bereich der Targetdicken von 5  $\mu\text{m}$  bis 20  $\mu\text{m}$  demonstriert werden. Die Untersuchung der Laserstrahl Aberrationen und die dazugehörigen Verbesserungen, erzielten die bis dahin beste, jemals erreichte Wellenfront des Lasersystems, abgeleitet von den erreichten, maximalen Protonenenergien.



# CHAPTER 1

---

## Introduction

---

With the invention and the implementation of the chirped pulse amplification (CPA) scheme [1] it has become possible to construct laser systems delivering pulses in the petawatt ( $10^{15}$  W) regime. Focusing laser beams with these high powers down the smallest possible spot, the so-called Airy disk, which is in the size extent comparable to the laser wavelength, a focused intensity of  $10^{23}$  W cm $^{-2}$  can be reached. In reality, this limit is not easily hit and the intensities met nowadays in the laboratory reach between  $10^{21}$  W cm $^{-2}$  and  $10^{22}$  W cm $^{-2}$  at most. These high intensities open up wide areas of research in the field of laser physics, laser-plasma interaction fields (*High-energy physics*) [2, 3], and many other fields, e.g. studying astrophysical phenomena [4], which have been emerged since the invention of the first laser in 1960 [5]. The regime of intensities higher than  $10^{18}$  W cm $^{-2}$  is generally called the relativistic laser-matter interaction regime, because free electrons are accelerated to relativistic velocities by the laser field. The work at hand is embedded in this regime where the target normal sheath acceleration process takes place.

Already lower laser intensities (starting with  $10^9$  W cm $^{-2}$ ) generate a plasma on a solid matter target through ionizing and heating up of the surface. If this intensity is already exceeded by a pre-pulse or the amplified spontaneous emission (ASE), the main laser-pulse has to interact with this pre-plasma. The plasma expansion itself can accelerate particles to 100s of keV energy which can be understood in the frame of hot electron expansion [6]. Electron beams are emitted from the plasma due to the high electric fields of the laser [7, 8].

In addition to electrons heated up by the laser, beams of highly-energetic ions in the range of MeV were observed and first reported at the beginning of the last decade [2, 3]. The underlying mechanisms at play have attracted a lot of attention and are still subject of current research because of the unique properties of the accelerated proton beams. Indeed, such particle beams, originating from the target rear side contamination layer (mostly water), have an ultra-low emittance [9], contain up to  $10^{13}$  particles and have a pulse duration that is comparable to the laser pulse duration ( $\approx 1$  ps). All these features brought up ideas on application for the accelerated protons that range from e.g. serving as a diagnostic tool for the transverse proton probing of the acceleration itself [10], up to new compact particle accelerator schemes [11, 12].

In the current knowledge, the underlying processes at play in the high-energetic acceleration of ions can be summarized in the following way: Electrons are accelerated to high, relativistic energies by the laser field in the plasma at the target surface. They propagate through the target and form on the back side an electron sheath that is, compared to the laser-pulse duration, quasi-static. The so created electric field on the back side can reach several TV  $\text{m}^{-1}$  and is comparable to the impinging laser pulse's electric field. This leads to field ionization of the atoms of the target's backside and their acceleration. As the ions are accelerated normal to the target surface this mechanism is called the target normal sheath acceleration (TNSA). There are models that explain some of the basic properties of the target normal sheath accelerated protons [13, 14, 15], but due to its complexity it is not fully understood and no completely analytical model could be derived yet.

The conversion efficiency from laser to proton energy, to a certain extent, and the maximum proton energy scales with the laser intensity [16]. For short pulse laser systems (laser pulse duration  $\tau_L$  up to several ps) it follows a square root law, i.e.  $E_{\text{protons,max}} \propto \sqrt{I_{\text{laser}}}$ . This leads to the observation that most energetic laser systems, which reach intensities beyond  $10^{18} \text{ W cm}^{-2}$ , can accelerate protons up to energies of about 60 MeV [17]. The energy spectrum of laser-accelerated particles (in the range of  $10^{13}$  particles in total) usually decreases exponentially with increasing energy up to a cut-off energy. In addition, the divergence and the source size of the proton beams are also energy-

dependent and increase towards lower proton energies [18] up to a maximum of  $60^\circ$  for the divergence respectively some 100s of  $\mu\text{m}$  for the source size. The exponentially decreasing spectrum and the large divergence make the laser-accelerated protons hardly usable for further post acceleration [12]. Since not all characteristics of the acceleration mechanism are understood, it is difficult to create proton beams with controllable properties.

Until now several experimental teams have investigated the physical processes at play with various laser systems [15]. Besides varying the laser parameters (energy, intensity, contrast) to gain a deeper insight into the acceleration mechanism, there were studies that investigated different target thicknesses [19], various target materials, and also conditioned or specially coated targets [20]. In the current understanding of TNSA, the ion trajectories follow the direction of the electron density gradient at the rear surface of the target which explains the initial divergence of laser-accelerated ions. A particularly interesting idea, that links the shape of the electron sheath to the shape of the driving laser beam, was proposed and its proof of principle was made soon after [21, 22], when an astigmatic laser beam was used to create an elongated focal spot. This oblate focus is able to drive an ion beam with different opening angles showing that the electron distribution follows the laser intensity profile and can in turn influence the divergence of the ion beam.

These findings laid the foundations for the thesis at hand which addresses the reduction of the proton envelope divergence. This can be achieved using a modified laser focal spot geometry to drive the ion acceleration. Therefore a hollow focal spot is created, i.e. a ring shaped focus, on the target front side. Shaping the laser beam, using specially designed helical phase plates [23], to obtain a hollow focal spot is one cornerstone of this work. Studying the propagation of such a laser beam and the influence of aberrations on it is important to enable the laser-driven ion acceleration with this special kind of focus. The electron sheath in turn is influenced by the shape of the laser beam. With the ring focus the shape of the electron sheath of the TNSA is modified in a way to reproduce a flat sheath shape. This designed electron sheath would reduce the proton beam envelope divergence. To measure and characterize the properties of the TNSA proton beam is the other cornerstone of this thesis.

Improving the initial parameters of a laser-accelerated ion beam would ease the usage of these ions for other applications mentioned above. Most of the applications have to be placed at some distance from the ion source, either due to the electromagnetic pulse of the laser-matter interaction or to be able to select specific energies from the continuous energy spectrum. To cover large distances with the ion beam, one has to collimate or focus it for the application, otherwise nearly the whole beam will be lost due to the large (up to  $30^\circ$ ) half opening angle.

The LIGHT (**L**aser **I**on **G**eneration, **H**andling and **T**ransport) project, a collaboration that includes several German university institutes and Helmholtz centers [12], created the environment for a experimental testbed located at GSI Helmholtzzentrum für Schwerionenforschung GmbH to investigate the feasibility of transporting laser-generated ions and matching them into conventional accelerator structures. During the time of this thesis the LIGHT laser and proton beam line was installed and commissioned. It consists of a laser-driven ion source, a pulsed solenoid for energy selection and collimation, and a RF cavity for ion beam phase manipulations. It is designed to deliver a ns long proton pulse around 10 MeV with up to  $10^{10}$  particles and currently allows the transport over a distance of about 4 m. Within this project, the performance of this beam line, i.e. the capture efficiency of the pulsed solenoid, is limited by its spatial dimensions and distance to the source. While reducing the ion beam divergence utilizing the laser-driven ion acceleration with shaped laser beams, more particles could be captured within the solenoid and increase the efficiency of this beam line as well as the ion bunch intensities.

In this manuscript, chapter 2 describes the underlying theoretical background of the work: the topic of laser-driven ion acceleration and laser beam shaping. The basics of laser beam propagation and laser beam shaping are presented with a short excursion to laser beam aberrations. Afterwards, the essential relativistic laser-matter interactions are described and the used ion acceleration mechanism, the target normal sheath acceleration, is explained. Both topics are then brought together to the introduction of ion acceleration with shaped laser beams and are consolidated with simulations. In chapter 3 the laser system PHELIX is introduced. Special emphasis is made on the laser

beam aberrations occurring in such a large laser system as well as ways to reduce and control the aberrations with adaptive optics.

The experiments that were conducted in the frame of this thesis are described in chapter 4 and 5 along with the used diagnostics in the experiments. Chapter 4 is concentrated on the laser side of this work: the characterization of the phase masks that are used to create the hollow laser beam, the laser beam propagation itself, and the on-shot focus diagnostic. In turn the chapter 5 contains the results on the laser-driven ion acceleration. This chapter also covers the used detector for the laser-accelerated protons, the radiochromic films. As the analysis of this detector is only practicable with computers, the software developed and used for this purpose is explained in more detail. The thesis finishes with a conclusion and outlook towards further ion acceleration experiments with shaped laser beams.



# CHAPTER 2

---

## Theoretical background

---

This chapter is divided into three parts. The basics of laser beam propagation and the effects of aberrations on a laser beam are covered in the first part. The Kirchhoff integral theorem is introduced and the equality of the Fraunhofer approximation (far field), the electric field distribution in the focal plane of a lens, and the Fourier transform of the source field are illustrated. Thereafter the principle of laser-driven ion acceleration and related mechanisms are explained. The mechanism of the target normal sheath acceleration (TNSA) is described as well as some basics in electron acceleration. The electron acceleration is important for the TNSA mechanism to work, because the electrons transfer a part of their energy to the ions. This two-step acceleration of ions is necessary, since the laser field cannot accelerate the ions directly because this would require laser intensities beyond  $10^{24} \text{ W cm}^{-2}$ . The third part brings the TNSA together with the laser spatial phase modeling and lays the cornerstone for the thesis at hand. Simulations with shaped laser beams are presented as well as simulation on laser transport in presence of aberrations for the hollow beam.

### 2.1 Laser beam shaping

In this section the basic properties of the propagation of laser light are explained. Diffraction of laser light can be described within a formalism known as the Kirchhoff integral theorem and the more generalized Collins integral.

The equality of the Fraunhofer approximation (far field), the electric field distribution in the focal plane of a lens, and the Fourier transform of the source field are demonstrated and follow the explanation in [24]. Gaussian beam properties are derived, phase terms applied, and the far field is studied. This section concludes with an introduction to laser aberrations and their influence on propagation and focusing.

### 2.1.1 Laser beam diffraction

The electric field of a laser is described by the Maxwell equations. The derived wave equation from a particular case of the Maxwell equation (no free charges, no current) in scalar approximation is [25, 26, 27]

$$\left( \frac{\partial^2}{\partial x^2} + \frac{\partial^2}{\partial y^2} + \frac{\partial^2}{\partial z^2} - \frac{1}{c_n^2} \frac{\partial^2}{\partial t^2} \right) E(x, y, z, t) = 0 \quad (2.1)$$

with  $E(x, y, z, t)$  being the electric field and  $c_n = c/n$  is the speed of light in a medium ( $c$  vacuum speed of light,  $n$  refraction index). A solution of the wave equation is a plane wave traveling in  $z$  direction

$$E(z, t) = E_0 \exp [i(\omega t - kz)]. \quad (2.2)$$

$E_0$  is the field amplitude,  $\omega = 2\pi\nu$  the angular frequency ( $\nu$  is the frequency), and  $k = 2\pi/\lambda$  stands for the wave number ( $\lambda$ : wavelength). Points of maximum field are given by  $\omega t - kz = 2m\pi$  ( $m$  an integer) and define equiphase surfaces, spaced by  $\lambda$ . The same is true for another solution of the wave equation yielding the spherical wave

$$E(r, t) = \frac{E_0}{r} \exp [i(\omega t - kr)] \quad (2.3)$$

with  $r$  denoting the distance to the origin.

With a given electric field in a certain area and time it is possible to calculate the propagation in space and time by the wave equation. The propagation of the finite electric field into space or in presence of an obstacle is called diffraction. In the following some relations for propagation are derived from the ideally plane or spherical wave.

Following Huygen's principle an electric field  $E(x, y, 0)$  on a surface prop-



agates into space in such a way that each point on the surface can be seen as the source of a spherical wave. At a point  $P(x, y, z)$ , away from the surface, the resulting electric field is the superposition of all assumed spherical waves. Thinking of  $N$  starting points for the spherical waves the summation yields [24]:

$$E(P) = \sum_{i=1}^N E_i(P) = C \exp[i\omega t] \sum_{i=1}^N E(x_i, y_i) \frac{\exp[-i k r_i]}{r_i} \cos(\theta_i) \delta x \delta y \quad (2.4)$$

with  $r_i$  being the distance from the starting point to the point  $P$  and angle  $\theta_i$ ,  $\delta x \delta y$  is the point spacing,  $C$  a constant and  $\cos(\theta_i)$  accounting for maximum energy flow normal to the surface and zero for tangential directions. Following this empirical assumption further to the limit of  $N \rightarrow \infty$ , one gets the same results as mathematically derived [25, 28]

$$E(P) = \frac{i}{\lambda} \exp[i\omega t] \int_A E(x, y, 0) \frac{\exp[-i k r]}{r} dA. \quad (2.5)$$

This integral is the so-called Kirchhoff integral. The paraxial approximation  $\cos(\theta_i) = 1$  is incorporated in this solution, as well as the assumption that the surface  $A$  is much larger than the wavelength  $\lambda$ . With the Kirchhoff integral some simple and common diffraction geometries can be calculated, e.g. the diffraction of a circular aperture with a homogeneous illumination. Additional limitations to the geometry yield the Fresnel and Fraunhofer approximation which are used to calculate the near and far field diffraction pattern. In the Fraunhofer approximation (large distance  $L$  to the aperture compared to its extend  $a$ ) the resulting electric field  $E_2$  can be calculated with its source field  $E_1$  and the Kirchhoff integral reads as

$$E_2(\theta_x, \theta_y) = i \frac{a^2}{\lambda L} \exp[-i\Phi] \int_{-1}^1 \int_{-1}^1 E_1(x_1^*, y_1^*) \exp[i k (a\theta_x x_1^* + a\theta_y y_1^*)] dx_1^* dy_1^*, \quad (2.6)$$

the far field distribution. Therein are the angular coordinates  $\theta_x = x_2/L$  and the normalized coordinates  $x_1^* = x_1/a$  ( $y$  respectively) and  $\Phi = kL + (x_2^2 + y_2^2)/(2L)$  replaced. Studying only free space propagation does not help understanding and constructing real laser systems. Generalizing the Kirchhoff

integral to account for optical elements in terms of matrix optics [26] leads to the Collins integral [24, 29] representation

$$E_2(x_2, y_2) = \frac{i}{\lambda B} \exp[-i k L] \int \int E_1(x_1, y_1) \cdots \exp \left[ -i \frac{\pi}{\lambda B} (A x_1^2 + D x_2^2 - 2 x_1 x_2 + A y_1^2 + D y_2^2 - 2 y_1 y_2) \right] dx_1 dy_1 \quad (2.7)$$

with elements  $A, B, D$  of the ray transfer matrix  $M$ .

The ray transfer matrix analysis (also known as ABCD matrix analysis) is a technique around a ray transfer matrix  $M$  in the geometrical optics to describe optical systems. By multiplying the laser beam (represented as a vector) with a matrix of an optical element, the change in the path of the laser beam can be calculated. It is valid in the paraxial approximation. It maps the input parameters of the laser in the input plane,  $x_1$  the distance from the optical axis and  $\theta_1$  the angle with the optical axis, to the output plane parameters  $x_2$  and  $\theta_2$  via matrix multiplication. This is expressed with a ray transfer matrix  $M$  and its elements  $A, B, C, D$  as

$$\begin{pmatrix} x_2 \\ \theta_2 \end{pmatrix} = \begin{pmatrix} A & B \\ C & D \end{pmatrix} \begin{pmatrix} x_1 \\ \theta_1 \end{pmatrix}. \quad (2.8)$$

The determinant of the ray transfer matrix is the ratio of the input  $n_1$  and output  $n_2$  refraction index of the medium where the beam starts and ends as  $\det(M) = AD - BC = n_1/n_2$ . Two simple examples of a ray transfer matrix are given by

$$M_d = \begin{pmatrix} 1 & d \\ 0 & 1 \end{pmatrix} \text{ and } M_r = \begin{pmatrix} 1 & 0 \\ 0 & \frac{n_1}{n_2} \end{pmatrix}. \quad (2.9)$$

$M_d$  is the matrix for a free space propagation over a distance  $d$  and  $M_r$  represents the refraction at a flat surface.

The next step is calculating the field distribution  $E_2$  at the focal plane  $f$  of a lens with a given field  $E_1$  at the distance  $d$  from the lens. The ray transfer matrix elements for this propagation are  $A = 0$ ,  $B = f$ ,  $D = 1 - d/f$  and the

Collins integral reads as

$$E_2(\theta_x, \theta_y) = i \frac{\exp[-i k \delta]}{\lambda f} \int_{-\infty}^{\infty} \int_{-\infty}^{\infty} E_1(x_1, y_1) \exp[i k(\theta_x x_1 + \theta_y y_1)] dx_1 dy_1 \quad (2.10)$$

with  $\delta = d + f + 1/2(\theta_x^2 + \theta_y^2)(f - d)$  and  $\theta_x = x_2/f$  ( $y$  respectively). Comparing (2.6) and (2.10) indicates that both integrals are equivalent. This means that the electric field of the Fraunhofer approximation can be measured at the focal plane of a lens (far field). Furthermore, in the case of  $d = f$ , the quadratic phase term in  $\delta$  vanishes and (2.10) corresponds to the exact Fourier transform of the field. Measuring the Fourier transform (in the focal plane of a lens) is enough to completely characterize the source electric field. Knowing about Fourier transformation properties, diffraction calculations are simplified if the electric field is represented by its Fourier transform (Fourier optics).

With the knowledge on how to calculate the changes of the electromagnetic field of a laser (amplitude as well as shape) as it propagates through optical systems, one can find special field solutions of the Collins integral. This special group of fields change only their field amplitude and lateral extent and preserve their shape, while propagating through an optical system. They are called self-similar or propagation invariant field distributions. Eigensolutions of the diffraction integral have these properties and hold the following relation with  $a, b$ , and  $\gamma$  are arbitrary scaling factors for lateral extend and amplitude respectively:

$$E_2(x_2, y_2) = \gamma E_1(ax_1, by_1). \quad (2.11)$$

The most well-known field distribution fulfilling this relation and which is a solution of the wave equation is the Gaussian field distribution

$$E_1(x_1, y_1) = E_0 \exp \left[ \frac{-i k}{2q_1} (x_1^2 + y_1^2) \right] \quad (2.12)$$

with a complex number  $q_1$ . Most laser resonators emit Gaussian beams [24, 25, 26, 30] since they are an eigensolution of the resonator (also called transverse electromagnetic mode TEM, in the ground state TEM<sub>00</sub>). The transformation

rule for Gaussian beams with ray transfer matrix method reads then

$$E_2(x_2, y_2) = \frac{E_0}{A - B/q_1} \exp \left[ \frac{-i k}{2q_2} (x_1^2 + y_1^2) \right] \quad (2.13)$$

with the beam parameter  $q_2 = (q_1 A + B)/(q_1 C + D)$  calculated with the ray transfer matrix  $M$ .

A Gaussian beam stays a Gaussian beam as it propagates throughout a system, only the amplitude and transverse size change, a property which is called propagation invariant. In the following, some properties of a real Gaussian distribution are explained as it propagates through optical elements. The simplest distribution with a beam waist  $w_0$  at  $z = 0$  is

$$E_1(x_1, y_1) = E_0 \exp \left[ -\frac{(x_1^2 + y_1^2)}{w_0^2} \right] \quad (2.14)$$

yielding  $q_1 = i\pi w_0^2/\lambda = iz_0$ . The beam parameter  $q(z)$  changes according to the ray transfer matrix [24, 26] for a free propagation over a distance  $z$ :

$$\frac{1}{q(z)} = \frac{1}{R(z)} - \frac{i\lambda}{\pi w(z)^2}. \quad (2.15)$$

Therein,  $R(z)$  can be written as  $R(z) = z(1 + z_0^2/z^2)$  the radius of curvature of the phase front and  $w(z) = w_0\sqrt{1 + (z/z_0)^2}$  the  $1/e$  beam radius with respect to the on-axis value. Then the Gaussian beam at a distance  $z$  reads

$$E_2(x_2, y_2) = \frac{E_0}{1 - iz/z_0} \exp \left[ -\frac{ik(x_2^2 + y_2^2)}{2R(z)} \right] \exp \left[ -\frac{x_2^2 + y_2^2}{w(z)^2} \right]. \quad (2.16)$$

$z_0$  is the Rayleigh range (also depth of field or confocal parameter) and describes the distance from the minimal waist  $w_0$  to which the beam radius has increased by a factor of  $\sqrt{2}$ . For distances  $z \gg z_0$  the beam radius approaches an asymptote with the divergence angle  $\theta = w_0/z_0 = \lambda/(\pi w_0)$  (see figure 2.1). The beam parameter product  $\theta w_0 = \lambda/\pi$  is a constant for a Gaussian beam and does not change by propagation. For a Gaussian beam the imaging condition is  $1/g + 1/b = 1/f + z_0^2/(z(z^2 + z_0^2 - zf))$ . The additional term, compared to geometrical optics, accounts for the different phase front propagation in the beam waist, where it is not spherical. One should note that if the waist of a

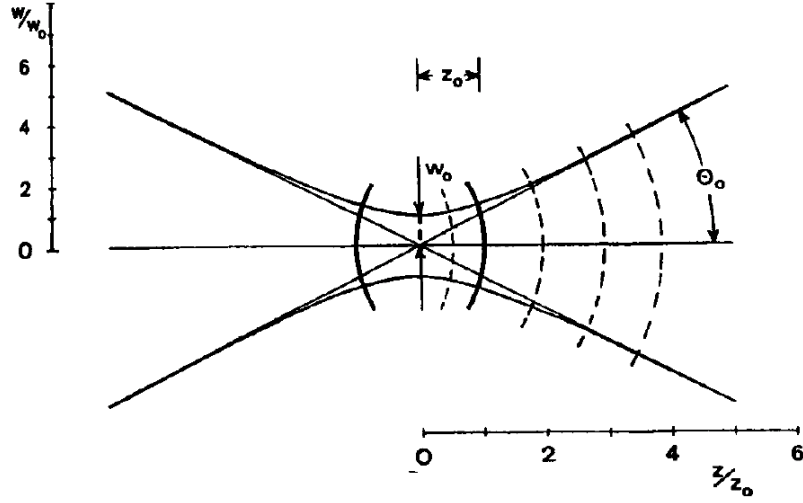


Figure 2.1: Free space propagation of a Gaussian beam.  $w_0$  is the point of the minimal waist and  $z_0$  indicates the Rayleigh range.  $\theta_0$  is the asymptote the laser beam approaches for large distances  $z$ . The picture is taken from [24].

Gaussian beam is located in the front focal plane  $z = f$  the image waist is found at the back focal plane, in contrast to geometrical optics. This is the cornerstone how image relay transport in a laser system works.

### 2.1.2 Laser phase

Since the Gaussian beam is a solution to the wave equation, a superposition of a Gaussian beam and an additional phase is still a propagation invariant. One special case is a Gauss-Laguerre beam which is a Gaussian beam with an additional helical phase. The electric field of a laser beam propagating along  $z$  with a  $LG_p^l$  mode is given by [24]

$$E_{pl}(r, \Phi) = E_0 \left[ \frac{\sqrt{2}r}{w} \right]^l L_p^l \left( \frac{2r^2}{w^2} \right) \exp \left[ \frac{-r^2}{w^2} \right] \exp [-i l \Phi] \quad (2.17)$$

with  $w$  the beam waist,  $r$  and  $\Phi$  the radial and azimuthal coordinates and  $L_p^l(x)$  the Laguerre polynomial of order  $l, p$  ( $l$  and  $p$  are the azimuthal and radial mode index). If in (2.17)  $l = p = 0$  then the Laguerre polynomial  $L_0^0(x) = 1$  and a Gaussian beam is obtained again. Although these modes can be produced

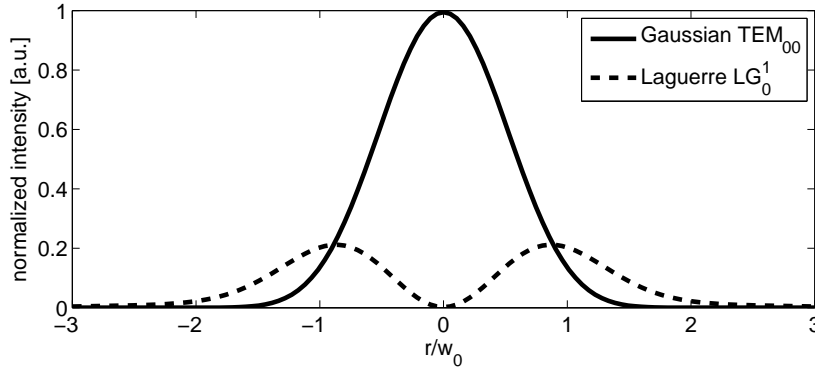


Figure 2.2: Transverse intensity profile of a Gaussian beam ( $\text{TEM}_{00}$ ), a Laguerre beam ( $\text{LG}_0^1$ ).

inside the cavity of a laser system [31], it was not desirable to work inside the cavity for this thesis. The cavity is the soft spot of the laser system. Changing the laser mode for one experiment would require a realignment procedure for subsequent experiments without the hollow beam. So another way of creating an LG beam was looked for and found [23] by adding the helical phase with a spiral phase element (SPE) after the cavity and obtain a Laguerre-Gaussian mode ( $\text{LG}_0^l$ ). The corresponding Laguerre polynomial in (2.17) is  $L_0^l(x) = 1$  for all values of  $l$ . In the recent years such beams with a continuous spiral phase were used for a variety of applications, e.g. trapping of atoms [32]. The intensity distribution of a LG beam is circular symmetric with an annular shape compared to the Gaussian beam intensity distribution illustrated in figure 2.2.

The transverse extent of a LG beam (depending on  $l$ ) is always larger than the  $\text{TEM}_{00}$ . Therefore, if the same energy assumed in both beams, i.e. the LG beam and the  $\text{TEM}_{00}$  beam, then the intensity of a LG beam is lower. The used SPE is an optical element that increases the refraction index with the azimuthal angle so that an incident Gaussian beam with a flat phase is emitted with a helical phase (figure 2.3). Due to manufacturing limitations the phase change is not smooth, but with fine enough steps it is not distinguishable from the diffraction limited one (a Michelson interferogram of such a phase is shown in figure 4.3).

The phase singularity (which depends on the azimuthal angle) in the center of such a LG beam leads to an intensity minimum. As the beam is propagation-

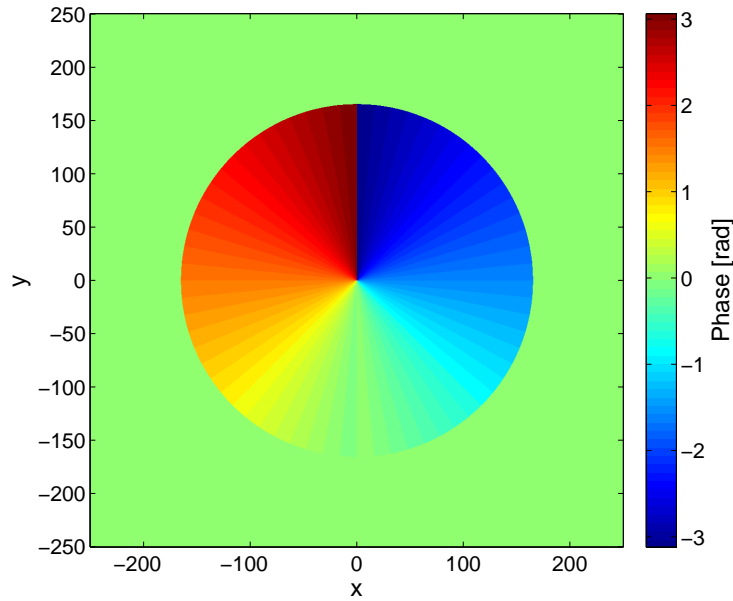


Figure 2.3: Phase profile of a Laguerre beam with  $l = 1$ .

invariant, the hole in the center can be observed in the near field as well as in the far field. In the ideal case the intensity profile in the focal plane is a perfect ring. As soon as wave-front aberrations (deviations from the ideal one) occur, the ring becomes distorted depending on the aberration strength.

### 2.1.3 Laser aberrations

Deviations from the ideal phase (the so-called aberrations) of a laser beam results in a focal spot quality that can be quite different from the diffraction limit. In addition, if the aberrations are not stationary as the beam propagates through an optical system, the propagation invariance of the beam is no longer guaranteed. This can lead to e.g. localized intensity spikes which can damage optical components. This is why the PHELIX laser system uses adaptive optics (see 3.3) to control the occurring aberrations.

As explained above, the focus profile can be understood as the Fourier transform of an input electric field. The far field (or the Fourier transform) of a homogeneous illuminated aperture resemble the best focus profile, that can be generated with a focusing optic, which is limited by diffraction. In the center a bright region, the so-called Airy disk, is created which is surrounded by

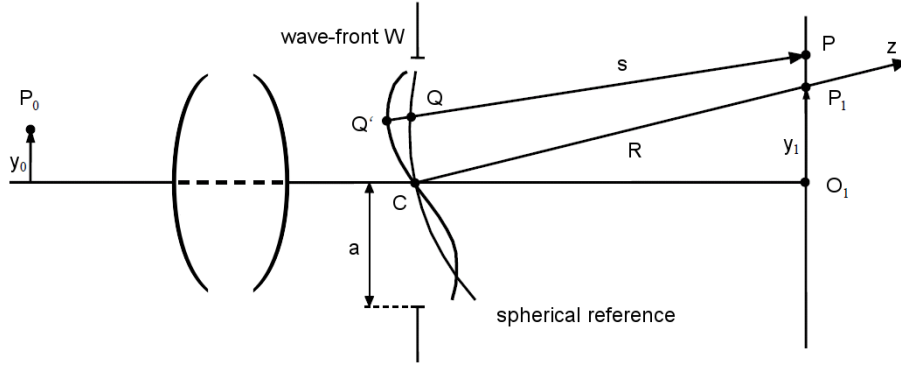


Figure 2.4: Reference system for discussion of aberration taken from [25].

rings of decreasing intensity (the so-called Airy pattern). This is the pattern with the highest achievable intensity in the center. Phase deviations lead to a transverse spread of the electric field in the Fourier transform and to a transfer of intensity out of the central part. A detailed explanation of this short summary of diffraction in presence of aberrations can be found in e.g. [25].

In figure 2.4 an optical system is given with the point source  $P_0$  and its image  $P_1$  along the  $z$  direction.  $C$  is the center of the aperture with radius  $a$ . The aberrated wave-front  $W$  in the aperture is given as reference sphere  $R$  and an aberration function  $\Phi$ , representing the occurred wave-front deformations through the system. An arbitrary ray  $s$  intersects the reference sphere in  $Q$  and the aberrated wave-front in  $Q'$ . Assuming a refraction index  $n = 1$ , the distance  $QQ'$  is the optical path difference (OPD) in  $Q$ .  $R$  is the curvature of the reference sphere. Then the disturbed field amplitude in  $Q$  can be calculated as  $\Delta E(Q) = E_0/R \exp [i k(\Phi - R)]$  with  $E_0/R$  the amplitude in  $Q$ . The field in  $P$  is given [25] as

$$E(P) = -\frac{i}{\lambda} \frac{E_0 \exp [-i k R]}{R} \int \int \frac{\exp [i k(\Phi + s)]}{s} dS \quad (2.18)$$

with the approximation of small angles and a constant amplitude  $E_0$ . Rewriting with the Gaussian reference sphere  $dS = a^2 \rho d\rho d\theta$  and the integration only



inside the aperture yields the intensity of  $W$  in  $P(x, y, z)$  as

$$I(P) = \left( \frac{E_0 a^2}{\lambda R^2} \right)^2 \left| \int_0^1 \int_0^{2\pi} \exp [i(k\Phi - v\rho \cos(\theta - \Psi) - 1/2u\rho^2)] \rho d\rho d\theta \right|^2 \quad (2.19)$$

with the aperture coordinates  $(\rho, \theta)$  and the image coordinates  $(r, \Psi)$ . Therein is  $u = 2\pi/\lambda(a/R)^2 z$  and  $v = 2\pi/\lambda(a/R)\sqrt{x^2 + y^2}$ . If no aberrations were present, the maximum obtainable intensity would be

$$I^* = \pi^2 \left( \frac{E_0 a^2}{\lambda R^2} \right)^2. \quad (2.20)$$

Maybe one of the most used and simplest meaningful ways of expressing the effect of wave-front aberrations is the Strehl ratio  $S$ . It is the ratio of the peak focus intensities of an aberrated against a perfect wave-front  $S = I(P)/I^*$ . It is linked to the root-mean-square (rms) wave front error  $(\Delta\Phi)^2$  by the empirical approximation  $S \approx 1 - \left(\frac{2\pi}{\lambda}\right)^2 (\Delta\Phi)^2$  [33]. As the real Strehl ratio requires complex calculations, this approximation gives good results above an approximated  $S$  value of more than 0.3. This approximation implies that the Strehl ratio (i.e. the diffraction pattern) is independent of the nature of the aberration. But as the Strehl ratio gets smaller and the wave-front aberrations grow, the nature of the aberration becomes more significant. Different aberrations have different influence on the image quality and can be tolerated to a different strength.

Therefore to describe the wave-front, i.e. surfaces of the same phase in the beam, the Zernike expansion of a (circular) wave-front along with deviations will be introduced shortly. The Zernike polynomials  $Z_n^m(r, \theta)$  are one mathematical way to explore a continuous wave-front as a linear combination of orthogonal polynomials [25, 26, 34, 35]. They are widely used as their first terms correspond to the aberrations of geometrical optics (also Primary or Seidel aberrations), e.g. coma and astigmatism.  $Z_n^m(r, \theta)$  can be written as

$$Z_n^m(r, \theta) = R_n^m(r) \exp [i m\theta] \quad (2.21)$$

with a radial polynomial  $R_n^m(r)$  and an angular dependency  $\exp [i m\theta]$ . The

radial polynomials are defined as


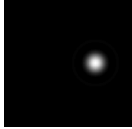

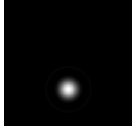
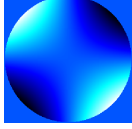
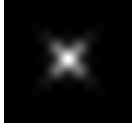
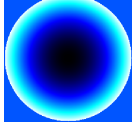

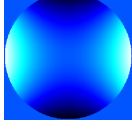

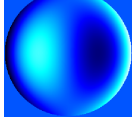

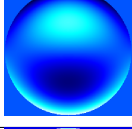
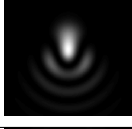
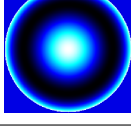
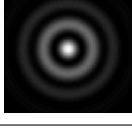
$$R_n^m = \sum_{k=0}^{(n-m)/2} \frac{(-1)^k (n-k)!}{k!((n+m)/2-k)!((n-m)/2-k)!} r^{n-2k}. \quad (2.22)$$

The first few Zernike polynomials are tabulated in table 2.1 along with their single index notation  $i$ . With this orthogonal set of polynomials which are normalized on the unit circle it is possible to write any arbitrary wave-front  $W$  as a sum of Zernike polynomials with a weighting factor  $Z_i$  (in units of  $\lambda$ ) as

$$W = \sum_n \sum_{m=-n}^n Z_i Z_n^m(r, \theta). \quad (2.23)$$

Lord Rayleigh was the first who thought about an upper limit for wave-front aberration that can be accepted without a great loss in image quality. This first limit (Rayleigh criterion) restricts the global wave-front distortion not to extend more than  $0.25 \lambda$  with a continuous, slow slope. Later definitions are more restrictive. The most conventional criterion [25], the diffraction-limited criterion, puts the limit down to  $1/14 \lambda$  (i.e. a strehl ratio of 0.8). The continuous, slow slope limit means, that no local jumps in the wave-front occur, as they could diffract light too far out of the beam axis. In specific, different types of aberrations have significantly different influences on the image quality. The upper boundaries for the Zernike coefficients  $Z_i$  calculated with the diffraction-limited criterion are [25]:  $Z_4 = 0.94 \lambda$  (spherical),  $Z_{7,8} = 0.60 \lambda$  (coma) and  $Z_{3,5} = 0.35 \lambda$  (astigmatism). In the following section the basics of laser-electron interaction along with the introduction of the laser-driven ion acceleration are explained.

Table 2.1: Common aberrations with Zernike polynomials

wave-front map	far field	Zernike index and polynomial				
		n	m	i	name	polynomial
		1	-1	1	tilt y	$r \exp[-i\theta]$
		1	1	2	tilt x	$r \exp[i\theta]$
		2	-2	3	45° astigmatism	$r^2 \exp[-2i\theta]$
		2	0	4	defocus	$2r^2 - 1$
		2	2	5	0° astigmatism	$r^2 \exp[2i\theta]$
		3	-1	7	coma y	$(3r^3 - 2r) \exp[-i\theta]$
		3	1	8	coma x	$(3r^3 - 2r) \exp[i\theta]$
		4	0	12	spherical	$6r^2 - 6r^2 + 1$

## 2.2 Laser-driven ion acceleration in the TNSA regime

In a simple picture, the laser pulse impinging on the thin target quickly ionizes its surface and transfers some of its energy to the electrons. In a second step, these hot electrons travel and recirculate through the target and in particular they accumulate at the target rear surface creating a charge separation and a quasi-static electric field. Last, light ions located in the vicinity experience this field and get accelerated. The energy transfer of laser energy to electrons and later on to the ions takes place inside a plasma. The plasma at the target front surface also has an effect on the incidence laser field itself. The laser self-focusing in the plasma allows to overcome the effect of diffraction of the beam within the plasma.

For a more detailed explanation one may refer to [36, 37, 38, 39, 40].

### 2.2.1 Laser/electron interaction

A linearly polarized, monochromatic, plane electromagnetic wave traveling in the direction  $z$  describes an ideal laser pulse:

$$\mathbf{E}(z, t) = E_0 \hat{\mathbf{x}} \exp[i(kz - \omega_L t)] \quad (2.24a)$$

$$\mathbf{B}(z, t) = B_0 \hat{\mathbf{y}} \exp[i(kz - \omega_L t)] \quad (2.24b)$$

with  $B_0 = E_0/c$  where  $E_0$  and  $B_0$  are the electric and magnetic field amplitudes,  $\omega_L$  the laser angular frequency,  $k = \omega_L/c = 2\pi/\lambda_L$  the laser wave vector (the speed of light  $c$ , the laser wavelength  $\lambda_L$ ) and  $\hat{\mathbf{x}}, \hat{\mathbf{y}}$  the unity vectors normal to  $\hat{\mathbf{z}}$ .

The dimensionless electric field amplitude  $a_0$  is a convenient quantity to determine if the laser-electron interaction becomes relativistic ( $a_0 \geq 1$ , i.e. laser intensity  $I_0 \approx 1 \times 10^{18} \text{ W cm}^{-2} \mu\text{m}^2$  for a laser with  $\lambda_L = 1 \mu\text{m}$  wavelength). It is defined as

$$a_0 \equiv \frac{eE_0}{m_e \omega_L c} = \sqrt{\frac{I_0 [\text{W cm}^{-2}] \lambda_L^2 [\mu\text{m}]}{1.37 \times 10^{18} \text{ W cm}^{-2} \mu\text{m}^2}} \quad (2.25)$$

wherein  $e$  is the electron charge and  $m_e$  the electron rest mass. With a ideal laser pulse the motion of a single electron can be described with the Lorentz force as

$$\frac{d\mathbf{p}}{dt} = -e(\mathbf{E} + \mathbf{v} \times \mathbf{B}) = -e \left( \mathbf{E} + \mathbf{v} \times \left( \frac{1}{c} \hat{\mathbf{z}} \times \mathbf{E} \right) \right) \quad (2.26)$$

with  $\mathbf{p} = \gamma m_e \mathbf{v}$  and  $\gamma = \sqrt{1 + p^2/(m_e^2 c^2)}$ . For an electron velocity  $v \ll c$  the effect of the magnetic component in (2.26) can be neglected and the electron performs an oscillation in  $x$ -direction. When the electric field  $E_0 = \sqrt{2I_0/\epsilon_0 c}$ , approach the relativistic limit, that means  $a_0 \geq 1$ , the electron velocity approaches  $c$  and the  $\mathbf{v} \times \mathbf{B}$  term in (2.26) is no longer negligible and leads to an additional drift of the electron along the laser beam direction. In reality, a laser pulse is neither monochromatic nor a wave perfectly plane and not infinitely long. It has a temporal and spatial profile in the form of a Gaussian (see section 2.1.1). This requires the change of the constant amplitudes  $E_0$  and  $B_0$  in (2.24) to time- and position-dependent amplitudes  $\hat{\mathbf{E}}(z, t)$  and  $\hat{\mathbf{B}}(z, t)$  that change slowly compared to a laser wave oscillation. In a first half-wave of the laser cycle an electron is accelerated outwards to a zone with reduced intensity. Thus, in the second half-wave the electron sees a smaller restoring force and therefore returns not to its initial position. This is the effect of the ponderomotive force  $\mathbf{F}_p$  that pushes the electrons out of a localized high-intensity zone and is given by

$$\mathbf{F}_p = -\frac{e^2}{4m_e\omega_L^2} \nabla(\mathbf{E} \cdot \mathbf{E}^*) = -\nabla\Phi_p \quad (2.27)$$

with the ponderomotive potential  $\Phi_p = a_0^2(m_e c^2)/(4\gamma^2)$  [41].

With the cycle-averaged relativistic gamma-factor  $\bar{\gamma} = \sqrt{1 + a_0^2/2}$  the ejection angle  $\theta$  of an electron can be calculated as

$$\tan^2 \theta = \frac{2}{\bar{\gamma} - 1}. \quad (2.28)$$

This concludes the motion of a single electron in vacuum with the presence of a laser field and allows to look at some collective effects of many electrons.

To ignite a plasma, an intensity of  $10^9 \text{ W cm}^{-2}$  is sufficient. This implies, as mentioned before, that already a pre-pulse or the amplified spontaneous emis-

sion (ASE) of a laser system is able to create a plasma at the target surface the incident laser interacts with. It is described as an inhomogeneous, iso-thermal expanding plasma with an exponential decay profile [36]. As described above, electrons are pushed out of regions of high intensity due to the ponderomotive force and this leads to a restoring force because of the electric field that is generated by the charge separation of electrons and ions.

This electric field, generated by the charge separation, is screened on a scale length  $\lambda_D$  the so-called Debye length, over which the plasma itself appears to be quasi-neutral

$$\lambda_D = \sqrt{\frac{\epsilon_0 k_B T_e}{n_e e^2}}, \quad (2.29)$$

with  $\epsilon_0$  is the permittivity of the vacuum,  $k_B$  being the Boltzmann constant,  $T_e$  is the electron temperature and  $n_e$  the density of plasma electrons. Driven by the external laser field the electrons are shifted in respect to the immobile ion background. The electrons start to oscillate about their rest position with the electron plasma frequency  $\omega_p$

$$\omega_p = \sqrt{\frac{e^2 n_e}{\bar{\gamma} m_e \epsilon_0}}. \quad (2.30)$$

As long as  $\omega_L > \omega_p$  the laser can propagate into the plasma. The critical density  $n_c$ , calculated with (2.30) and  $\omega_p = \omega_L$  to

$$n_c = \frac{\omega_L^2 \epsilon_0 \bar{\gamma} m_e}{e^2}, \quad (2.31)$$

defines the point at which the laser can not further propagate into the plasma, because the plasma refraction index (2.33) from this point on becomes imaginary. Thus the laser is reflected at the critical density surface  $n_c$  and can only penetrate evanescent deeper in the plasma where  $\omega_p > \omega_L$ .  $n_e < n_c$  defines the underdense plasma regime and  $n_e > n_c$  the overdense plasma regime. The exponentially evanescent length  $l_S$ , up to which the laser light can penetrate into an overdense plasma, is given by

$$l_S = \frac{c}{\sqrt{\omega_p^2 - \omega_L^2}}. \quad (2.32)$$

A laser pulse can propagate further into the plasma as  $\bar{\gamma}$  becomes larger (leading to a larger critical density). This is the effect of the relativistic transparency [42].

### 2.2.2 Relativistic self focusing

In the relativistic regime the electrons are expelled out of the the areas of higher laser intensities by the ponderomotive force, reducing locally the electron density. The refraction index  $n$  for the laser in a plasma can be calculated as [36]

$$n = \sqrt{1 - \frac{n_e}{n_c}} = \sqrt{1 - \frac{\omega_p^2}{\omega_L^2}}. \quad (2.33)$$

The electron density profile  $n_e$  and also  $\omega_p$ , that is defined by the incident laser, resemble in their shape a convex lens. On the laser axis a locally lower electron density results in a higher refraction index than in the regions off the laser beam axis. Since the laser beam can be assumed, in a simple image, to be cylindrical symmetric, this effect also has a radial symmetry which leads to a focusing of the laser pulse, the so-called relativistic self focusing [43, 44], sketched in figure 2.5.



Figure 2.5: Sketch of relativistic self focusing due to the ponderomotive force  $F_{NL}$  that pushes the plasma out and thus creating a localized lower plasma frequency  $\omega_p$  on the beam axis. This changes also the refraction index and acts as a convex lens that focuses the incident laser beam further. Picture taken from [39].

### 2.2.3 Electron acceleration

So far, only the relativistically relevant mechanisms have been taken into account, since the PHELIX laser system, where the experiments for this thesis were conducted, is in the regime of  $a_0 \geq 1$ . To accelerate electrons there needs to be an electric field component in acceleration direction and a defined phase relation between the incident laser field and the oscillation of the electrons. For intensities up to  $10^{18} \text{ W cm}^{-2}$  energy can be transferred from the laser to the electrons by the inverse Bremsstrahlung effect. But in the relativistic case, this effect plays a minor role [45]. The resonance absorption effect in a plasma excites plasma oscillations where  $\omega_L = \omega_p$  at the critical surface  $n_c$ . But this only holds, if the laser arrives under oblique incidence and in p-polarization, which means that there is an electric field component parallel to the plasma density gradient [46]. The not-so-resonant resonance absorption (also called Brunel effect or vacuum heating) is an efficient source of hot (MeV) electrons, if the plasma density gradient is very strong (small  $l_S$ ) [47, 48]. In this case, the displacement of electrons in the first half of a laser cycle is so strong that they are pushed into the vacuum and in the second half-cycle the electrons propagate deeply into the plasma where the laser can not follow because the laser is reflected at the critical density surface. But also this effect depends on oblique incidence along with p-polarization. To overcome these limitations one has to consider the highly intensity-dependent magnetic component of the Lorentz force, which is responsible for the drift explained above in connection with the ponderomotive force (2.26). The relativistic  $\mathbf{J} \times \mathbf{B}$  heating is a mechanism that depends on the high-frequency component of the Lorentz force [7]. Essentially, this relieves the constraint to p-polarization as the driving force is now the longitudinal  $\mathbf{v} \times \mathbf{B}$  force. As all these mechanisms are coupled to the laser field this results in a link between the laser intensity profile and the generated electron spatial profile at its source [49].

As the currently available laser intensities are not high enough for a direct ion acceleration (laser intensities  $I \geq 10^{24} \text{ W cm}^{-2}$  would be needed due to the larger mass of the ions) they have to gain their energy from the hot electrons accelerated by the mentioned heating mechanisms. The ion acceleration from the back side of the target is enabled by hot electrons penetrating through the



target and leave into vacuum on the rear side. Hot electrons are continuously produced as long as the laser pulse heats the target. A typically duration is  $\tau_L = 650$  fs for the laser beam used for this thesis. As they leave the target they produce a rear side charge separation sheath and the more electrons leave the target the stronger the field becomes. This intensifying field reinjects electrons back into the target. The electrons that reach again the front side can be accelerated again by the laser and gain additional energy. This is the so-called recirculation [50] which broadens the rear side electron distribution. Insulating materials dampens this effect and lead to a filamentation of the outgoing ion beam due to ionization instability. Thus conducting target materials are preferred as they have a smooth electron transport through the target [40].

The generated hot electron spectrum is assumed to follow a Boltzmann distribution [14, 51]:

$$n_e(E) = n_{e,0} \exp \left[ -\frac{E}{k_B T_e} \right] \quad (2.34)$$

with  $T_e$  the electron temperature and  $n_{e,0}$  the total number of electrons per unit volume. The overall electron number  $n_{e,0}$  can be assessed by  $n_{e,0} = \eta E_L / (c \tau_L \pi r_0^2 k_B T_e)$  with the laser energy  $E_L$  and  $r_0$  being the focal spot radius. The conversion efficiency  $\eta$  is intensity-dependent [52] and is given by  $\eta = 1.2 \times 10^{-15} I^{0.74}$  with a given intensity in  $\text{W cm}^{-2}$ . Hence for the PHELIX laser parameters  $n_{e,0} \approx 10^{13}$  hot-electrons are generated. For the assumed exponential spectrum the hot electron temperature, which can be seen as the mean energy, can be estimated by the ponderomotive potential [7, 41] to be

$$k_B T_e = \Phi_p = m_e c^2 \left( \sqrt{1 + a_0^2/2} - 1 \right). \quad (2.35)$$

#### 2.2.4 Target normal sheath acceleration - TNSA

As mentioned, the currently available laser intensities are not high enough for direct ion acceleration. Only nondirectional plasma expansion and electron-ion collisions generate somehow energetic ions on the front side (in the plasma). The electrons, that are accelerated in the forward direction through the target [53], field-ionize ions from the contamination layer at the back side and accelerate them in a direction normal to the target surface. The mechanism includes

an accumulation of the electrons at the rear side as shown in figure 2.6. This is the principle of the target normal sheath acceleration (TNSA) which is able to generate high-quality ion beams in terms of ion number, pulse duration, and directional propagation [13, 16]. The source of ion acceleration within TNSA is the electron sheath, the form and spatial distribution of the electrons define the proton beam properties. It was shown that the electron sheath has a transversal Gaussian density profile [9] and the electric force is normal to this density gradient. This leads to a radius-dependent electric field and an emission angle for all protons. In the center the protons are accelerated by a larger field to higher energies than protons on the rim. Proton energies up to 60 MeV have been reported as well as an ultra-low emittance that can be explained with the cold (at rest) starting conditions of the contamination ions [2]. The exiting divergence angle of the ions is depending on the created electron sheath which in turn is depending on the incident laser parameters, the generated plasma, and the target material itself (small-angle scattering) [54, 55]. As the target becomes thicker, the small-angle scattering dominates inside the target and thus smooths the electron spatial profile, and hence the outgoing ion beam. The source size of the proton beam is typically in the range of 100s of  $\mu\text{m}$  [2, 56] and the acceleration time can be deduced from, e.g. a fluid model to be approximately in the range of the laser pulse duration [14].

Following [14, 40], the built up potential  $\Phi$  by the electrons, given by the Poisson equation, that reach the target back side and leave the target, is in a one-dimensional case given as

$$\epsilon_0 \frac{\partial^2 \Phi}{\partial z^2} = en_e, \quad (2.36)$$

assuming that the target ( $z \leq 0$ ) perfectly shield the potential. With the electron density  $n_e$  (2.34) and replacing the electron kinetic energy  $E$  by the potential energy  $-e\Phi$  a solution to the Poisson equation can be derived. Then the maximum strength of the electric field created by the electron sheath on the target rear side at the target surface can be estimated to

$$E_{max} = \frac{\sqrt{2k_B T_e}}{\sqrt{e}\lambda_D} = \sqrt{\frac{2k_B T_e n_e}{e\epsilon_0}} \quad (2.37)$$

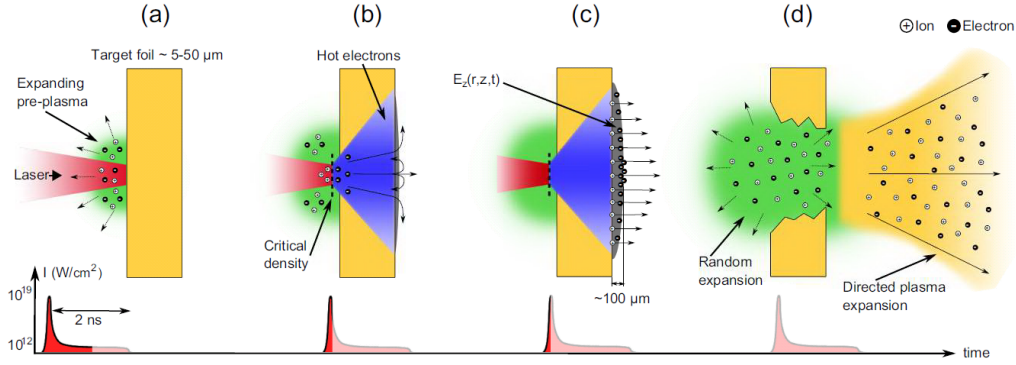


Figure 2.6: Schematic representation of the TNSA acceleration mechanism. (a) The laser pulse arrive from the left and has to interact with the ASE generated pre-plasma. (b) At the critical density the laser accelerates electrons into the target. (c) Electrons travel through the target and form at the rear side the strong electron sheath that field-ionize ions of the contamination layer. (d) The accelerated protons leave the target with the co-moving electrons in a quasi-neutral plasma cloud. The picture is taken from [57].

and reaches several  $\text{TV m}^{-1}$  [58, 40]. This initial field easily ionizes the ions on the back-side contamination layer [59], i.e. the protons, and is proportional to the electron number  $n_e$  and their temperature  $k_B T_e$ . While the proton beam expands into vacuum, energy is continuously transferred from fast electrons to the protons (due to the Coulomb force), thus leading to an kinetic energy matching of electrons with the ions. Therefore, a quasi-neutral plasma cloud is ejected from the target. The one-dimensional fluid model by *Mora* [14] predicts an exponential proton spectrum  $dN/dE = N_0 \exp[-E/(k_B T_e)]$  with a notable cut-off energy  $E_{p,max}$  of the protons and a broad energy distribution. A comprehensive overview of different theoretical models to describe the ion acceleration can be found in [60]. An empirical law is given by [61]

$$E_{p,max} \approx 10k_B T_e, \quad (2.38)$$

linking the electron temperature  $k_B T_e$  to the maximum (cut-off) proton energy  $E_{p,max}$ . After the acceleration due to the electric force and the plasma expansion it is assumed that the protons along with the co-moving electrons propagate ballistically [10].

TNSA efficiently accelerates protons, the lightest ions, with the generated

electrons and thus this thesis attempts to optimize proton beam parameters with respect to the initial electron source distribution and the generated electron sheath. Due to the fact that the laser is responsible for the heating of the electrons and the shape is linked to the electron sheath, in a next step it is necessary to understand the properties of laser beam shaping and its propagation. Therefore in the next section simulation results on laser beam propagation and laser-driven ion acceleration are presented.

## 2.3 Ion acceleration with shaped laser beams

Now we combine the knowledge of laser-driven ion acceleration, the dependency on the input parameters (e.g. laser intensity), and laser beam shaping to lay the cornerstone for the work at hand. In this section the particle-in-cell (PIC) simulations, done for this work, will be explained as well as the developed laser transport code based on section 2.1.

The influence of the laser focal spot shape on the outgoing TNSA particle beam was proposed and qualitatively verified by *Fuchs et al.* [21] in 2003. They irradiated a flat target foil with an elongated laser spot and detected a correspondingly elongated proton beam signature perpendicular to the major laser beam axis. In [62], one explains that defined pre-plasma parameters can change the ion beam properties, too. Later the target thickness as well as the laser spot dependency was demonstrated and measured in [63].

### 2.3.1 Laser transport and focal spot simulation

A laser simulation tool in MATLAB was developed by myself (based on section 2.1), in addition to the following simulations concerning the laser-matter interaction as well as the ion acceleration. Its goal was to study the impact of laser aberrations on the propagation of the hollow beam. As there is no analytic solution to the propagation of a laser beam with aberrations in an optical system, the problem is studied with numerical techniques [64, 65, 66] for solving the Kirchhoff integral at every propagation step. The previously demonstrated equivalence of the Fourier transform and the far field reduces most of the propagation to Fourier operations. That means a starting electric field distribution,

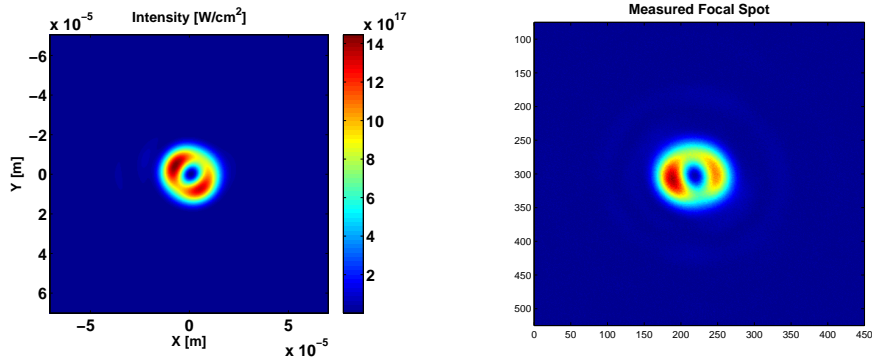


Figure 2.7: Left: Simulated far field distribution through the system with applied aberrations. Right: Measured far field distribution through the system up to the main-amplifier sensor.

with or without aberrations has to be Fourier transformed (normally done with the fast Fourier transform algorithms, FFT). Then a transfer function is applied (for the propagation) and with the inverse Fourier transform the new electric field distribution at the new position is obtained. Additional aberrations can be applied after each inverse Fourier transform where the spatial distribution is reconstructed (i.e. in the near-field planes). This is repeated for all optical elements under consideration until the end of the laser system. The last Fourier transform of the propagation code produce the electric field distribution in the focal plane on the target.

In figure 2.7, an example of such a simulation is given with measured PHELIX aberrations through the optical system. The simulation result (left) is in qualitatively good agreement with the measured far field distribution (right) and gave confidence that the propagation code works properly.

In figure 2.8 plotted as Strehl ratio, is the deviation from an ideal ring focus compared to a ring focus with aberrations. A similar definition of the Strehl ratio of section 2.1.3 was used, where here the intensity on the perfect ring is compared to the intensity on the same ring of the aberrated profile. A Strehl ratio of one means an ideal ring, and as the defocus and spherical aberration only changes the size of the focal spot it is negligible because the shape is nearly unchanged for these aberration strengths. Not rotational symmetric aberrations have a clear impact on the shape of the ring focus, e.g. astigmatism and coma aberration. It is even possible that some specific combination of

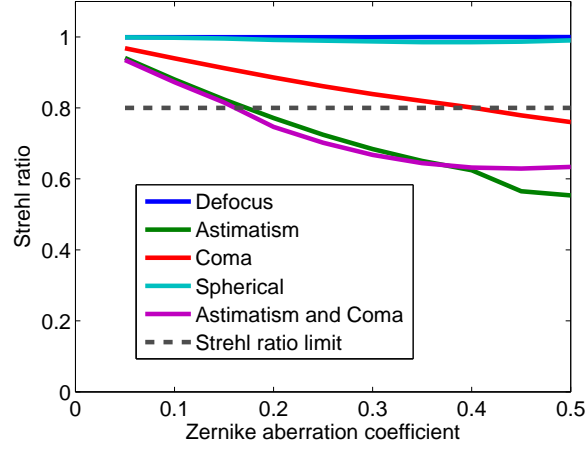


Figure 2.8: Strehl ratio of a ring focus with different aberrations. The purple line combines the same aberration strength for astigmatism and coma.

aberrations can balance each other (see purple line) and thus lead to a reduced effect on the ring. The limit for the aberration threshold was set to keep the deviation at least better than a Strehl ratio of 0.8 which was derived from the diffraction limited criterion for a Gaussian beam, but higher values are preferable. Observed in the figure can be that the most distorting aberration is the astigmatism. Therefore great effort was made on improving the wavefront of the PHELIX laser system (chapter 3 and 4). Some sample simulated images with aberrations are shown in figure 2.9.

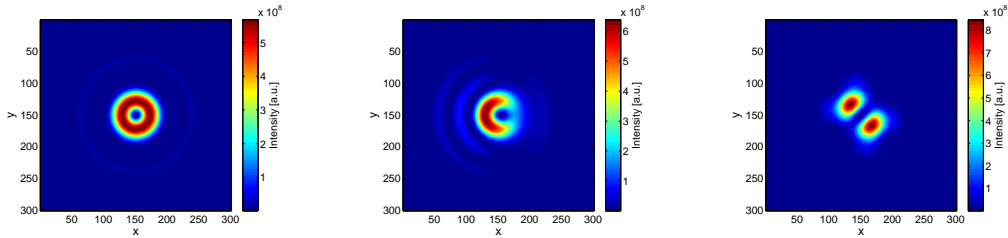


Figure 2.9: Simulated far field distribution for different aberrations. Left: Ideal ring focus. Center: Ring focus with applied coma aberration. Right: Ring focus with applied astigmatism aberration.

The simulation helped identifying the optical elements in the laser chain with the most impact on the hollow laser beam propagation and which needed to be improved (e.g. measurements of complete sub-systems in section 3.2 and hence resulting improvements see section 3.3). The next section deals with

TNSA simulation in presence of a hollow beam. Complete three-dimensional simulations are needed to include the laser beam aberrations. Since they are complex and time consuming they were beyond the scope of this experimental work. Therefore we restrict the the problem on two-dimensional simulations, i.e. a perfect hollow beam, to study the basic influence of shaped laser beams on the TNSA mechanism.

### 2.3.2 TNSA simulation

A first simplified simulation was performed by *T. Cowan et al.* based on the electron transport model developed in [21]. Figure 2.10 (a) shows the simulated electron sheath (sheath cross-section) in dependency on the annular focal spot size ( $R_{ann}$ ). It starts left with  $R_{ann} = 0$  which is equal to a Gaussian focal spot, to the right with increasing  $R_{ann}$  that represents different annular focal spot sizes. The figures 2.10 (b)-(d) show then the (rotational symmetric) electron sheath for a given strength of the annular focus  $R_{ann}$ . As the annular focus becomes larger the electron sheath changes from Gaussian (b) to flat (c) and final to an annular sheath (d). They are calculated with an ideal focal spot and a Gaussian point spread function ( $60^\circ$  FWHM) for the electron transport through an  $11\ \mu\text{m}$  thick gold target [21]. With these electron sheath configurations and fact that the accelerating force on the ions of the TNSA mechanism is normal to the electron sheath, possible proton beam profiles were calculated (figure 2.11). Essentially, the flat and annular electron sheath lead to a more directed proton beam of the TNSA and therefore reduce the initial divergence.

Based on these encouraging results, I performed several simulations with the particle-in-cell (PIC) method in 2D to investigate the parameters of the laser-driven ion acceleration with shaped beams for this work. The used PIC code was EPOCH-2D <sup>1</sup> which is based on the Plasma Simulation Code from *H. Ruhl* [67]. The PIC method solves equations (Lorentz force as particle mover, Maxwell equations for fields) and computes in parallel particle densities on a finite computational mesh allowing to follow trajectories of charged particles in self-consistent fields [68]. Because the simulation of large system

<sup>1</sup>Extendable PIC Open Collaboration project, <http://www.ccpp.ac.uk/home/index.html>

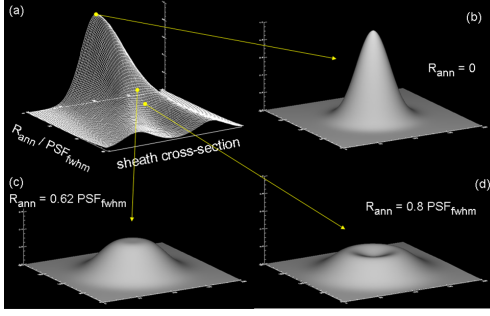


Figure 2.10: Electron sheath dependence on annular focus size. (b) is the predicted electron sheath with a Gaussian focal spot, while (c) and (d) show the electron sheath for two different annular focus sizes. Taken from *T. Cowan, 2010*.

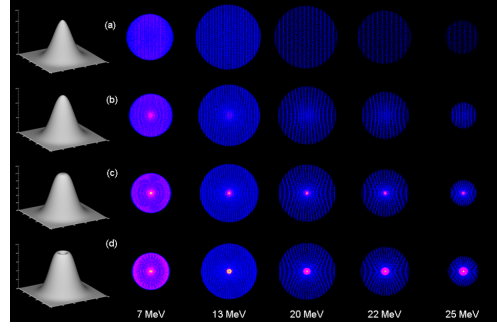


Figure 2.11: Simulated proton beam profile in RCF based upon the electron sheath predictions shown in figure 2.10. Taken from *T. Cowan, 2010*.

with real particle numbers is not possible nowadays, even with supercomputers, macroparticles are introduced in the simulation. They represent several thousands or millions of real particles (electrons, ions, etc.). The same holds true for the simulation volume and time frame, which is limited by computational space. In addition, the chosen grid and time step size have to properly resolve the problem, i.e. balance speed and accuracy of the simulation. A rule of thumb to resolve physics in a plasma, values for the grid size should be smaller than the Debye length ( $\delta x \leq \lambda_D$ ) and the time step have to resolve the plasma oscillation ( $\delta t \leq 0.2\omega_p^{-1}$ ) [69]. For a more detailed treatment of this rather large field one may refer to [70]. Typical parameters in the simulations performed for this work were e.g. grid size  $\delta x \approx 1 \mu\text{m}$ , time step  $\delta t \approx 1 \text{fs}$  and simulation box size of about  $0.01 \text{mm}^2$ . To simplify the simulation, an infinitely good contrast, i.e. no pre-pulse or ASE, was assumed, while the temporal pulse shape was a Gaussian. As the simulations were performed in 2D, effects of laser aberrations as described in the previous section, could not be modeled.

The simulations aimed at finding the proper target thickness for a given focal spot shape and laser parameters achievable at PHELIX. Additionally, they should ensure the above simplified simulation results, from the beginning of this section, with a higher level simulation code. By varying the target thickness in the simulation an optimum target thickness was found to be in



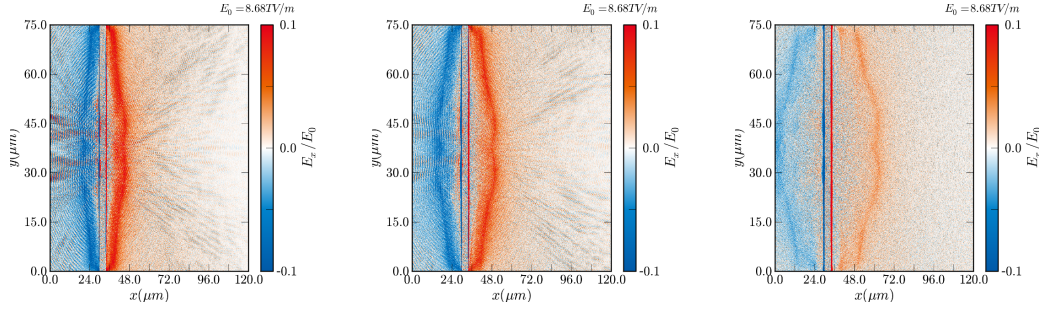


Figure 2.12: PIC simulation for the electrical field of an annular focus spot for a 4  $\mu\text{m}$  target. From left to right increasing time steps for the evolution of the electric field are shown.

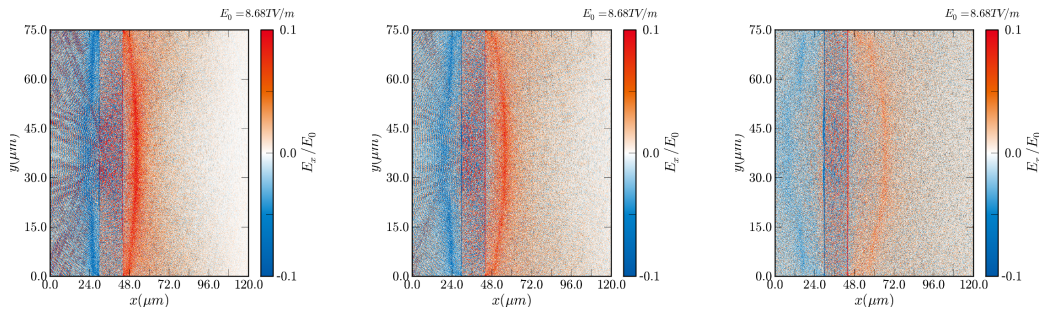


Figure 2.13: PIC simulation for the electrical field of an annular focus spot for a 14  $\mu\text{m}$  target. From left to right increasing time steps for the evolution of the electric field are shown.

the range of 14  $\mu\text{m}$  to 18  $\mu\text{m}$  for the focal spot sizes achievable at PHELIX. Optimum target thickness in this context means that the accelerating electric field becomes flat compared to the electric field of a Gaussian focal spot.

Figures 2.12 and 2.13 show two simulations for different target thicknesses (4  $\mu\text{m}$  and 14  $\mu\text{m}$ ) while the laser parameters ( $I_0 = 1 \times 10^{19} \text{ W cm}^{-2}$  and  $\tau_L = 650 \text{ fs}$ ) and annular focal spot (diameter 15  $\mu\text{m}$ ) were held constant. The laser comes in from the left border and hits the target located at  $x = 30 \mu\text{m}$ . The parameter depicted in the figures is the electric field strength along the laser propagation direction  $x$ . In the first simulation, the target thickness equals 4  $\mu\text{m}$ , which is clearly too thin, as it can be seen in the time evolution of the arising electric field (illustrations from left to right). The field resembles the hollow character of the incident laser field for different time steps (800 fs, 900 fs and 1150 fs). In contrast, the second simulation shows a well-chosen target thickness. The resulting field of the laser-matter interaction stays in the central part very flat for the different time steps. This results in the predicted,

more directed ion acceleration.

In figures 2.14 to 2.16 the accelerating electric fields of the TNSA with a hollow focus are shown again, but for a single time step (1150 fs) and various target thicknesses (15  $\mu\text{m}$ , 10  $\mu\text{m}$  and 5  $\mu\text{m}$ ). For comparison in figure 2.17 a simulation with a Gaussian focus on a 5  $\mu\text{m}$  thick target is also displayed. It can be observed that the shape of the electron sheath (the accelerating electric field) depends on the input laser shape and a well-chosen target thickness. Seen in figure 2.16, the accelerating electric field is not flat but resemble the impinging hollow laser profile. Switching to thicker targets in figure 2.15 and 2.14 the electron sheath, i.e. the electric field, approach a flat shape. Based on these simulation results, the optimum target thickness was derived to be in the range of 14  $\mu\text{m}$  to 18  $\mu\text{m}$  to reproduce a flat electron sheath. Incorporated are the PHELIX laser parameters with an intensity of about  $1 \times 10^{19} \text{ W cm}^{-2}$ , the pulse length of 650 fs, and a 15  $\mu\text{m}$  ring focal spot diameter. Not included in the simulation is the real contrast of the laser system, as told in the beginning to simplify and ease the simulation process. Therefore targets with proper thickness (in the range from 5  $\mu\text{m}$  to 20  $\mu\text{m}$ ) were ordered and the experiments (chapter 5) were prepared and conducted.

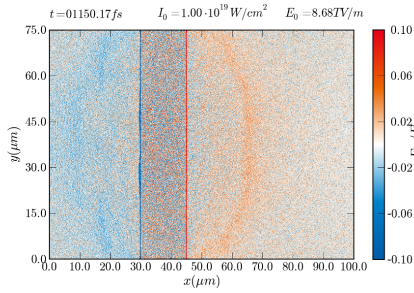


Figure 2.14: PIC simulation of an annular focus spot for the accelerating electric field with a 15  $\mu\text{m}$  target.

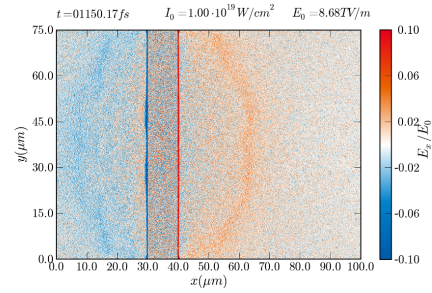


Figure 2.15: PIC simulation of an annular focus spot for the accelerating electric field with a 10  $\mu\text{m}$  target.

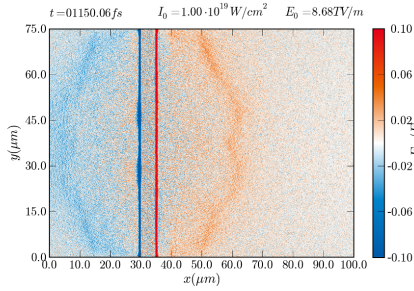


Figure 2.16: PIC simulation of an annular focus spot for the accelerating electric field with a 5  $\mu\text{m}$  target.

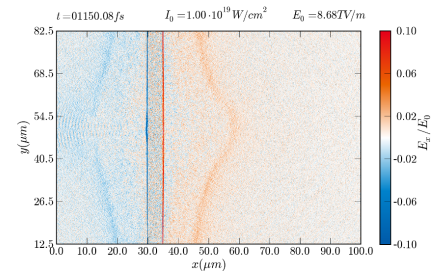


Figure 2.17: PIC simulation of a Gaussian focus spot for the accelerating electric field with a 5  $\mu\text{m}$  target.



## CHAPTER 3

---

### Beam properties of high-energy laser systems

---

The experiments for this thesis were carried out at the high-intensity high-energy laser system PHELIX (**P**etawatt **H**igh-**E**nergy **L**aser for heavy **I**on **E**xperiments) located at the GSI Helmholtzzentrum für Schwerionenforschung GmbH [71]. At first, the laser system itself is introduced with its different modes of operation. Generally, large scale laser systems like PHELIX need to work with large beam diameters to avoid damage on optics, i.e. keep the laser beam fluence below a damage threshold. Large diameter optics have to cope with distorting wave-front aberrations (both static and thermal) that lead to intensity losses at the experiment, in particular at the focus position. The origin of aberrations as well as measurements on aberrations are presented. The fact that aberrations lead to intensity losses made it necessary to develop and implement adaptive optics systems along with its control software [72]. A Shack-Hartmann sensor (SHS) measures the spatial phase of the laser and opens the possibility to correct for those aberrations with the newly implemented adaptive optic systems. The adaptive optics systems in operation are introduced and explained with their particular application.

### 3.1 The laser system PHELIX

The high-intensity high-energy laser PHELIX can be operated in combination with the heavy-ion accelerator UNILAC (**U**niversal **L**inear **A**ccelerator) at the Z6 experiment area or in laser-only mode. This combination at GSI

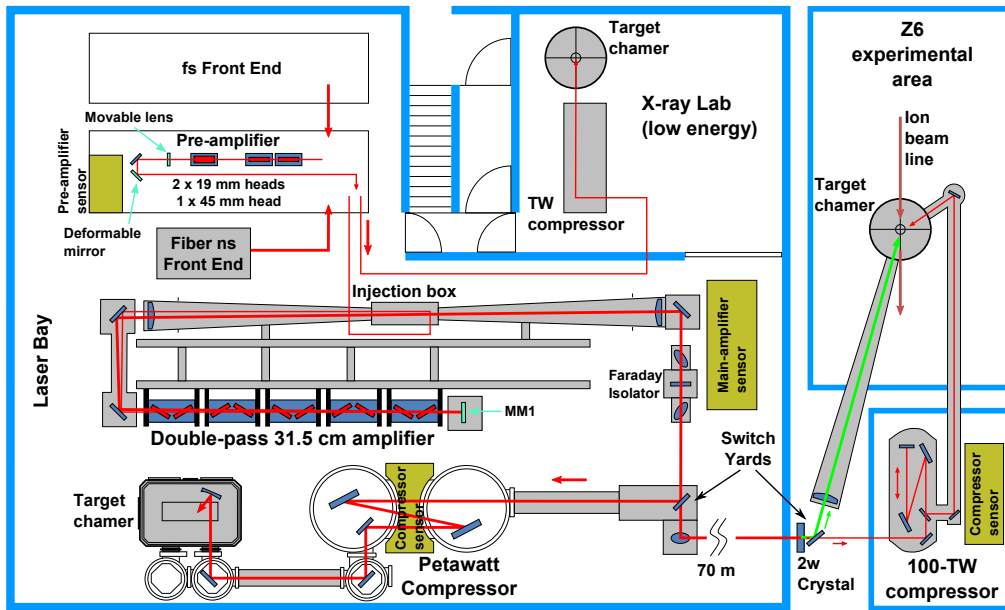


Figure 3.1: Schematic sketch of PHELIX. Currently three different experiment places can be operated by the laser. After the pre-amplifier a low energy mode can be selected and guided to the x-ray lab. Behind the main-amplifier a switch yard is used to direct the beam either to the in house, petawatt target area or to the Z6 experiment area where it can be combined with the UNILAC ion beam. Extra highlighted in olive are the laser sensors and in turquoise the active elements of the adaptive optics systems.

is unsurpassed worldwide and enables a large variety of unique experiments [71]. Applications of such a laser system range from laser-particle acceleration (key aspect of this work) [2, 3], secondary source development (coherent and incoherent X-ray radiation) [73, 74] to be used as high-precision ultra-fast diagnostics, and planetary science (warm dense matter studies) [75, 76] thanks to the ability to drive pump-probe experiments. A schematic sketch of the laser system and experiment areas is given in figure 3.1. Two independent laser front-ends can be amplified and deliver a short and/or a long pulse for experiments with a central wavelength of  $\lambda = 1054 \text{ nm}$ .

The ns front-end (ns-FE) is built around a gated cw fiber laser and generates the long pulse. It operates at 0.5 Hz in alignment mode and has a adjustable pulse duration between 1 ns and 20 ns. In addition, the temporal pulse shape can be controlled electronically with 1 ns resolution. After fiber based amplification the laser beam gets decoupled from the fiber. It is ampli-

fied in a flashlamp-pumped Nd:glass regenerative ring amplifier to energies of about 20 mJ. The long temporal pulses of the ns-FE allow for a maximum energy extraction out of the full system (after pre- and main-amplifier) of about 1 kJ of laser energy. After frequency doubling it is mainly used as a driver for various laser-driven plasma experiments like the experimental determination of the ion stopping-power of plasma or plasma-assisted nuclear physics in the Z6 area.

In contrast to the ns-FE the short pulse or fs front-end (fs-FE) is used for ion acceleration and x-ray experiments. It is based on the chirped pulse amplification (CPA) scheme [1]. As the name fs-FE indicates, it is used to achieve the highest intensities on target with a pulse duration of about 500 fs after pulse compression. It starts with a commercial laser oscillator (*Coherent Mira*) that creates 100 fs pulses with some nJ energy at a 72 MHz repetition rate. The pulses can either be injected first to an ultrafast optical parametric amplifier (uOPA) and then stretched or directly temporally stretched to 2.3 ns. That uOPA stage is used to generate the highest contrast pulses available at PHELIX with a contrast of up to  $10^{-11}$  [77]. Thereafter, the pulses pass two Ti:sapphire (titanium-doped sapphire) amplifiers with a repetition rate of 10 Hz and exit the fs-FE with nearly 20 mJ of energy.

After either front-end follow the pre-amplifier that consists of three Nd:glass (neodymium-doped glass) flashlamp pumped rod amplifiers. At the input of the pre-amplifier, a temporal beam shaping setup has been implemented to allow working with either front-end or with both of them simultaneously to achieve complex pulse shapes. In the next step in the beam combiner, the transversal Gaussian beam is shaped into a top-hat beam which is much more adapted to the extraction of energy in power amplifiers. Because super-Gaussian beams are not self-similar, the beam is image-relayed from this point on, throughout the rest of the the laser chain. Within and between every amplification stage the beam is expanded with telescopes to keep the fluence always below the damage threshold of the optics. Additionally, most of the beam transport after the first amplification is done in vacuum to prevent non-linear effects occurring in air at high intensities. The pre-amplifier output energy depends on the aperture used, i.e. the chosen beam diameter, but at maximum it is

able to amplify the front-end pulses to 10 J. The main-amplifier can raise the energy then up to 250 J at maximum before it is re-compressed to short pulse duration (500 fs) again and focused on a target. The short-pulse compressor consists of two dielectric gratings that compress the pulse in time via negative dispersion. Following next in line to the compressor is the final focusing optic, an off-axis copper parabola, which focuses the high-energy laser beam to a spot size of several  $\mu\text{m}$ . Along with the pulse duration of 500 fs and the maximum energy of 250 J (corresponding to 0.5 PW) with the off-axis parabola of small F number, intensities in excess of  $10^{21} \text{ W cm}^{-2}$  can be reached.

The above values represent the optimal parameters of PHELIX while the real experiment parameters are described in chapter 5.

## 3.2 Sources of aberrations in a laser system

Aberrations are deviations in the wave-front from a perfectly flat or spherical wave. The aberrations induced in the main-amplifier by the flashlamp discharge limit the repetition rate of the PHELIX laser to one shot every 90 minutes. Measurements of the aberrations were part of my preceding diploma thesis [72] and have been pursued during this thesis. Measurements of the thermal and on-shot aberrations are presented in the next two subsections. Studying the aberrations is very important because of their influence on the desired hollow beam, as explained in section 2.3.1. Strong aberration would make a propagation of this special beam shape impossible. Therefore, it is necessary to know the origin of the aberrations and how they can be controlled. Three notably sources of aberrations in a laser system like PHELIX can occur and are schematically displayed in figure 3.2:

**Static aberrations:** These aberrations are induced via form errors of the optics or by intentionally misaligned optics. Tilted optics are necessary for reflecting ghost focuses (unwanted focuses along the beam line due to internal reflections in optics) out of the beam axis or suppress parasitic lasing and have a strong contribution to astigmatic aberration. Form errors lead to mostly spherical aberration. As the optics diameters are growing, it is challenging to control the form error. The peak-to-valley



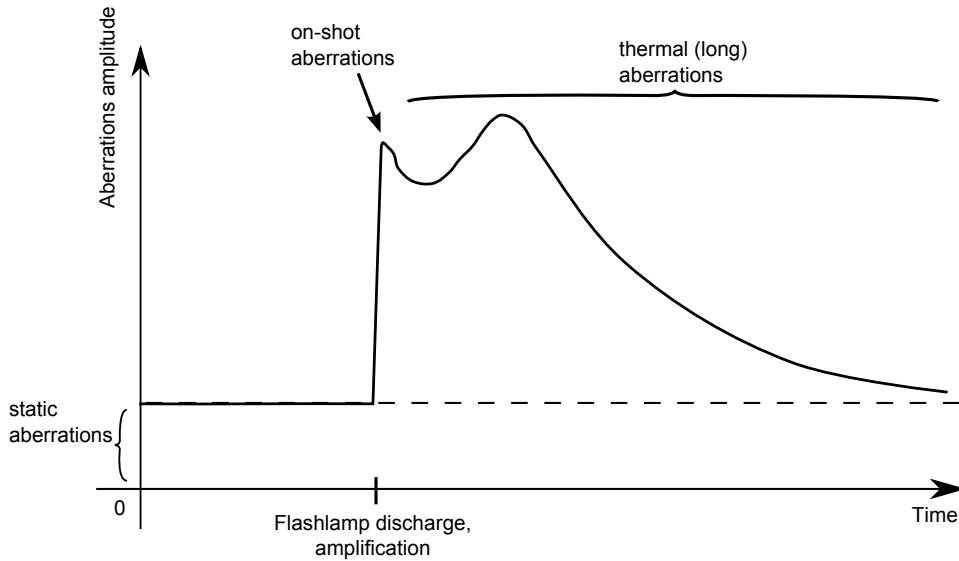


Figure 3.2: Schematic time line representation of aberrations at the PHELIX laser system. Before a shot only static aberrations contribute to the wave-front error. At the discharge point the on-shot aberrations dominate and add to the static one. Thereafter, the cooling begins of the amplifier and it is the regime of the thermal aberrations [72].

(ptv) wave-front error should not exceed  $0.25 \lambda$ . Static aberrations at PHELIX are corrected at low orders by optimized beam line design.

**Shot aberrations:** The discharge of the flashlamps generates a strong heat input in the Nd:glass amplifiers due to the quantum defect and efficiency of neodymium ions in glass. It is instantaneous. This heat input then alters the amplification medium e.g. the length due to linear thermal expansion or the refraction index as well as birefringent properties. The energy deposition is not uniform (in a amplification rod the most absorption is at the edge) and thus this non uniformity of heat deposition leads to a non-uniform temperature map. The laser beam that passes through these excited optical elements will suffer from these on-shot aberrations. The time which passes between the optical pumping and the laser amplification has an impact on the strength of these aberrations. Documenting the on-shot aberrations was an important element of this work.

**Thermal (long time-scale) aberrations:** After a high-energy shot of the laser system PHELIX, the slow flow of the heat, induced by the discharge

of the flashlamps, out of the system is mostly responsible for the waiting time of 90 minutes between the shots. Ideally, the next shot of PHELIX happens after the amplifiers have fully cooled down to their initial temperature to reduce this part of aberrations. With adaptive optics it has been shown that it is possible to increase the repetition rate. Due to the fact that aberrations can be compensated with a closed-loop system to deliver a wave-front almost similar to a reference taken beforehand with a cold system.

### 3.2.1 Pre-amplifier aberrations

The pre-amplifier consists of three Nd:glass rods. The flashlamps are concentrically arranged around each amplifier rod and surrounded by water for cooling. Due to this geometry only cylindrical symmetric aberrations are expected and the  $Z_4$  defocus aberration is the strongest measured aberration, during shot and cool-down (figure 3.3). The other aberrations are insignificant and their magnitude is usually at the detection limit of the Shack-Hartmann sensor. It can be understood from figure 3.4 where the non-homogeneous change in temperature leads to a localized change in the refraction index and therefore to the observed aberrations.

### 3.2.2 Main-amplifier aberrations

In contrast to the pre-amplifier the main-amplifier consists of Nd:glass disks setup at Brewster's angle and that are pumped from two sides. Here, there is no cylindrical geometry and therefore a more complex type of aberration is measured. The cool-down and on-shot aberrations of the main-amplifier are shown in figure 3.5. Due to the fact that the main-amplifier is fired together with the pre-amplifier, a large defocus term  $Z_4$  in the on-shot aberration occurs. The second high aberration is astigmatism  $Z_5$  which can not be explained with the pre-amplifier and therefore is introduced by the main-amplifier. In the main-amplifier, the laser disks stand upright and the flashlamps are installed on either side. Now that the heat input is not homogeneous from all sides a kind of a cylindrical lens is formed which accounts for the astigmatism.

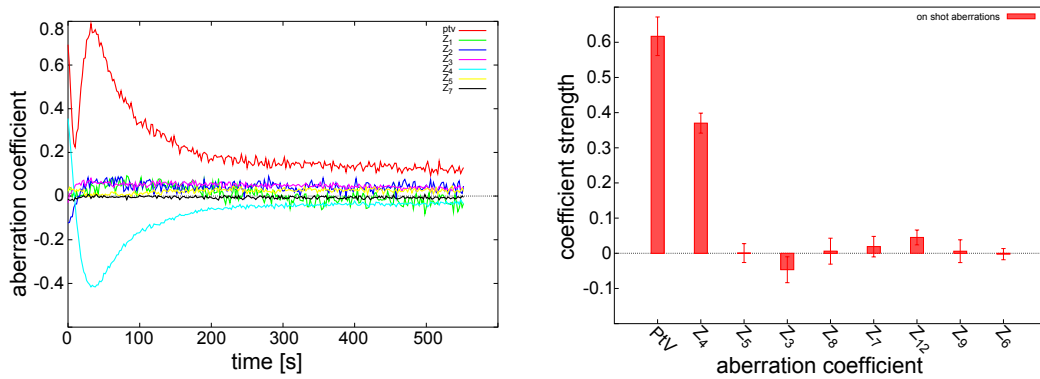


Figure 3.3: Pre-amplifier cool-down aberration measurement over time after the shot (left) and on-shot aberration measurement (right). The strongest aberration during shot and cool-down is  $Z_4$  defocus.

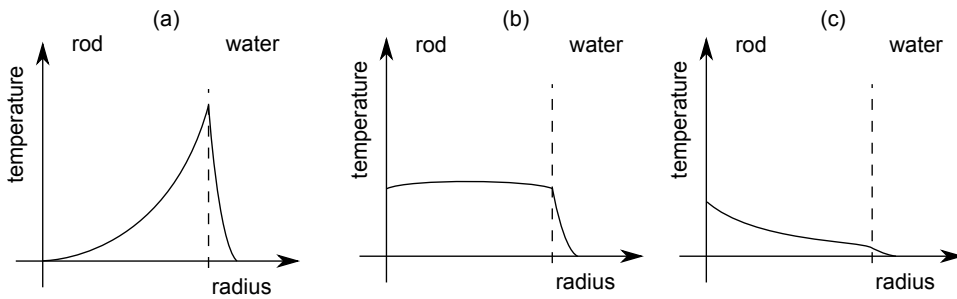


Figure 3.4: Schematic sketch of radial temperature distribution in the pre-amplifier heads. (a) temperature during discharge of the flashlamps. (b) at the zero crossing of defocus. (c) some minutes after a shot.

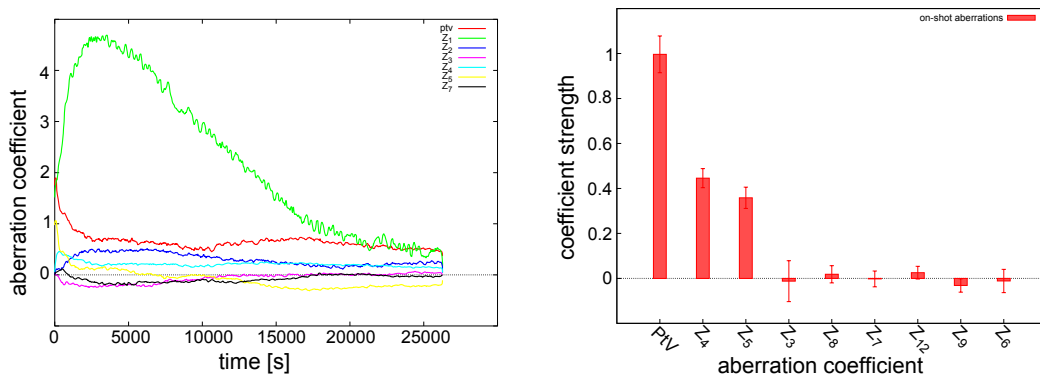


Figure 3.5: Main-amplifier cool-down aberration measurement over time after the shot (left) and on-shot aberration measurement (right). Notably is the  $Z_4$  defocus term that is introduced by the pre-amplifier. The  $Z_5$  term corresponds to  $0^\circ$  astigmatism and is introduced in the main-amplifier. In the cool-down measurement the tilt terms ( $Z_1, Z_2$ , pointing in  $x$  and  $y$  direction) can be neglected since it is easy to correct with a pointing mirror.

### 3.3 Adaptive optics at PHELIX

Adaptive optics generally allow better control of the laser wave-front, or in other words, the spatial phase of the beam. It is a subject area that deals with improving the wave-front via (semi-)automatic corrections. Initially, this kind of technique was deployed at large earth-bound telescopes for correcting wave-front deformations due to turbulent air flow (termed “seeing”) [78]. Several correction elements along with wave-front sensors have been installed throughout the PHELIX system for controlling the spatial phase of the beam. There is a full closed-loop capable adaptive optics system with a bi-morph deformable mirror and two more systems that require a wave-front measurement as feedback (a motorized lens and the bending mechanism installed at the main folding mirror MM1, see figure 3.1).

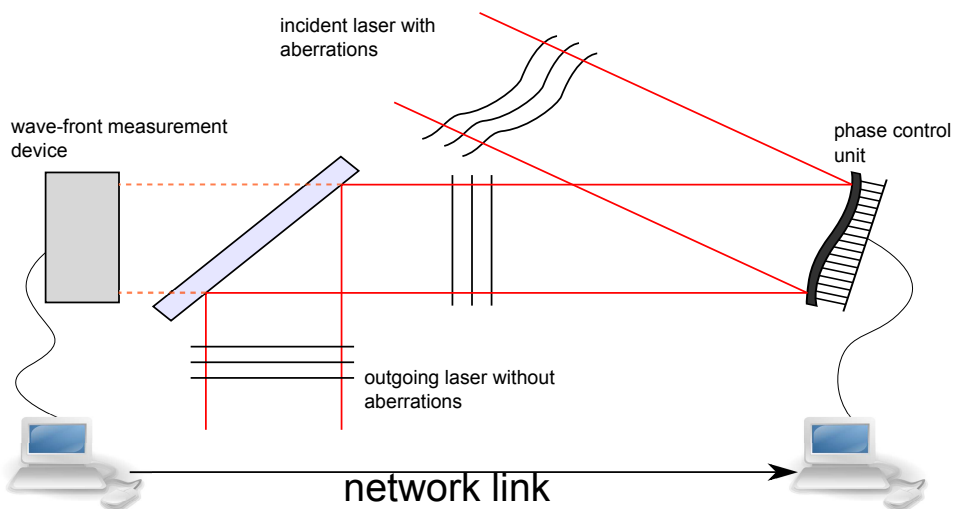


Figure 3.6: Schematic setup of an adaptive optics system. The beam with an aberrated wave-front arrives on the correcting element and is reflected without aberrations. A wave-front sensor measures the phase and calculates needed corrections for the phase control unit.

The elements necessary for controlling the wave-front (see figure 3.6) are: a wave-front sensor for measuring the phase of the laser beam (at PHELIX these are Shack-Hartmann sensors described in the next section), a correcting element that applies the required changes to the spatial phase, and a computer with corresponding software is needed for closed-loop operations.

The three mentioned correcting elements are in detail:

**Bi-morph deformable mirror:** This kind of adaptive mirror features a continuous surface bent by a force applied on the back side. This solution has the advantage of preventing diffraction occurring at the boundaries of discrete mirror elements featured by other adaptive mirror technologies [79]. It consists of a thin glass substrate coated on one side with a high-reflection coating and one or more (structured) piezoelectric disks glued to the other side. An adjustable voltage of several hundred volts at each piezoelectric element allows for a local deformation of the surface. In first order the deformation reacts linearly to the applied voltage and without any electric hysteresis. It can be utilized to correct all types of aberrations. Since the dynamic range of the actuators is limited, it is important to unload this device and correct simple aberrations with the two other devices mentioned next.

**Motorized lens:** A telescope lens of the pre-amplifier was motorized to correct for on-shot defocus aberration. The strength of the correction is proportional to the lens position.

**MM1 bending mechanism:** In addition to the two above-mentioned mechanism the third device has been introduced to support the work of this thesis and address specifically the astigmatism aberrations of the main-amplifier by employing a new bending mechanism at the main folding mirror MM1 shown in figure 3.7. It consists of two linear motor stages attached at the top and bottom of the mirror to apply a force on its surfaces near the upper and lower edges with respect to points at its left and right edges. With this tool it was demonstrated that it is possible to reduce the static and on-shot  $0^\circ$  astigmatism ( $Z_5$ ) aberrations of the main-amplifier.

### 3.3.1 Shack-Hartmann wave-front sensor - SHS

The Shack-Hartmann sensor (SHS) principle is a stable way to measure the whole wave-front at once. An incident wave-front is mapped by an array of micro lenses which focus the light on a CCD chip behind the lens array. An even wave-front under normal incidence will produce an array of focuses in the center of each sub-aperture. A wave-front with deviation will cause the focuses to be displaced from their respective aperture centers by a shift of  $dx$ . The shift is proportional to the gradient of the wave-front (figure 3.8). With these shifts, the wave-front can be reconstructed and the control signal can be calculated for the adaptive optics.

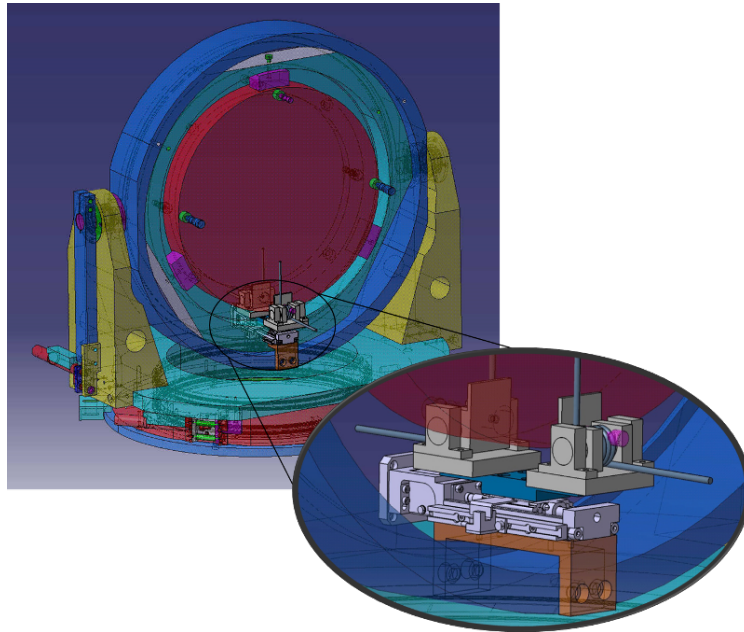


Figure 3.7: The new bending mechanism installed at the main folding mirror (MM1).

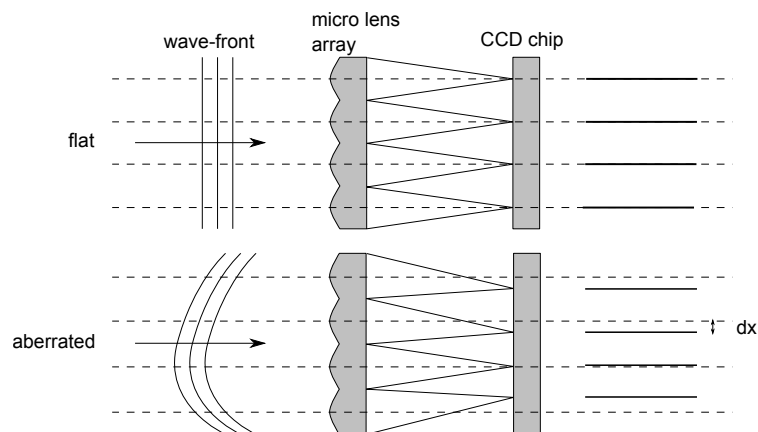


Figure 3.8: Measurement scheme of a Shack-Hartmann sensor. Top: A flat wave-front impacts onto the micro-lens array and is focused without any deviation. Bottom: The distorted wave-front is focused away from the center of each sub-aperture. The focus position shift  $dx$  is proportional to the gradient of the incoming wave-front.





# CHAPTER 4

---

## The hollow laser beam

---

All experiments conducted for this work were carried out at the PHELIX Petawatt target area using the CPA short-pulse beam (section 3.1) and were approved by the *PHELIX and Plasmaphysics Program Advisory Committee (PPAC)*. The experiments focus on the optical control of the laser focal spot to influence the proton beam parameters. This chapter is dedicated to the work that was done on the laser system to be able to use the proposed hollow beam in a TNSA experiment. First the phase mask, necessary for creating a hollow beam is described. With this phase mask, it was possible to study the propagation of the hollow beam throughout the PHELIX laser system. It was observed that the hollow beam is sensitive to aberrations induced by optical elements (section 2.3.1). Therefore a beam time was dedicated to identify and compensate for these effects. Improving the beam quality, i.e. wave-front, was necessary to propagate the hollow beam through the whole laser system up to the target chamber. At the end, these steady efforts culminated in the best beam quality at the PHELIX laser achieved so far.

Measuring the real intensity distribution on the target during the laser-matter interaction is a difficult task. Dedicated to this, a new type of diagnostic was built and implemented at the experiments. The on-shot focus diagnostic utilizes relativistic effects occurring inside the plasma. It images frequency up-shifted infrared laser light created at the critical plasma density surface, to give a direct access to the intensity distribution. After its initial implementation, this new type of diagnostic was spatially calibrated. The imaging quality was

verified with an extreme case of focal intensity distribution. A strongly astigmatic (line) focus was created and recorded with the on-shot focus diagnostic. A good agreement between the focal spot before and during a full-energy shot could be observed.

This chapter covers the creation and propagation of the hollow laser beam up to the impact on the front side of a TNSA target during a full system laser shot. The generated hot electron distribution and resulting proton spectra will be analyzed in the following chapter 5.

## 4.1 Phase mask for hollow beam creation

In order to shape the accelerating electron sheath of the TNSA mechanism, one can either use different target geometries [80] or influence it with a special focal spot geometry, as shown in section 2.3. In this work the phase shaping of the laser pulse is done with a phase mask (figure 4.1) designed to give an annular focal spot (refer to 2.1.2).

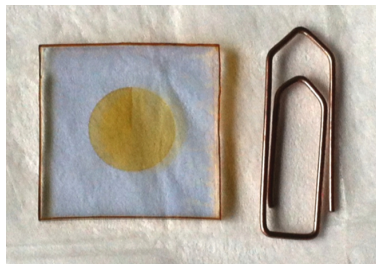


Figure 4.1: Example of a phase mask element that was used for the hollow beam.

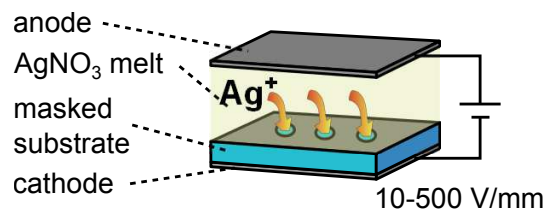


Figure 4.2: Schematic representation of the ion exchange method. Silver ions are doped into the glass material with a supportive potential and thus locally change the refraction index.

The spiral phase element (SPE) converts the Gaussian  $TEM_{00}$  mode of PHELIX into a Laguerre-Gaussian like mode  $L_{0n}$  with  $n$  being the height of the helical phase [31, 81]. For this thesis SPEs were used with a phase  $\exp^{in\Phi}$  and  $n$  from 1 to 5. The SPEs were manufactured by the company SMOS<sup>1</sup> after an iterative development process. They are written into a bulk glass substrate via the ion exchange method (figure 4.2), where the glass substrate is masked

<sup>1</sup>SMOS, <http://www.smos-microoptics.de/>

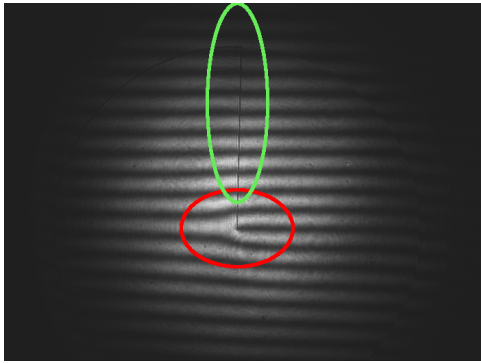


Figure 4.3: An interferogram taken with the Mach-Zehnder interferometer of a  $2\pi$  phase mask.

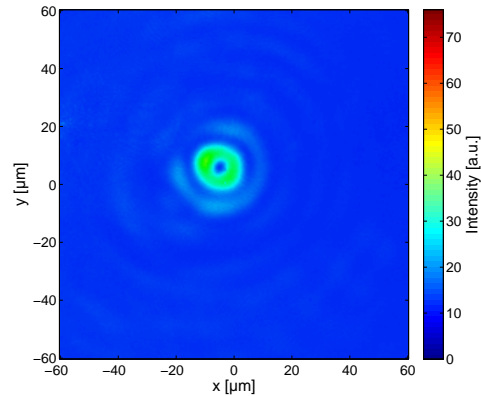


Figure 4.4: The focal profile of the phase mask measured in transmission.

with a metal that regulates the ion exchange process. Since the glass substrate is submerged in a silver nitrate bath along with an applied potential, silver ions move into the glass where no covering mask is present. By varying the time and applied potential, the change of refractive index can be controlled. After the manufacturing process the phase elements were coated with an anti-reflection coating to reduce interference effects inherent to a plan-parallel glass.

We built a dedicated Mach-Zehnder interferometer to verify the quality of the SPEs in terms of spatial phase (figure 4.3). The central discontinuity can be seen (red circle), where a fringe splits up into two, i.e. a phase jump of  $(2n - 1)\pi$ . Above that point in the image (green circle), the line where the fringes are interrupted, is after a full round trip of the phase, where the phase jump is  $2n\pi$ . As the line is thin and the fringes left and right of it fit each other, it implies that the phase mask operate as expected and is tuned for the PHELIX laser wavelength. The Mach-Zehnder interferometer was built to measure the transmission of the phase mask, too. In figure 4.4 the focus profile of such a transmission measurement is illustrated. As the interferogram indicates, the focus intensity distribution is very good in terms of ring shape. Even the diffraction rings around the central focal spot could be observed.

## 4.2 Hollow laser beam propagation

A beam time was dedicated to the study of the propagation of the hollow beam and to evaluate the influence of spatial phase errors throughout the PHELIX laser system. But before hand, a study was made about the best strategy to implement the hollow beam at PHELIX. The SPE is inserted in the beginning of the amplification chain of the PHELIX laser system, in the pre-amplifier (figure 4.5). The reasons for this decision were for cost reduction and for easy handling, because there, the phase mask has to be only several millimeters in diameter. Otherwise the phase can be introduced anywhere in the system because it is a propagation invariant beam mode.

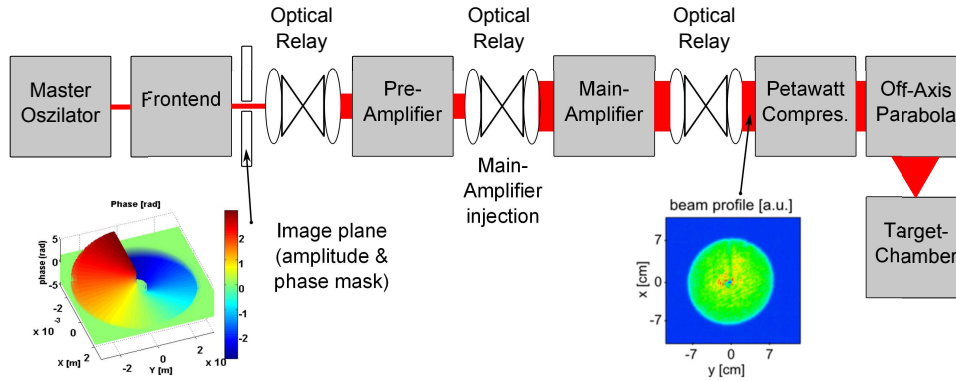


Figure 4.5: Schematic sketch of the different PHELIX stages along with phase mask position.

The investigation started by propagating the beam through the PHELIX laser system. Measurements of the beam profile and wave-front along with the focal profile were carried out at several stages of the laser chain, namely at the pre-amplifier, main-amplifier and the injection box, as well as behind the pulse compressor. Already during the tests, we observed that aberrations made it difficult to achieve an undisturbed propagation of the hollow beam through the laser system. We worked at reducing the occurring wave-front aberrations by utilizing the different adaptive optics systems that resulted in an improved beam transport quality that allowed the propagation of the hollow beam up to the target chamber.

Shown in figure 4.6 are two pictures of a ring focus. The left is recorded

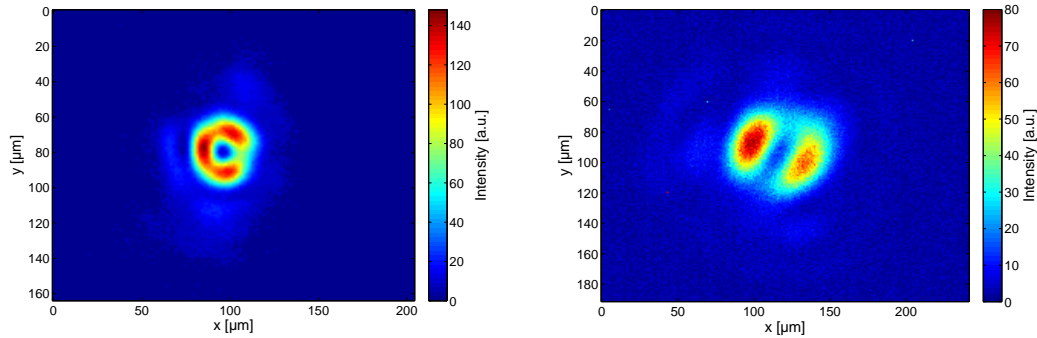


Figure 4.6: Comparison of beam focus measured in the target chamber before (left) and during a high-energy shot measured at the compressor sensor (right). The remaining on-shot aberrations still have a significant influence on the shape of the ring focus during a shot.

with the front-end only via the focus diagnostic in the target chamber before a shot, while the right one is imaged on-shot at the compressor diagnostic during a high-energy shot. It can be seen that the on-shot aberrations have a significant influence on the shape of the ring focus during a shot (refer to section 2.3.1 and 3.2).

Therefore in a second beam time, when ion acceleration was first demonstrated experimentally with the hollow beam, even further improvements were applied to the laser system in terms of spatial phase compensation. Within a system realignment, the stress relief of the optics was improved to reduce the static aberrations in the laser chain. The deformable mirror was adjusted for pre-compensating the occurring on-shot aberrations of the pre-amplifier. The static astigmatism aberration of the main amplifier was reduced with a new bending mechanism installed at the mid-chain folding mirror MM1. Additionally, this mirror was used to counteract the on-shot astigmatism aberrations of the main amplifier. In figure 4.7 examples are illustrated of focus images recorded before a shot and during a shot at the compressor sensor. It illustrates how the pre-compensation of the on-shot aberrations were applied. In the target chamber the focal spot is optimized (a). During a shot an on-shot spot in the compressor diagnostics is recorded (b) and the on-shot aberrations are measured. Then the inverse of these measured on-shot aberrations are applied to MM1 and lead to a distorted focus profile in the target chamber (c). But a better focus profile on-shot (d) is obtained in the compressor diagnostics. The

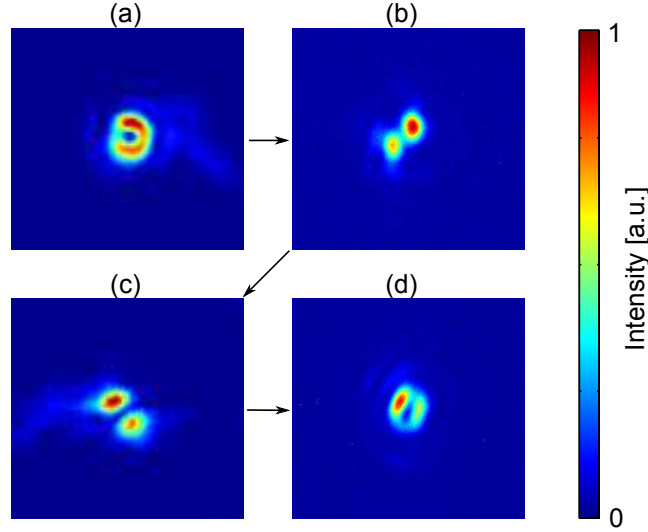


Figure 4.7: Comparison of focal profiles before and on-shot. With the front-end in the target chamber optimized focus (a) results in an on-shot spot in the compressor diagnostics (b) because of the measured on-shot aberrations. Applying the inverse of these measured on-shot aberrations with MM1 leads to a distorted focus profile in the target chamber (c) but to a better focus profile on-shot (d). This is the principle of pre-compensation of the on-shot aberrations.

effect of the remaining not pre-compensated, higher order on-shot aberrations still have an influence on the shape of the focal spot.

These efforts of optimizing the wave-front were still continued in a third beam time, as the adaptive optics systems were improved further to correct also for higher, but less strong, orders of the on-shot aberrations. In all conducted experiments the laser beam quality was subject to steady change due to the use of the adaptive optics. Before every shot the laser system alignment was optimized to get the best wave-front and therefore a beam shape closest to the expected hollow beam shape out of the system, i.e. to pre-compensate the occurring on-shot aberrations as good as possible. The steady improvements that were carried out during this thesis culminate in the best beam quality measured at the PHELIX laser system achieved so far. Beside the improved far field beam quality recorded by the sensors, this became apparent from the boost in maximum proton energy deduced from the RCF stacks. These results are discussed in section 5.5.

In figure 4.8 four different shot focuses are illustrated, measured at the

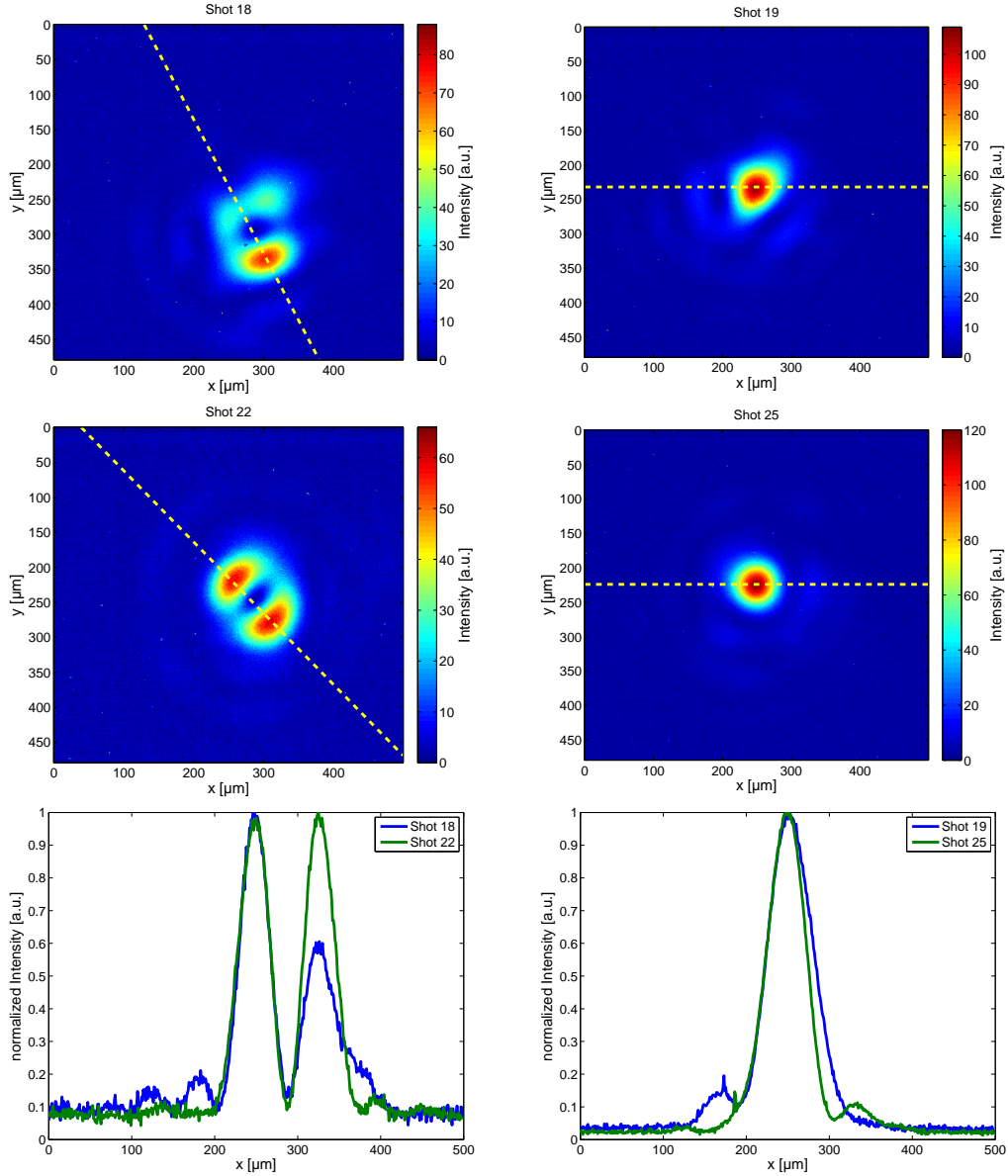


Figure 4.8: Comparison of the on-shot focal spots measured at the main-amplifier output sensor. In the top row a ring and a Gaussian focal spot are displayed (18 and 19). At an optimum reached aberration pre-compensation the shot images are displayed in the middle row (22 and 25) supported by the plotted line averages in the bottom row.

main-amplifier output sensor. In the top row a ring and a Gaussian focal spot are displayed from the beginning (shots 18 and 19). The influence of the on-shot aberrations can be clearly observed. The ring focal spot does not have a symmetric intensity distribution nor does the Gaussian focal spot. In contrast to that, two shot images with improved pre-compensating techniques are displayed in the middle row (labeled as shot 22 and 25). An improvement in the shape of the ring and Gaussian focal spot can be observed. Measurements suggest that the Strehl ratio was increased by at least  $0.10 \pm 0.05$ . Still, the ring focus is not fully closed (this is due to remaining astigmatism aberration), but it has a more symmetric shape and is closer to the desired hollow focal spot. The same holds true for the Gaussian focal spot. This is also supported by the plotted line averages in the bottom row. The ring and Gaussian focal spots are much smoother with less scattered energy, i.e. more energy is confined in a smaller area. This observation is supported by the recorded images with the on-shot focus diagnostic seen in the next section. Up to this point, the last PHELIX laser on-shot diagnostic, satisfying results on the compensation of aberrations were observed. In the next section the newly developed on-shot focus diagnostic is introduced for the measurement of the laser intensity distribution during the laser-matter interaction on the target.

### 4.3 On-shot focus diagnostic - OSFD

This type of diagnostic has been first proposed and demonstrated by *Dromey et al.* [82] in 2009. Here we developed a similar setup adapted to the PHELIX parameters and optimized imaging quality. This implementation gives satisfying measurements of the real laser intensity on the target during the laser-matter interaction. One idea is to image the reflected light from the oblique laser-matter interaction onto a camera and filter for high harmonics ( $3\omega_L$  in our case, for the principle setup see figure 4.9). We have chosen  $3\omega_L$  to obtain a signal which is clearly distinguishable from the background radiation of the plasma and have optics at hand that support that wavelength. For even shorter wavelength it gets difficult to find suitable optics. The imaging conserves the spatial intensity distribution on target. In addition, the camera used



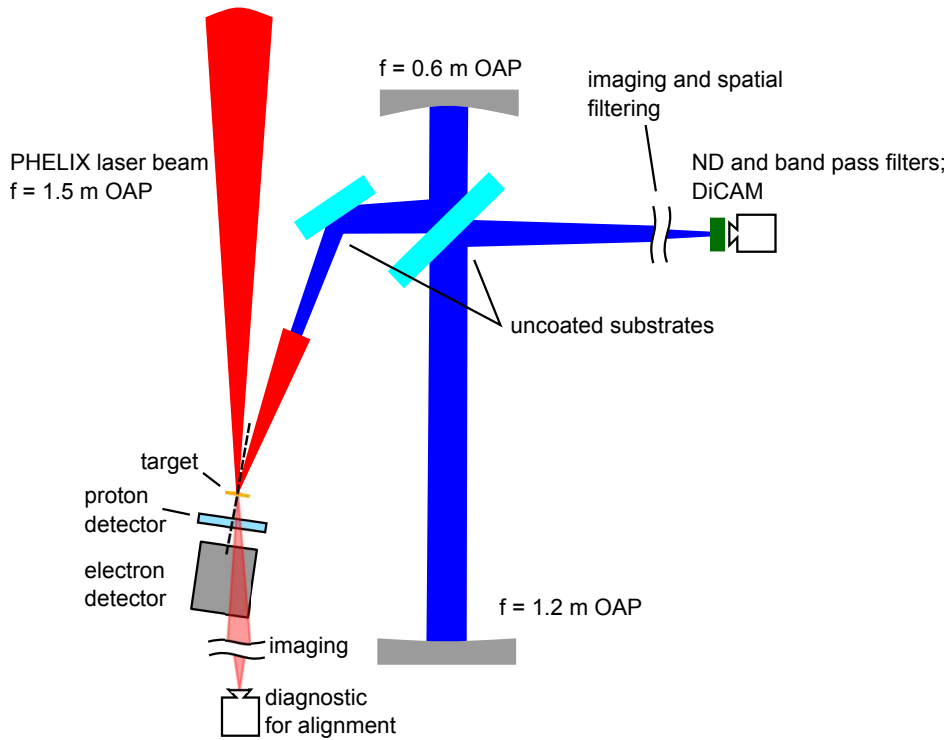


Figure 4.9: The schematic setup of an experiment along with the setup of the OSFD for imaging the laser matter interaction in  $3\omega_L$  with good resolution and low aberrations.

for this was a *dicam pro* (*PCO*<sup>2</sup>) to have the possibility to gate the shutter and therefore reduce the background noise even further. High harmonic generation for laser intensities in the range of  $10^{18} \text{ W cm}^{-2}$  to  $10^{21} \text{ W cm}^{-2}$  is driven by the relativistic oscillating mirror (ROM) effect at the critical density surface [83, 82, 84, 85, 86].

As the order of generation from this effect is linearly intensity-dependent [87], the conversion efficiency to  $3\omega_L$  is then an indirect measurement of the real laser intensity. The effect of a relativistically oscillating mirror is due to the Doppler shift of the incident light on the surface oscillating with relativistic speed. It compresses the laser light and as it is oscillating with the laser period  $\omega_0$ , the reflected light includes high harmonics of  $\omega_0$ , while the coherence of this effect preserve the laser properties like directed emission. The maximum harmonic order of this effect is strongly dependent on the incoming intensity

<sup>2</sup><http://www.pco.de/de/home/>

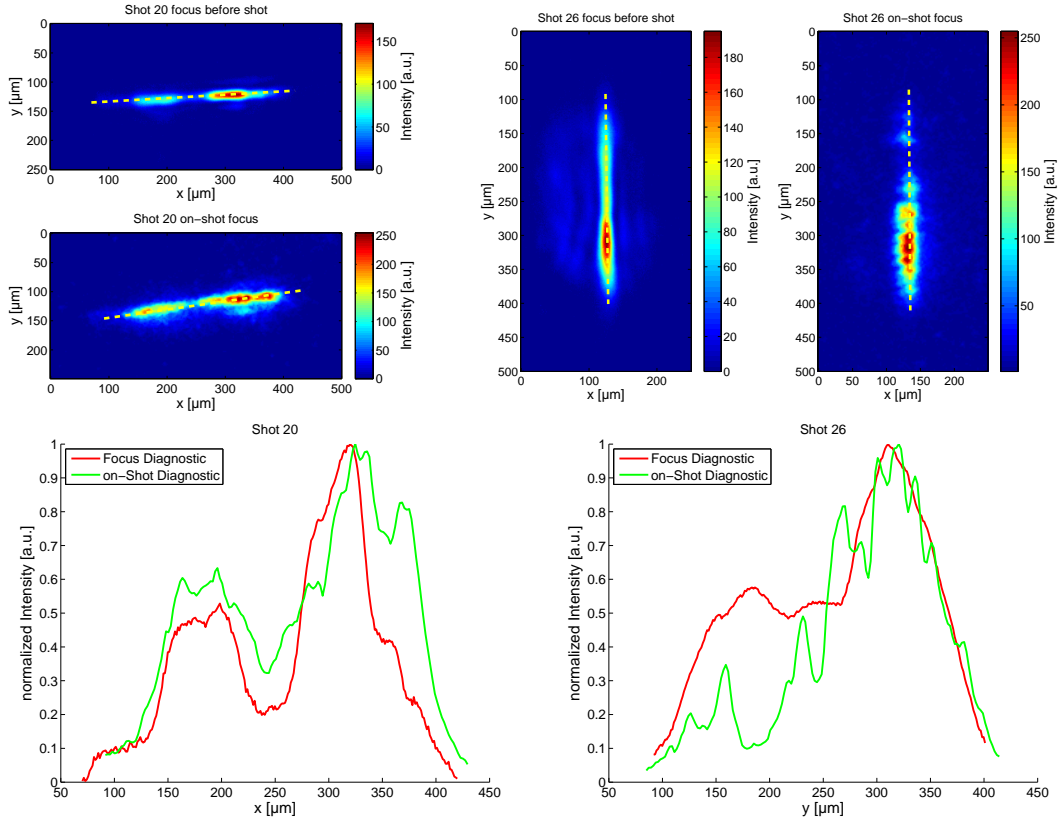


Figure 4.10: Comparison of focal spots measured before a shot with the focus diagnostic and measured with the OSFD at a full-energy shot. Shown on the left are the focal spot shapes before and during the shot 20 and on the right corresponding images for shot 26. Illustrated in the plots at the bottom are the projections along the indicated line for comparison.

[88]. Linear intensity dependency and source size of the  $3\omega_L$  emitting region is in the following experimentally confirmed using an extreme case of laser focal spot: a strongly astigmatic (line) focus. This extreme focal spot shape was applied to verify that the on-shot focus diagnostic gives comparable results to the focus diagnostic that is used before a shot. That means that the spatial intensity distribution measured in both diagnostics is qualitatively the same.

Figure 4.10 shows two intensity distributions measured by the focus diagnostics after alignment and their corresponding on-shot images, recorded with the OSFD during a full-energy shot. A qualitative match between the focal spots, recorded before and during the shot, can be observed in terms of shape and intensity distribution. This is important, since a totally different shape

in the OSFD would imply either, a faulty alignment of the final focusing optics or of the on-shot focus diagnostic itself. Validating the principle of this OSFD was important, because a major part of this thesis is focused on the laser beam propagation and creating a hollow focal spot on the target. Therefore, a strongly astigmatic focus was created in the target plane by an intended misalignment of the last focusing element. In figure 4.10 the area of the FWHM intensity of shot 20 is measured to  $(218.7 \pm 2.7) \mu\text{m} \times (23.0 \pm 2.7) \mu\text{m}$  for the focal spot recorded before and  $(252.90 \pm 4.36) \mu\text{m} \times (45.80 \pm 4.36) \mu\text{m}$  for the measured on-shot focal spot. The shot 26, where the line focus was created perpendicular to shot 20, is measured to  $(21.9 \pm 2.7) \mu\text{m} \times (253.8 \pm 2.7) \mu\text{m}$  for the focal spot recorded before and  $(34.80 \pm 4.36) \mu\text{m} \times (228.90 \pm 4.36) \mu\text{m}$  for the measured on-shot focal spot. This is a good agreement concerning the dimensions of the laser focal spot and fulfills the expectations. The illustrated line averages of figure 4.10 (bottom) support this observation. With this kind of newly implemented diagnostic it was the first time that the laser focus intensity distribution was imaged during the laser-matter interaction at PHELIX. The achieved proton acceleration with these shots will be discussed in the following chapter.

Figure 4.11 displays the four selected focal spots measured with the on-shot focus diagnostic from the target for comparison. The same shot numbers as in figure 4.8 are illustrated. In the top row a ring (left) and a Gaussian (right) focal spot are displayed. The bottom row (22 and 25) displays two shot images after the final wave-front improvement. One observes that the area reflecting the frequency up-shifted light is much smaller. We counted the pixels that are above half the maximum value. With this analysis method, shot 18 (ring focus) resulted in a pixel count of  $(1058 \pm 99)$  pixel while shot 19 (Gaussian focus) gave a pixel count of  $(747 \pm 89)$  pixel. Shot 22 and 25 have a significantly smaller area. Shot 22 (ring focus) resulted in a pixel count of  $(361 \pm 83)$  pixel while shot 25 (Gaussian focus) gave a pixel count of  $(162 \pm 48)$  pixel. The reflected peak intensity is nearly the same for all displayed shots which means that due to the smaller area less energy is reflected in frequency up-shifted  $3\omega_L$  light. The laser energy was comparable for all shots, 70.2 J and 64.6 J laser energy for shots 18 and 19 while shots 22 and 25 had a laser energy of 73.7 J and

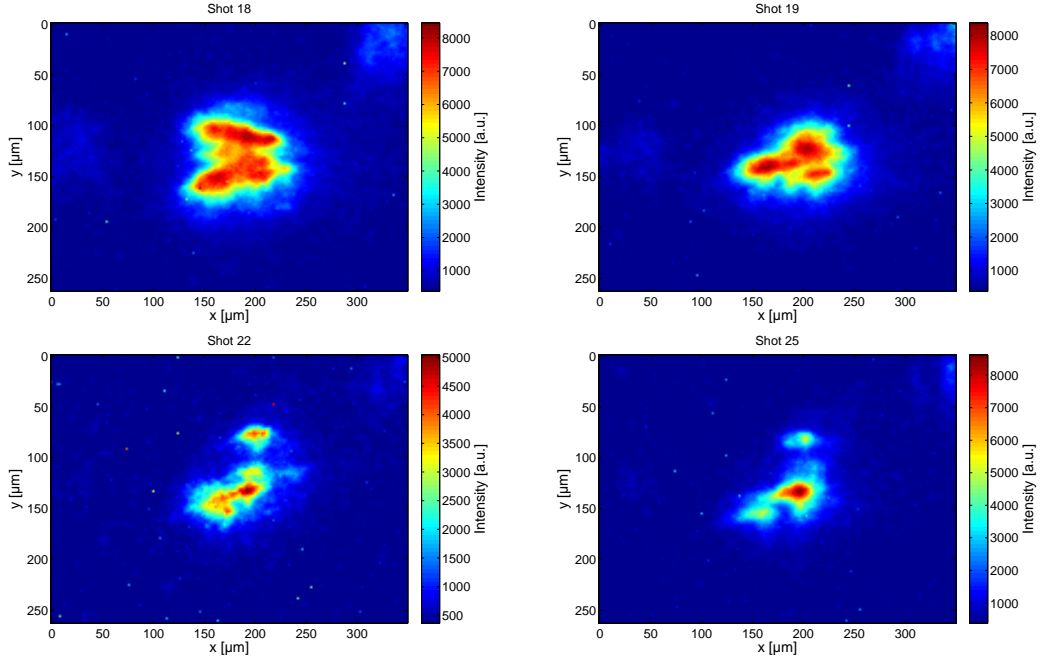


Figure 4.11: Comparison of the on-shot focal spots measured with the OSFD reflected from the target. The same shot numbers as in figure 4.8 are displayed. In the top row a ring (left) and a Gaussian (right) focal spot are displayed. The two shot images that are displayed in the bottom row (22: ring and 25: Gaussian) are recorded after the final wave-front improvements.

67.4 J. A possible explanation is, deduced from figure 4.8, that the improved wave-front of the laser leads to less scattered laser energy. Therefore more energy is concentrated in the central focal spot pattern and is relativistically self-focused to a smaller area [89, 90, 91]. This means more laser energy was transferred to the ion accelerating electrons, i.e. more electrons are accelerated to the rear side of the target, and therefore higher proton energies are reached. This can be seen in the proton data of section 5.5.

# CHAPTER 5

---

## Results of TNSA experiments

---

As chapter 4 was dedicated to the work that was done on the laser system, this chapter concentrates on the results of the laser-driven ion acceleration. Firstly, the laser and target parameters are presented followed by a description of the employed electron spectrometer and a measurement of the hot electrons. As the electrons are accelerated by the laser field and they in turn accelerate the protons, the influence on the hot electron generation with different laser focal spot geometries was studied. Thereafter follows a description of the main proton diagnostic, the radiochromic films. A proper analysis of these films is necessary to gather quantitative data on the ion beam. Therefore, I invested some time in the improvement of the existing analysis routine, which is used for the analysis of the radiochromic films. Then the laser-driven ion acceleration data that were taken throughout the different experiments, will be discussed and analyzed with respect to the influence of the hollow laser beam.

Figure 5.1 illustrates an example for an experiment setup (refer also to figure 4.9 for a schematic setup). The laser beam enters from the left side and hits the target in the center where the laser-matter interaction takes place. A radiochromic film stack is mounted shortly behind the target, for the measurement of the protons. The stack has a hole to give a direct view to the electron spectrometer which is placed behind the radiochromic film stack. The reflected, frequency up-shifted light is gathered and imaged by the on-shot focus diagnostic, described in section 4.3. It is necessary that all diagnostics have a direct view at the target where the interaction takes place.

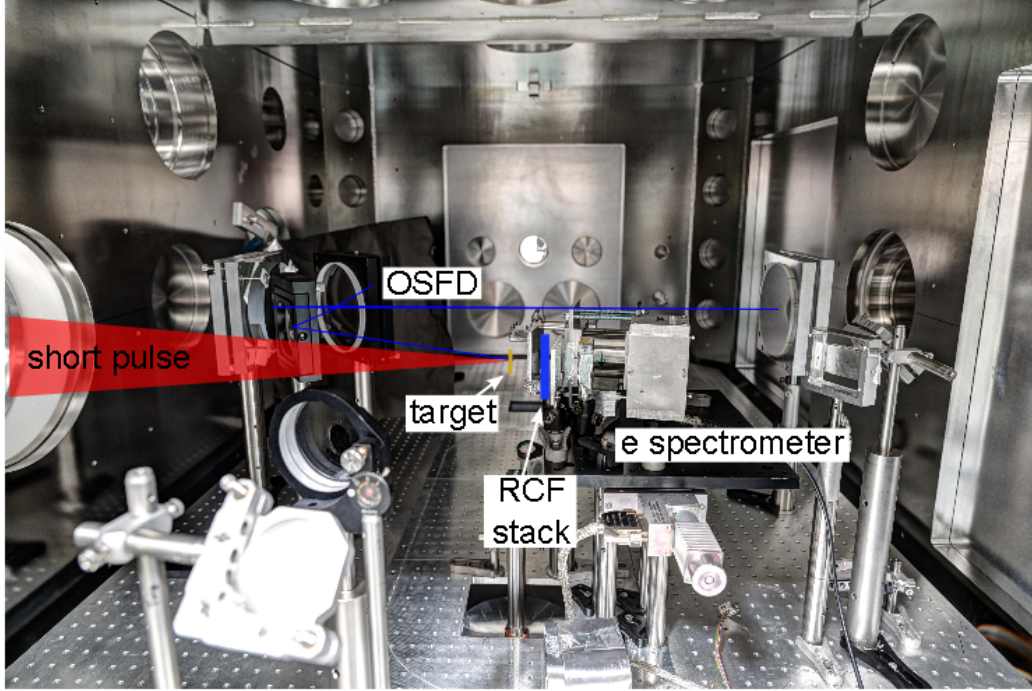


Figure 5.1: Example experiment setup for laser-driven ion acceleration. The beam enters from the left side and hits the target in the center. A radiochromic film stack is mounted shortly behind the target and has a hole to give a direct view for the electron spectrometer. The reflected light is gathered and imaged by the on-shot focus diagnostic.

The experiments were performed with flat gold foils with thicknesses ranging from  $3\ \mu\text{m}$  to  $20\ \mu\text{m}$ . For reproducible measurements the target foil was always aligned to the best focal position. This was achieved by a common set of laser diagnostics for optimizing the focal spot and a laser back-lighted target alignment. The majority of shots were done with the 12 cm round sub-aperture of the PHELIX beam, delivering 50 J to 80 J of laser energy on the target. Beside that some shots were performed with an elliptical laser beam ( $\approx 12\ \text{cm} \times 24\ \text{cm}$ ) delivering up to 120 J laser energy. The laser pulse duration was always constant at  $\tau_L = 650\ \text{fs}$ . All in all there were 56 successful high-energy experiment shots with and without the hollow beam feature over three experiment campaigns. Some shots were dedicated to study the effect of different contrast levels of the PHELIX laser system (the chosen contrast levels were normal  $\approx 10^{-6}$ , best  $\approx 10^{-11}$  and a level in-between of  $\approx 5 \times 10^{-8}$ ) and to the investigation on laser-driven ion acceleration with a line focus.

## 5.1 Magnetic electron spectrometer

For this work we employed a permanent magnetic dipole spectrometer as a detector allowing the detection of electrons. They are of particular interest because they are coupled to the laser intensity distribution and correlated to the maximum proton energy (see section 2.2). Therefore it was necessary to measure spectrally the hot-electron generation at this stage of the laser-driven ion acceleration to reveal an influence of the hollow laser focus. The development and characterization of the magnetic dipole spectrometer has been performed in another thesis [92]. Due to the low magnetic stiffness of the electrons a rather short ( $\approx 6$  cm length) dipole is used to detect the hot electrons (up to 30 MeV). A schematic of the detector setup is shown in figure 5.2.

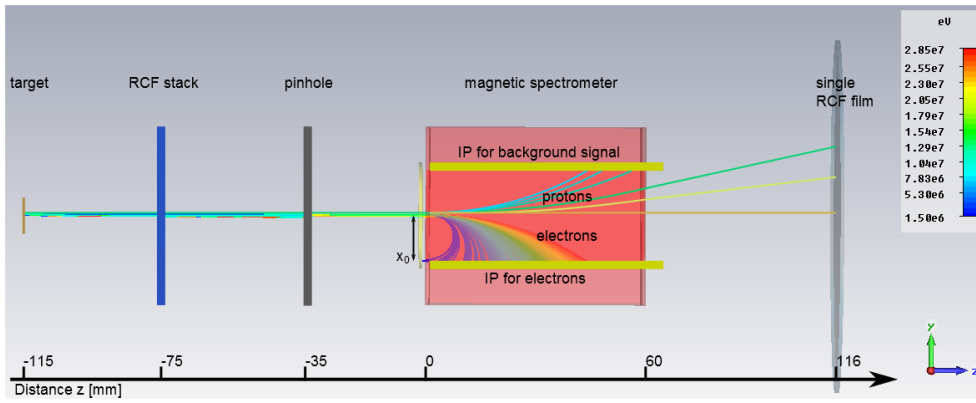


Figure 5.2: Schematic setup of the used magnetic dipole spectrometer. The electrons are bent inside the dipole onto a image plate detector, while the protons, that pass through the hole of the front RCF stack, are deflected and then detected by a single RCF additionally. On the opposite side of the electrons, an additional image plate for background signal is used [92].

The link between deflection  $z$  and energy  $E$  of the electrons is given by the dispersion relation

$$z(E) = \sqrt{\frac{2x_0 \sqrt{\frac{E^2}{c^2} - c^2 m_0^2}}{eB}} - x_0 \quad (5.1)$$

with  $x_0$  being the entrance height,  $c$  is speed of light,  $m_0$  the rest mass of a electron,  $e$  is the elementary charge, and  $B$  being the magnetic field strength. The plot of the dispersion relation is shown in figure 5.3.

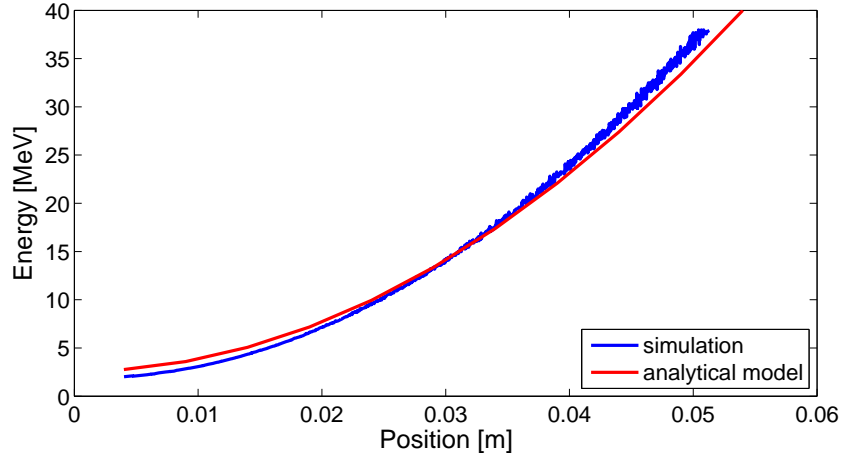


Figure 5.3: Electron dispersion relation of the magnetic spectrometer.

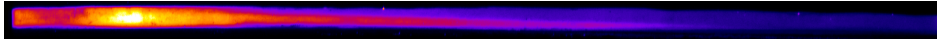


Figure 5.4: Measured electron trace on IP.

The detector for the electrons was a (reusable) image plate (IP) inside the spectrometer. IPs can be used to detect any kind of ionizing radiation [93, 94]. A special care has to be taken for the handling and digitalization of the IP (performed here with a FLA7000 Fuji scanner, pixel size  $50\ \mu\text{m}$ , sensitivity 10 000, latitude 5). First, the signal on the IP decreases over time after irradiation, so care has to be taken about the delay between experiment and scanning. And second, it is important to protect the IP from ambient light which can erase the signal on an IP. Only after the scanning process the IP is erased and thereafter it can be reused. An example of a recorded electron trace is shown in figure 5.4.

Figure 5.5 and table 5.1 illustrate the recorded electron traces and their corresponding temperatures  $k_B T_e$ . No clear influence of the focal spot geometry (ring or Gaussian) is observed. As the ring focal spot diameter is almost double the diameter of a Gaussian focal spot, the intensity drops to a quarter if the energy of the laser beam is constant. Therefore, one would have expected a lower electron temperature measured in the shots where a phase mask is applied. One possible explanation is that in turn more electrons are generated instead of acceleration to higher energies. More electrons that gather at the



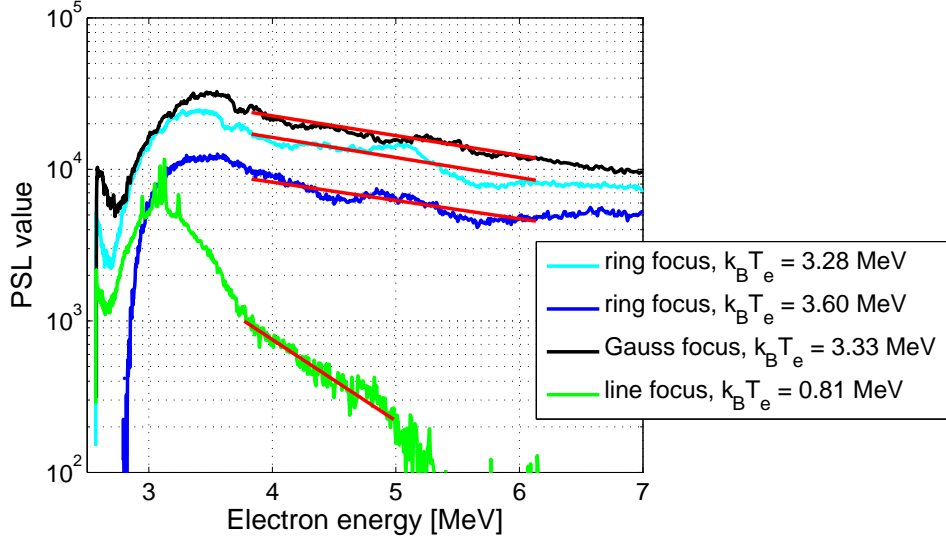


Figure 5.5: The comparison of electron temperature with different focal spot geometries, taken from [92]. The green line corresponds to a strongly astigmatic line focus of the previous section 4.3.

Table 5.1: Comparison of electron temperature  $k_B T_e$ , taken from [92].

Shot	Focus	$E_{protons,max}$ in MeV	$k_B T_e$ in MeV
23	ring	32.7	$3.28 \pm 0.22$
24	ring	30.6	$3.60 \pm 0.09$
25	Gauss	34.6	$3.33 \pm 0.12$
26	line	12.8	$0.81 \pm 0.04$

target rear side can also create a stronger electric field, which in turn can accelerate the protons to higher energies. The absolute electron numbers were not measured within the experiments because no calibration for the IP and electrons was at hand. The electron spectrometer was in operation at  $0^\circ$  to the target normal and covered a solid angle of  $\approx 0.34^\circ$ . The green line corresponds to a strongly astigmatic line focus of the previous section and shows a lower temperature as expected for this strong reduced laser intensity.

In table 5.1 the empirical scaling of equation (2.38) can be observed, too. The maximum measured proton energy lies in the range of ten times the hot electron temperature within a 18% error. Shot 26 does not match with this prediction because of the used line focus in comparison to the other shots.

## 5.2 Radiochromic film - RCF

The main diagnostic used for the laser-accelerated protons in this work were the *Gafchromic*® radiochromic films (*International Specialty Products, Ashland*, hereafter RCF). These are spatially resolving (5  $\mu\text{m}$  to 25  $\mu\text{m}$ ) films that change color (to blue) when exposed to protons, ionizing radiation or even neutrons [95]. The polymerization of molecules inside an active layer is responsible for the coloring. Molecules that were excited by radiation start to polymerize as long molecule chains and change their absorption spectrum. The strength of the coloring is proportional to the dose of the radiation [96]. They are widely used as a diagnostic for laser-accelerated protons [97] because they provide fast and precise measurements of the proton distribution and thereby capture all protons. This is an advantage over other solid-state nuclear track detector types, e.g. which needed to be etched before analyzed like CR-39. RCF types, schematics and compositions used for this work are tabulated in table 5.2 and 5.3. The different layer thicknesses and compositions of the films are responsible for the energy sensitivity. Studies have shown that neither the dose rate nor the radiation energy (for same dose level) have significant influence on the film response. This makes the films suitable for medical applications (low dose rate) but also for highly intense bunches like TNSA accelerated protons [2, 18, 98]. In addition, RCFs are insensitive to temperature (below 60 °C) and visible light.

Table 5.2: Atomic composition the RCF layers consists of [99, 100, 101, 94]. PCDA and LiPCDA are the radiation sensitive coating and are abbreviations for *pentacosa-10,12-diynoic acid* respectively *lithium pentacosa-10,12-diynoic acid*.

Layer	Density [g cm <sup>-3</sup> ]	Atomic composition [%]							
		H	C	O	N	Li	Na	Cl	Br
Polyester	1.35	36.4	45.5	18.2					
PCDA	1.08	56.8	29.1	7.1	6.9				
Adhesive	1.2	57.1	33.3	9.5					
Gelantine	1.2	53.5	22.6	11.1	12.8				
LiPCDA	1.2	58.3	29.6	10.8	0.1	0.8	0.1	0.2	0.1

Table 5.3: Comparison of RCF types.

Film	Dose range [Gy]	Layer composition Layer (table 5.2) thickness [ $\mu\text{m}$ ]
HD-810 (HD)	5 to 2000	Gelantine $\approx 0.7$
		PCDA $\approx 6.5$
		Polyester $\approx 97$
HD-V2 (H2)	2 to 4000	PCDA $\approx 8$
		Polyester $\approx 97$
MD-V2 (M2)	1 to 200	Polyester $\approx 96$
		PCDA $\approx 17.5$
		Adhesive $\approx 20$
		Polyester $\approx 25$
		Adhesive $\approx 20$
		PCDA $\approx 17.5$
EBT3 (E3)	0.01 to 40	Polyester $\approx 96$
		LiPCDA $\approx 27$
		Polyester $\approx 120$

When the films are combined to a stack configuration, the RCFs give a spatially energy-wise resolved proton measurement (figure 5.6 and 5.7). This is based on the energy deposition of the protons in the RCFs according to the well known Bragg curve (radiochromic imaging spectroscopy, RIS [18]). Due to that fact the signal in each RCF can be identified with a corresponding Bragg energy of the RCF in the stack. Bragg energy means that protons starting with this energy suffer the highest energy loss in that RCF and are completely stopped at the end of this film. To avoid a large exhaustion of RCFs to cover the full proton spectrum, metal layers are inserted between the RCFs. By varying the thickness and material (e.g. Copper or Nickel) of these metal layers, the energy deposition of protons can be controlled and the Bragg energy position of the RCFs stretched. The activation of the metal layers can also be used for spatially energy-wise resolved measurement (nuclear activation-based imaging spectroscopy, NAIS [102, 103, 104], but was not used in this work, because no valid calibration was at hand.

After irradiation the RCF has to develop over time for 24 h to 48 h [95],

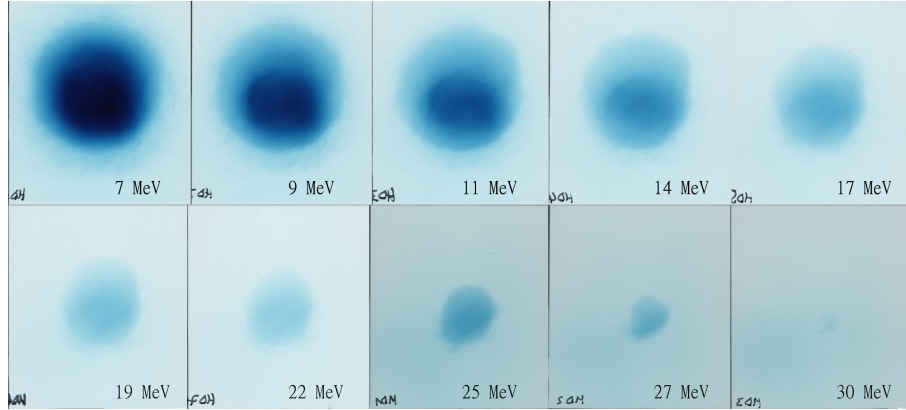


Figure 5.6: Example color scan of a RCF stack irradiated by laser generated protons.



Figure 5.7: Example RCF stack configuration, covering proton energy range from 7 MeV to 38 MeV (left to right).

because only  $\approx 85\%$  of the coloring occur in the first few seconds. During that time the blueish color darkens and thereafter it is stable over time. This is needed to get correct results out of the RCF analyze software (5.2.1). *Hey et al.* [97] calibrated the RCF with a micro densitometer, but the error by using other scanning techniques is negligible [96, 98, 105]. Therefore, after the aging of the films, they are digitized in three color RGB and one infra-red channel by a transmission film scanner (Nikon Super Coolscan 9000ED) and prepared for analysis. The whole data were taken with same settings as the calibration was done, 1000 dpi, 16 bit color depth per channel and all coloring enhancements turned off.

### 5.2.1 RCF analysis software

In order to analyze the RCFs, either per layer or per stack, a dedicated MATLAB software package originally developed by [40, 57], was improved during this work. This was a necessary and also time-consuming step because this analysis package is used to extract most of the results concerning the proton beam. The routine was completely rewritten and optimized for speed, han-

dling, and accuracy. A new calibration along with the Nikon scanner and new color-dependent algorithms made it possible to decrease the uncertainty in the calculated proton energy deposition down to approximately 7%. In the frame of this thesis the newly developed and improved tools for image processing along with code optimization have greatly reduced the processing time for a stack analysis. It works nowadays in very stable manner and can also be employed by users outside the development team. The reconstruction of the energy and spatial distribution was set to work with all occurring beam shapes and not only to some handpicked. Also included is a complete error estimation for the proton spectrum, numbers, and divergence. The software guides the user through several steps needed for correct data analysis. First, the scanned RCF images have to be cut to the same size per stack and are digitally cleaned from dust by analyzing the infra-red channel. After that the three color channels of each individual film are first converted to dose values (after subtracting blank film color values) and then to values representing the deposited energy per layer.

This was a major flaw in previous versions of the software, where the background subtraction was done on the color level and not the deposited energy. As can be seen in an example the calibration curves (figure 5.8) it makes a significant difference to subtract the color values or dose value corresponding to a background signal from a proton signal. For example, assuming a background level of 400 Gy (normalized color values:  $R = 0.55$ ,  $G = 0.33$ ,  $B = 0.14$ ) and a proton signal of about 2 kGy (normalized color values:  $R = 0.72$ ,  $G = 0.62$ ,  $B = 0.33$ ) as illustrated in figure 5.8. A simple subtraction would yield a proton signal strength of 1.6 kGy. Now following the illustration in the figure, one would obtain the color values indicated by the brown dots (normalized color values:  $R = 0.17$ ,  $G = 0.29$ ,  $B = 0.19$ ), if one subtracts the background signal color values from the proton signal. The previous software would calculate a proton signal of 490 Gy which is clearly far away from the real proton signal of 1.6 kGy.

The color calibration of the RCFs used during this work was done at *Helmholtz-Zentrum Dresden-Rossendorf (HZDR)* at the TANDEM accelerator [100]. Ideally, there would be one global calibration function for mapping

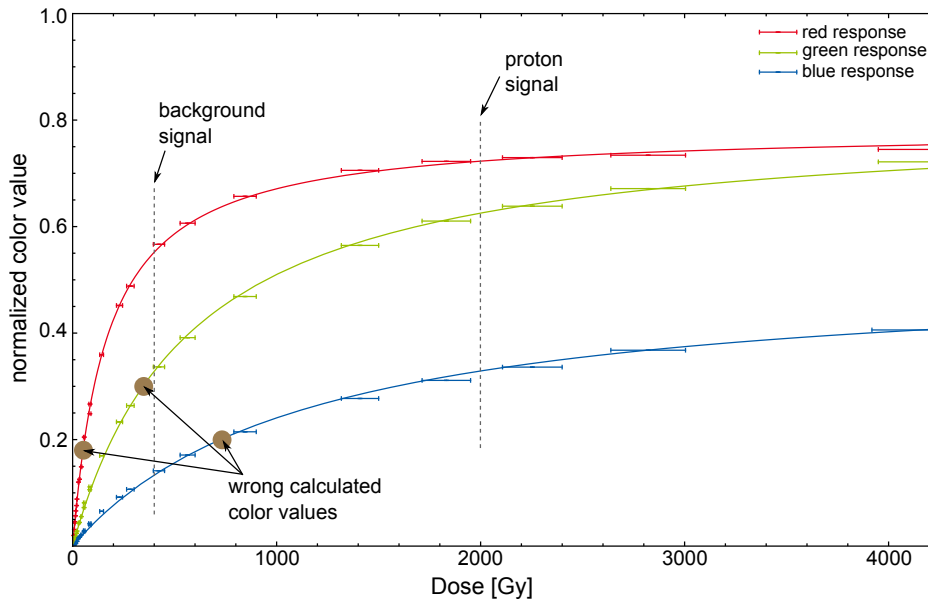


Figure 5.8: RGB Color calibration curves for the HD-V2 film type [100] illustrating the “wrong” background signal subtraction. The two dotted lines indicate the assumed background and proton signal. The brown dots represent the wrong color values obtained with a flawed calculation.

the color (optical density) of the RCFs to deposited energy per film type. But since there are differences in the RCF compositions, scanning method and other sources, that change either the response of the RCF or the digitized color values, each film type has to be calibrated for each respective scanner, handling procedure and per production lot. During the calibration it was seen that different production lot of RCFs show only a difference in response of less than  $< 2\%$ , so this effect is neglected here.

The radiation background correction is done via selecting values that are clearly not part of the proton signal (e.g. due to electrons or x-ray radiation). After conversion and cleaning of the signals automated analyzing routines can be used. This includes measurement of the envelope divergence, reconstruction of the exponential proton spectrum by deconvolution, the determination of a cut-off energy, and the temperature of the proton spectrum. The new routine to calculate the spatial proton number distribution in each RCF layer makes the results more independent from the actual stack configuration. The errors in determining the color values as well as calibration errors are taken into account in this software package.

### 5.2.2 Proton energy spectrum reconstruction

The RCF stack configuration gives the opportunity to deconvolute the proton energy spectrum. Protons that pass through or are stopped in a film transfer energy to its active layer material. Figure 5.9 shows the example stack calculated with the SRIM<sup>1</sup> energy loss tables. The Bragg energy, indicated by red circles, is the initial proton energy a proton has to have to be stopped right at the end of the current active layer. Protons below this energy can not deposit energy in that layer because they are stopped before. With a much higher energy the proton energy deposition contribution in that active layer is lower (shaded area). The deposited energy  $E_{dep,lay}$  is added per layer and corrected by a quenching factor [100]. As previously mentioned, protons loose energy in every layer they go through, so for one layer the calculated deposited energy  $E_{dep,calc}$  can be given as

$$E_{dep,calc} = \int \frac{dN(E')}{dE} \times E_{loss}(E') dE' \quad (5.2)$$

with  $dN/dE$  the proton particle spectrum and  $E_{loss}(E')$  the deposited energy of a given proton energy in the given layer.

This implies, to calculate the proton spectrum  $dN/dE$ , each layer has to be deconvoluted with its response (figure 5.9, solid line). The analysis software achieves this by calculating a convolution of the film response with an assumed exponential energy spectrum for TNSA generated proton beam of the form:

$$\frac{dN}{dE} = \frac{N_0}{E} \exp \left[ -\frac{E}{k_B T_p} \right] \quad (5.3)$$

with  $k_B T_p$  being the proton temperature,  $E$  is the kinetic proton energy and  $N_0$  a constant. With this assumed proton spectrum and the RCF response a deposited energy  $E_{dep,calc}$  can be calculated. Then, the measured  $E_{dep,lay}$  in the experiment is compared to the calculated  $E_{dep,calc}$ . A least mean square fit is used to solve the relevant equations (5.2) and (5.3) numerically for all layers and calculate the parameters  $N_0$  and  $k_B T_p$  (shown in figure 5.10 the deposited energy and the calculated spectrum).

---

<sup>1</sup>The Stopping and Range of Ions in Matter, <http://srim.org/>

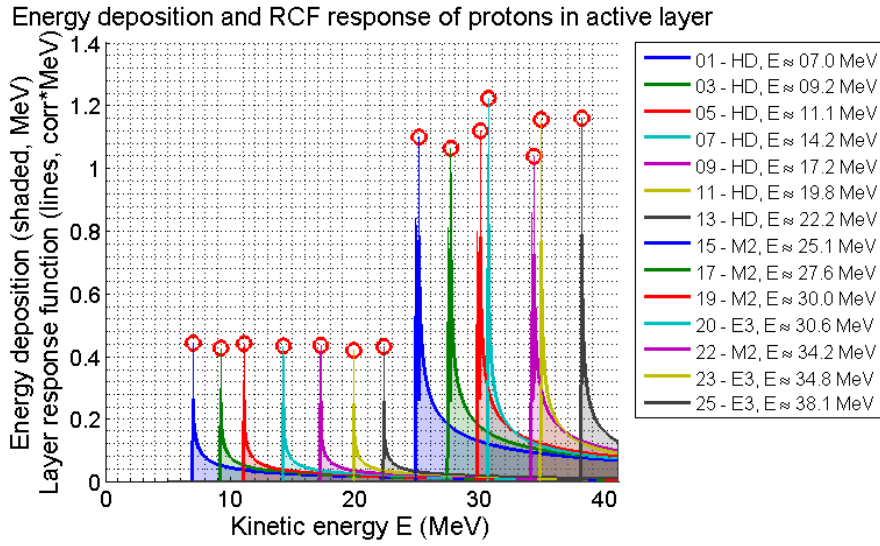


Figure 5.9: Example RCF stack energy deposition and RCF response. Each proton energy deposits energy in the layers before it gets stopped (shaded area). The solid line corresponds to the response of the RCF to protons. The red circles indicate the initial proton energy, with which the proton is stopped at the end of the current active layer. It is the maximum possible energy deposition and correspond to the Bragg energy. The values for the corresponding Bragg energy of a layer is displayed in the legend.

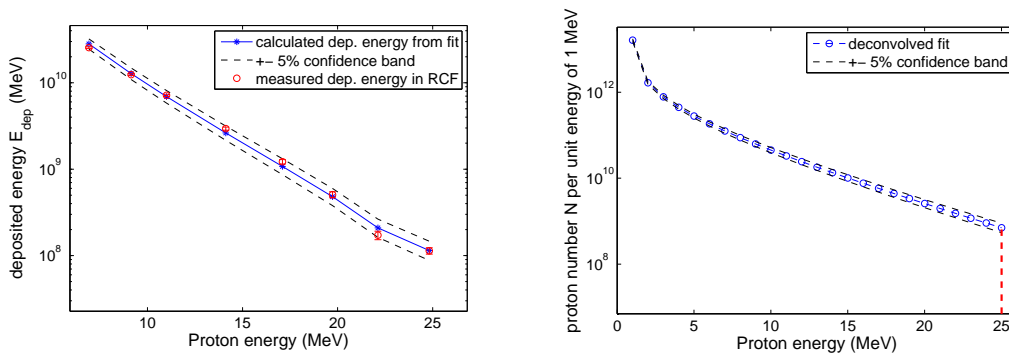


Figure 5.10: Left: Measured and fitted deposited energy. Right: Calculated proton spectrum. For both, parameters are  $N_0 = (3.27 \pm 0.23) \times 10^{12}$  and  $k_B T_p = (4.67 \pm 0.16)$  MeV.



### 5.2.3 Proton envelope divergence

To calculate the divergence of a given RCF stack, one has to know the position of the stack relative to the target (laser-matter interaction) position. Usually a distance of 40 mm has been chosen. For this calculation a point source is assumed, since the distance is large compared to the proton source extend. Even though it is shown that the real source size is energy- and laser-dependent and about  $40\ \mu\text{m}$  to  $400\ \mu\text{m}$  in size [2, 56]. However, because the RCF gives 2D spatial information about the proton beam, one can calculate the envelope divergence angle  $\alpha$  with the imprint size  $x, y$  and distance  $d$ .

$$\alpha = \tan^{-1} \frac{x}{d} \quad (5.4)$$

The diameters in  $x$  and respectively  $y$  are measured and averaged for each RCF layer and approximated with a parabolic curve (see figure 5.11) of the form  $\alpha(E) = a + b \cdot E + c \cdot E^2$ . For TNSA proton beams generated by the PHELIX laser system a empirical determined parabolic fit leads to the best approximation of the measured data.

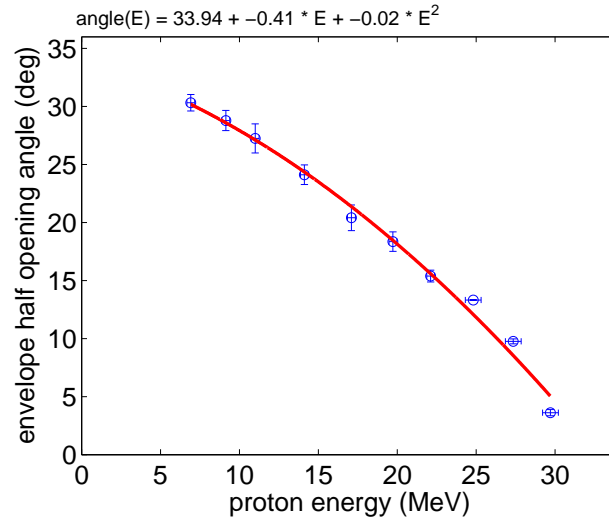


Figure 5.11: Envelope divergence of proton beam fitted with a parabolic polynomial.

### 5.2.4 Spectrally and spatially resolved proton particle profile with graphical deconvolution

With all the advantages of RCFs, i.e. the two-dimensional high-resolution spatial distributions and the energy distribution given due to the stack configuration, it is possible to extract the whole energy-wise spatially resolved proton beam profile. Since it is assumed to be radially symmetric only a cut through the  $x$  plane is displayed in figure 5.12.

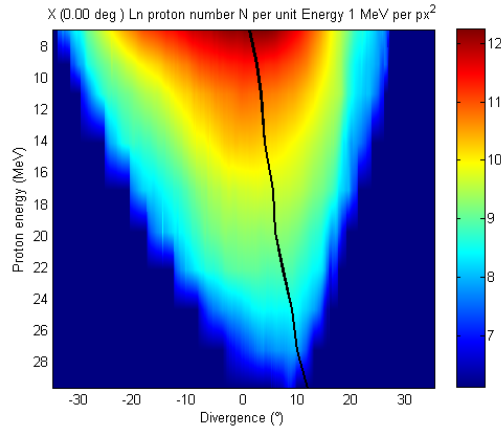


Figure 5.12: Example of a spatially and spectrally graphical deconvoluted proton beam. A cut through the  $x$  plane is illustrated. The black line indicates the maximum proton intensity for each layer. The color corresponds to logarithmic proton number in a 1 MeV energy intervall per square pixel. As it can be seen from the tilted distribution the target was not perfectly perpendicular to the impinging laser beam.

Ideally, this graphical deconvolution of the spectrum would be performed with RCF stacks that have no metal layer in between, but the algorithm written for this thesis can interpolate between two given RCF and relies on the formerly calculated energy spectrum (section 5.2.2). Firstly, the last RCF layer is converted to the absolute number of protons under the assumption that the highest proton energy occurring in the beam corresponds to the Bragg energy  $E_{Bragg,l}$  in that film. Then the number of protons  $N_l$  in that last layer  $l$  is calculated with the measured deposited energy  $E_{dep,l}$  of that film to

$$N_l = \frac{E_{dep,l}}{E_{Bragg,l}}. \quad (5.5)$$

These protons deposit energy in all  $n$  front layers with a spatial profile that is the same as the deposited energy profile  $d_l$ . The deposited energy of the protons  $N_l$  in these layers of the stack can be calculated from the energy loss tables (section 5.2.2) within an  $\Delta E$  energy bin

$$E_{dep,l-n} = N_l E_{loss,l-n} \left( \frac{dN_l}{dE} \right) \Big|_{E_{Bragg,l}}^{E_{Bragg,l} + \Delta E}. \quad (5.6)$$

In addition, protons that were stopped in the inserted metal layer can be estimated by the formerly calculated  $dN/dE$  proton spectrum

$$N_{l,metal} = \int_E^{E+\Delta E} \frac{N_0}{E'} \exp \left[ -\frac{E'}{k_B T_p} \right] dE' \quad (5.7)$$

with  $\Delta E$  meaning the energy bin of the metal layer. With proton numbers  $N_{l,metal}$  their energy deposition  $E_{dep,metal,l-n}$  can be calculated the same way as (5.6), while assuming a spatial profile that is interpolated to be between the last two RCF layers  $d_m$ . As the deposited energy of the protons from the layer  $l$  is less in every layer before, the spatial profiles  $d_l$  and  $d_m$  are weighted by a fraction  $a = E_{loss} (dN_l/dE) \Big|_{E_{Bragg,l}}^{E_{Bragg,l} + \Delta E} / E_{Bragg,l-n}$ , the fraction of the mean energy loss of the protons and the maximal possible energy loss in each layer. The fact that there are more particles in the central part of the proton beam made it necessary to convoluted the spatial profiles  $d_l$  and  $d_m$  in addition with a Gaussian profile  $G$ . A factor  $t$  based on the RCF layer thickness takes care for the different sensitivities of the different RCF types. Then the corrected values for the spatial energy deposition  $E_{dep,new}$  in the front layer can be calculated

$$E_{dep,l-n,new} = E_{dep,l-n,old} - a \cdot t (E_{dep,l-n} + E_{dep,metal,l-n}) \quad (5.8)$$

while the the spatial profiles are calculated the same way

$$d_{l-n,new} = d_{l-n,old} - G (d_l + d_m). \quad (5.9)$$

Until all layers are corrected for the deposited energy of the last layer, the procedure is repeated until the first layer is reached and the profile in figure 5.12 is obtained.

### 5.3 Ion acceleration with strongly astigmatic beams

#### beams

This section presents the measured proton data obtained from experiments with a strongly astigmatic laser focus (see section 4.3), to illustrate the influence of the focal spot shape on the accelerated protons. The first RCF layer and the proton spectra are displayed in figure 5.13 and 5.14.

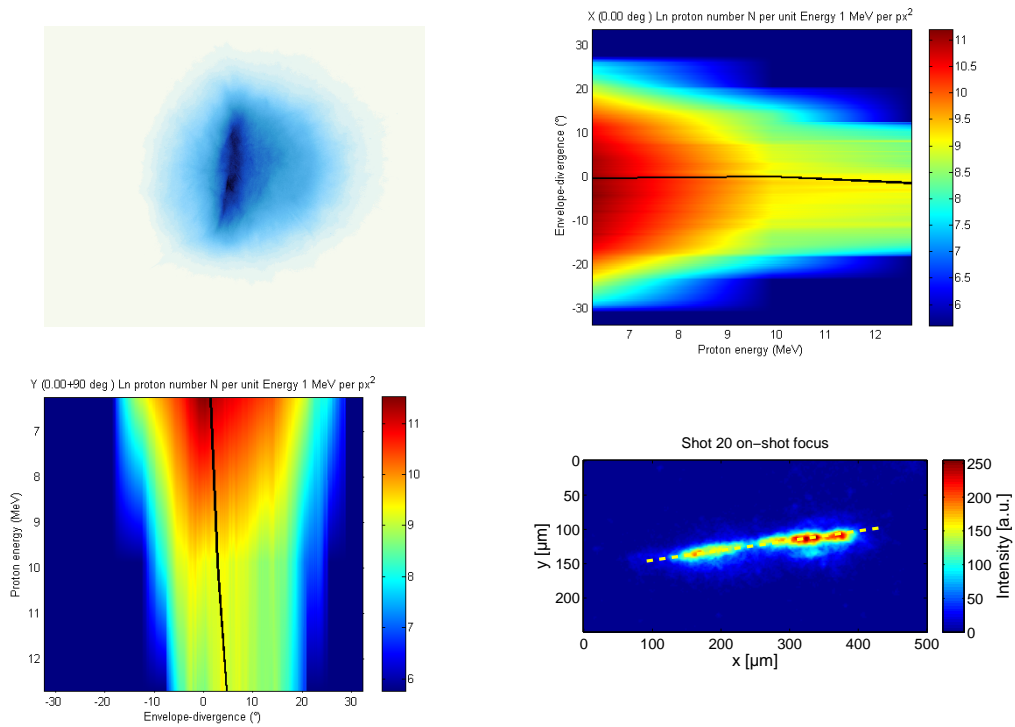


Figure 5.13: Detailed view of the measured protons from shot 20. The first RCF layer is displayed which corresponds to a proton energy of 6.2 MeV. In addition, the average  $x$  and  $y$  proton intensities for the whole stack are illustrated around. The color corresponds to logarithmic proton number in a 1 MeV energy interval per square pixel. It can be observed that the protons are accelerated perpendicular to the major axis of the laser focal line (bottom right).

In the displayed RCF and also in the average proton intensities it can be observed that the protons are accelerated perpendicular to the major axis of the laser focal line (displayed in figure 4.10), i.e. to the rear electron sheath. This is expected because the electron density gradient is steepest in this direction (refer

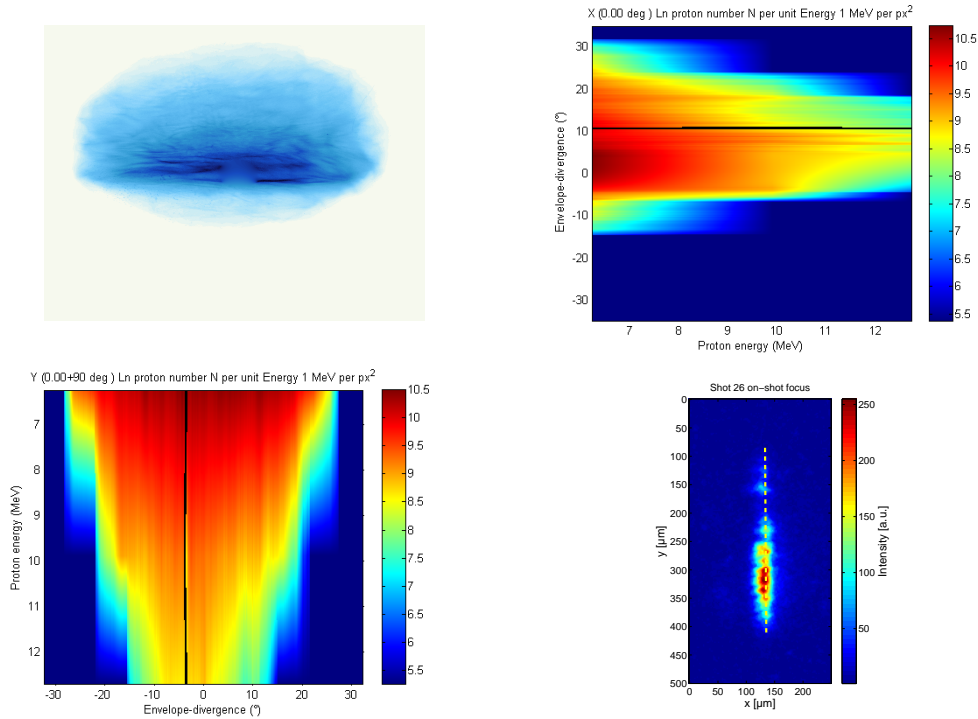


Figure 5.14: Detailed view of the measured protons from shot 26. The first RCF layer is displayed which corresponds to a proton energy of 6.2 MeV. In addition, the average  $x$  and  $y$  proton intensities for the whole stack are illustrated around. The color corresponds to logarithmic proton number in a 1 MeV energy interval per square pixel. It can be observed that the protons are accelerated perpendicular to the major axis of the laser focal line (bottom right).

to section 2.3). The cut-off proton energy is for both shots 12.7 MeV (the last RCF layer with a proton signal) as the lower measured electron temperature in table 5.1 indicates.

## 5.4 TNSA-dependency on focal spot geometry

First the comparison of different focal spot geometries (ring or Gaussian focus) and their effect on the maximum proton energy in the TNSA regime are studied. The maximum proton energy  $E_{proton,max}$  in the case of best (Gaussian) focal spot is proportional to the hot-electron temperature  $k_B T_e$ , which scales as the ponderomotive potential (2.35) with  $k_B T_e \propto \sqrt{a_0^2} \propto \sqrt{I_{laser}}$  [17], and proportional to the electron density  $n_e$ . Only a weakly or not at all scaling with the target thickness or laser pulse duration was also measured by *Robson et al.* [17] for a Gaussian beam.

### 5.4.1 Proton energy dependence on laser intensity

Changing the focal spot geometry from a Gaussian shaped to the smallest ring focal spot ( $2\pi$  phase mask), the focus size is almost doubled and therefore the intensity drops to a quarter if the energy of the laser beam is constant. A larger phase mask (e.g.  $4\pi$ ) reduces the intensity even further by a factor of 1.5. The variation in intensity is induced by different energies delivered from the PHELIX laser system. This leads to the results illustrated in figure 5.15, where the square root of the laser beam intensity is plotted against the maximum proton energy. The intensity is derived from the measured focal spot during alignment before every shot and the on-shot measured laser energy, while the pulse duration is fixed at  $\tau_L = 650$  fs. The maximum proton energy is measured with RCF stacks (see section 5.2). A typical energy detection gap between the last RCF is about 2 MeV and therefore an energy error of +2 MeV is assumed for all shots.

It can be observed that the data points with a Gaussian focal spot (blue) fit very well to the  $E_{protons,max} \propto \sqrt{I_{laser}}$  scaling law from [17] in the range of  $10^{18} \text{ W cm}^{-2}$  to  $10^{20} \text{ W cm}^{-2}$ . The same proportionality is assumed for shots with applied phase mask ( $2\pi$ , green). As illustrated in figure 5.15 a stronger coupling to the laser intensity  $I_{laser}$  can be found in comparison to the shots with the Gaussian focal spot, i.e. the gradient is steeper. Changing to a larger phase mask ( $4\pi$ , turquoise), the gradient is flat again and below the Gaussian one. Also it can be seen that the highest proton energies are reached with

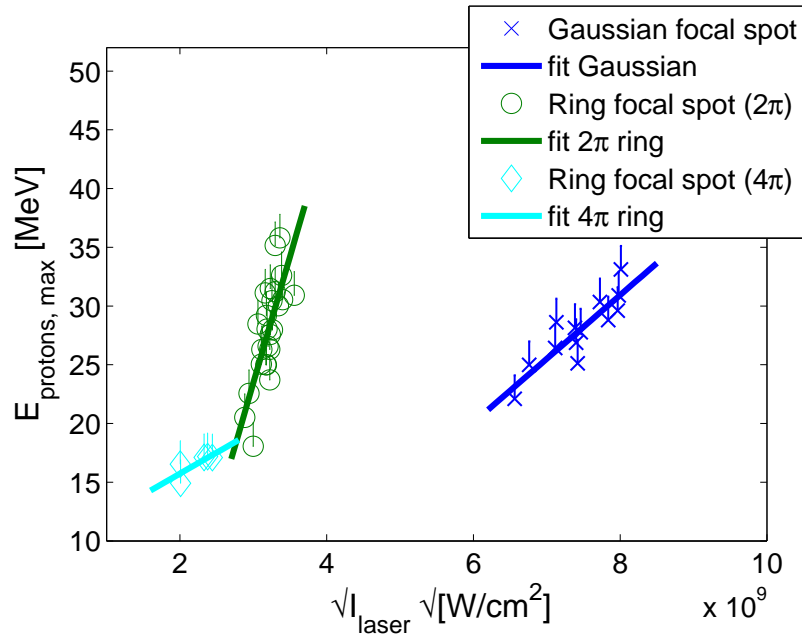


Figure 5.15: The comparison of different focal spot geometries and their effect on the maximum proton energy in the TNSA regime. The scaling law is assessed from [17] as the square root of the laser intensity is proportional to the maximum proton energy. If the phase mask ( $2\pi$ ) for laser beam shaping is applied, a stronger coupling to the laser intensity can be observed (green) in comparison to the shots with the Gaussian focal spot (blue). With a larger phase mask (turquoise) the coupling becomes weaker.

an applied phase mask. One possible explanation for this unexpected feature is, that the larger focal spot can deposit more of its energy inside the plasma and therefore transfer more energy to the accelerating electrons. More electron are accelerated and accumulate at the target rear side. This higher electron numbers lead to a stronger electric field of the electron sheath which in turn can accelerate the protons to higher energies.

### 5.4.2 Proton energy scaling with target thickness

Now, that the dependency on the laser intensity is validated, the interpretation on the target thickness can be done. As explained in section 2.3 the theory predicts an optimum target thickness for shots with an applied phase mask in terms of proton energy. This is illustrated in figure 5.16 where the shots with different target thicknesses are plotted against the maximum proton energy  $E_{protons,max}$  divided by  $\sqrt{I_{laser}}$  to account for the linear dependency.

#### Scaling with different focus geometries

The scaling of the maximum proton energy with different target thicknesses can be observed for shots with an applied phase mask. For thicknesses where more than one experiment was performed, the mean value is considered and the maximum deviation is indicated by the error bars. The lower blue line stands for shots with a normal Gaussian focal spot where no clear dependence on the target thickness can be observed. Compared to the shots with a Gaussian focal spot, shots with a ring focus result in a systematically higher scaled proton energy. The green circled line represents shots with the  $2\pi$  phase mask and the normal PHELIX contrast level. A connection of the maximum proton energy and the target thickness can be observed for targets in the range of  $5\ \mu\text{m}$  to  $20\ \mu\text{m}$ . The measured optimum target thickness range is from  $10\ \mu\text{m}$  to  $17\ \mu\text{m}$  and is slightly below the prediction of the theory of  $14\ \mu\text{m}$  to  $18\ \mu\text{m}$ . Shots with the  $4\pi$  phase mask are drawn in turquoise. In section 2.2.2 the effect of relativistic self focusing is explained. It depends on the pre-plasma and enables the incident laser beam to focus to a tighter spot. An incident ring focus can be confined inside a smaller area in the pre-plasma [91]. This is the interpretation



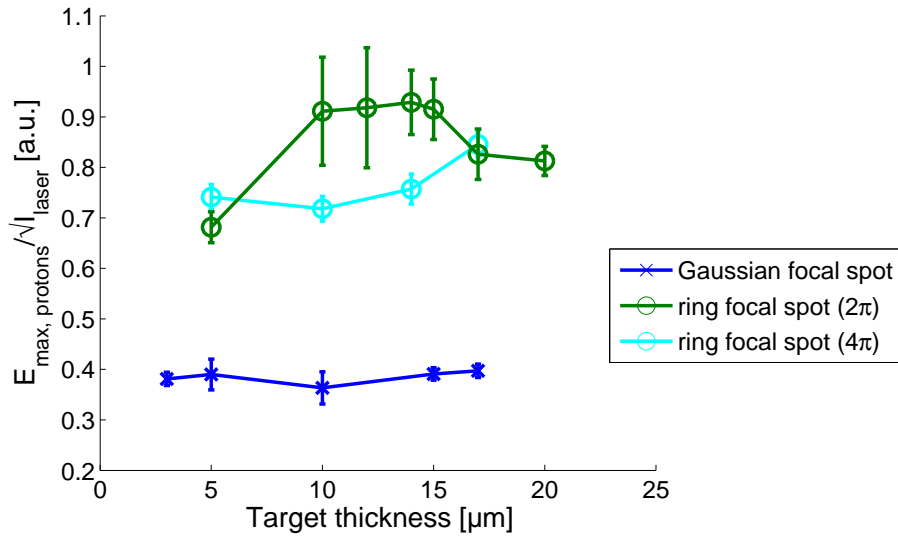


Figure 5.16: Scaling of the maximum proton energy with different target thicknesses. The lower dark blue line stands for shots with a normal Gaussian focal spot. The green, circled line represents shots with the  $2\pi$  phase mask and normal PHELIX contrast level. A connection of the maximum proton energy and the target thickness can be observed. Shots with the  $4\pi$  phase mask are drawn in turquoise.

why the measurements in figure 5.16 imply an optimum by a somehow thinner target than predicted by the theory for shots with a  $2\pi$  phase mask.

As the trend of the turquoise graph indicates, there is an optimum target thickness towards larger thicknesses than probed in the experiment which was up to  $17\ \mu\text{m}$ . It can be understood in a similar way to the explanations made in section 2.3. For a given ring size on the target an optimum target thickness exists, as shown in figure 5.16 for the  $2\pi$  phase mask in green. As the use of the  $4\pi$  phase mask (turquoise) enlarges the focal ring size, a thicker target is needed to generate a flat, accelerating electron sheath on the rear side. So a larger ring favors a thicker target.

### Scaling with different laser contrast levels

In addition, experiments with modified contrast levels were conducted and the results are illustrated in figure 5.17. The green data points were recorded with the best available contrast on the PHELIX laser, i.e. a contrast level of about

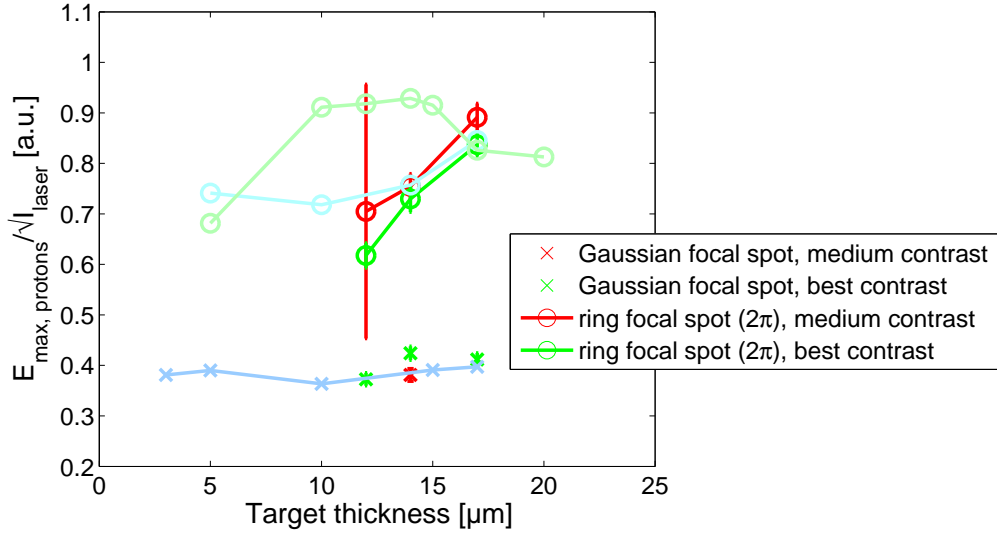


Figure 5.17: Scaling of the maximum proton energy with different target thicknesses and modified contrast level. The light color plots represent shots with normal contrast from figure 5.16 for comparison. The lower green and red data points stands for shots with a normal Gaussian focal spot and altered contrast. Again, no clear dependency on the target thickness can be observed as in figure 5.16. Shots with a ring focus and altered contrast result in a systematically higher scaled proton energy as before and show a target thickness dependency similar shots performed with the  $4\pi$  phase mask.

$10^{-11}$ , while the red correspond to a medium contrast, i.e. roughly a factor of 200 worse than the green. Shots with phase mask (circled) and an altered contrast level are plotted in red and green, medium and best contrast level, respectively, too.

Again, no clear dependency on the target thickness can be observed in the case of a Gaussian focal spot: the data points with the modified contrast level correspond to the previous ones with normal contrast. The trend of the red and green graph indicates that there is an optimum target thickness around  $17 \mu\text{m}$ , as it was observed with an applied  $4\pi$  phase mask. An analogous explanation can be applied to shots with modified contrast and a  $2\pi$  phase mask. As explained before, the relativistic self focusing is responsible for the deviation from the theory in case of the  $2\pi$ , normal contrast shots. The optimum is shifted to thinner targets. Now switching to a higher contrast level, that means reducing the pre-plasma scale, an incident ring focus can not be confined as in

the normal contrast case. This effectively results in a larger ring focal spot on the target. And this is similar to the case with the  $4\pi$  phase mask, favoring a thicker target. So shots with an applied  $2\pi$  phase mask and improved contrast favor also thicker targets. In a simple picture the inertial real target thickness has to be approximated by a virtual target thickness that is from the target rear side to the front critical density surface.

Additionally, a difference between the two contrast levels (medium and best) can be observed. The red (medium contrast) graph is a little above the green (best contrast) line, possibly because the pre-plasma is larger and the incident laser is focused better therein.

### 5.4.3 Envelope divergence with different focal spot geometries and central proton intensities

In section 2.3 the simulations predict a more directed proton beam, if the accelerating electron sheath approaches the desired (flat) shape. That means that fewer protons should be scattered into the border region of the outgoing proton beam from the laser-driven ion acceleration. Analyzing the proton beam size in each RCF layer at a fixed proton intensity should reveal a smaller proton imprint area. This is illustrated in figure 5.18. The threshold for the proton beam boundary was set to a fixed value of 2000 protons per square pixel (one pixel is approximately  $25\ \mu\text{m} \times 25\ \mu\text{m}$ ). This limit was chosen to distinguish clearly from the sometimes occurring high background (mostly electron) signal. Each of the plotted data points represents an RCF layer in a shot and is scaled to the corresponding maximum proton energy for comparison. The scaling by the reached maximum proton energy is necessary because the divergence angle is energy-dependent. Only shots where the target thickness is in the range of the previous determined optimum are considered in the figure. The size of the proton signal in a RCF can be converted to an envelope angle with the measured distance of the RCF stack to the laser-matter interaction.

In figure 5.18 a tendency to achieve a smaller envelope divergence with an applied phase mask can be observed, given by the two average lines (blue for a Gaussian focal spot, green for a ring focal spot). The average reduction is

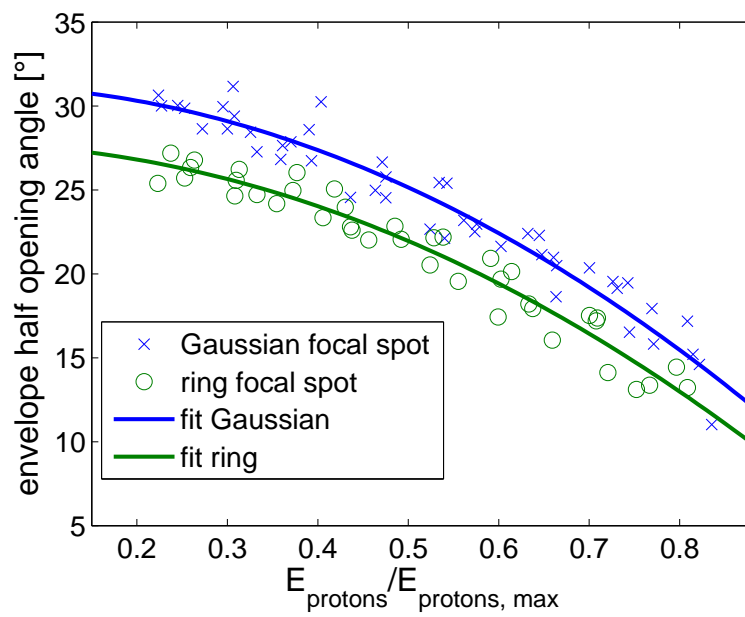


Figure 5.18: The comparison of different focal spot geometries and their effect on the envelope divergence angle. The tendency to achieve a smaller envelope divergence with an applied phase mask can be observed, given by the two average lines (blue for a Gaussian focal spot, green for a ring focal spot). The last layer is always omitted because of the weak proton beam signal therein.

$(3.07 \pm 0.42)^\circ$ . Therefore only  $10\ \mu\text{m}$  to  $17\ \mu\text{m}$  thick targets were considered, i.e. the optimum target thickness determined previously.

## 5.5 Ion acceleration with improved laser beam control

The influence of the laser focal spot shape on the ion acceleration was illustrated with strongly astigmatic laser focuses. But throughout all conducted experiments the laser beam quality was subject of steady change due to the use of the adaptive optics. Before each shot, the laser system alignment was optimized to get the best wave-front and therefore a beam shape closest to the expected hollow beam shape out of the system, i.e. to pre-compensate the occurring on-shot aberrations as good as possible. This was described in section 4.2 in detail. The steady improvements that were carried over the work of this thesis culminate in the best beam quality measured at the PHELIX laser system achieved so far. This became apparent from the boost of the proton maximum energy deduced from the RCF stacks. This set of particular shots, that were measured with the final optimized laser system, are covered in this section.

Figure 5.19 illustrates the comparison of the proton energy spectrum for different shots. Shot 18 and 19 are plotted as an example proton spectrum with “normal” wave-front, while shots 21 to 25 represent the proton spectrum with the final optimized wave-front. A clear improvement in reached maximum proton energy (indicated by the red dashed line) can be observed. Notably the used RCF stacks allowed only proton energy measurement of up to  $34.6\ \text{MeV}$ . Two shots with the hollow beam exceeded this limit and the maximum proton energy was not detected. The RCF stacks were designed that way, because the preceding shots in this experimental campaign did not exceed  $30\ \text{MeV}$  in maximum proton energy. The improved wave-front, as it was deduced from figures 4.8 and 4.11 in the previous chapter, leads to less scattered energy in the focus of the laser. The measurements with the OSFD indicates that in turn less energy is reflected in  $3\omega_L$  laser light. That means that more laser energy was transferred to the electrons in terms of generated electron numbers and they

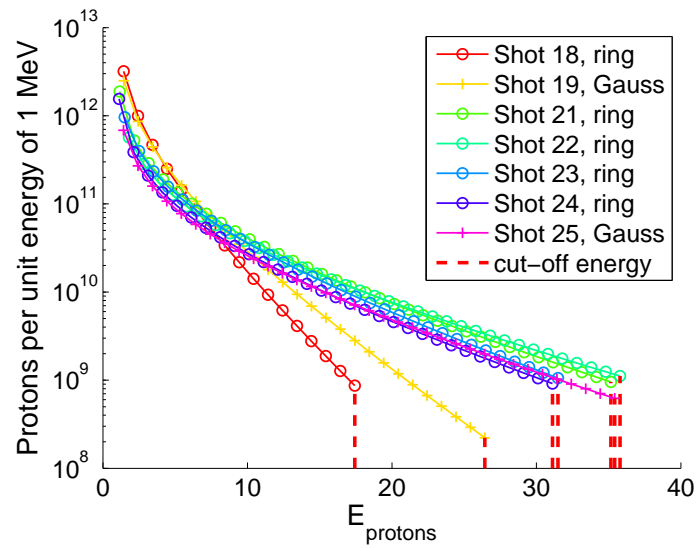


Figure 5.19: Comparison of the proton energy spectrum for different shots. Shot 18 and 19 are plotted for an example proton spectrum with “normal” wave-front, while shots 21 to 25 represent the proton spectrum with improved wave-front. A clear improvement in reached maximum proton energy (indicated by the red dashed line) can be observed. Notably, the used RCF stacks allowed only proton energy measurement of up to 34.6 MeV. Two shots with the hollow beam exceeded this limit.

Table 5.4: Comparison of proton temperature  $k_B T_p$  for the selected shots.

Shot	Focus	$E_{protons,max}$ in MeV	$k_B T_p$ in MeV
18	ring	16.9	$3.10 \pm 0.00$
19	Gauss	26.1	$4.26 \pm 0.11$
21	ring	34.6	$10.22 \pm 0.52$
22	ring	34.6	$11.85 \pm 0.61$
23	ring	32.7	$9.17 \pm 0.43$
24	ring	30.6	$9.47 \pm 0.21$
25	Gauss	34.6	$10.49 \pm 0.36$

create a stronger electric field at the target rear side. This in turn can accelerate the protons to higher energies and is seen in the proton temperature  $k_B T_p$  of equation (5.3) which are tabulated in table 5.4. The values are calculated by the RCF analysis software.

Additionally, in figure 5.20, the central proton intensities are compared for different focal spot geometries. Each data point represents a RCF layer and the therein counted proton numbers in a central part that corresponds to a half opening angle of  $2.5^\circ$ . It is scaled by the maximum proton energy of the corresponding shot for comparison. For this set of shots a tendency to higher proton yield in the center with an applied phase mask can be observed. The increase in the central proton numbers is measured to be  $(57 \pm 38)\%$  higher for the whole spectrum than with the Gaussian focal spot. The explanation is due to the reduced divergence angle and the therefore more directed proton beam. If less protons are scattered to the rim region of the emitted TNSA proton beam, the central intensity of the proton beam increases.

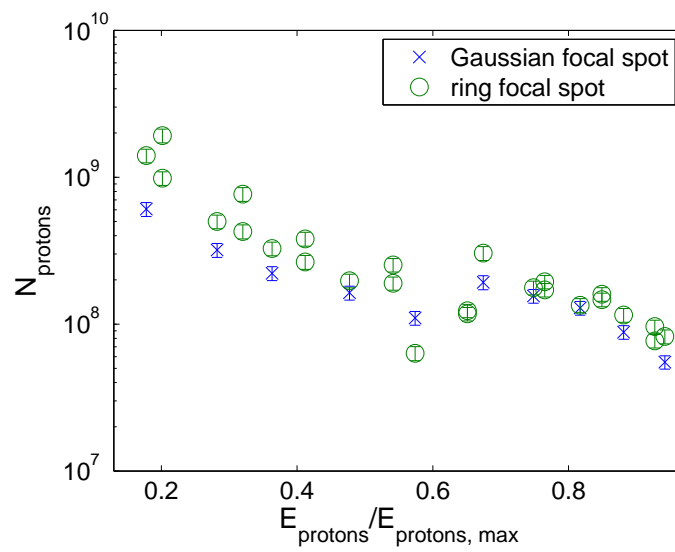


Figure 5.20: The comparison of different focal spot geometries and their effect on the central proton intensity. The jump at around 0,6 scaled proton energy is due to the change in the used RCF films, which have been changed at this energy position from the HD-810 type to the more sensitive EBT3.



# CHAPTER 6

---

## Conclusion

---

In the frame of this thesis laser-driven proton acceleration was studied within the target normal sheath acceleration (TNSA) regime with focus on the beam parameters of the generated proton beam by control of the laser beam. The experiments for this thesis were conducted at the PHELIX laser facility at the GSI Helmholtzzentrum für Schwerionenforschung GmbH. With such a laser system, along with the capability of tight focusing, laser intensities exceeding  $10^{18} \text{ W cm}^{-2}$  could be created on a target. These high intensities can easily ionize atoms of the target and produce a plasma. Electrons inside the plasma partially absorb laser energy, thus getting accelerated and penetrate through the target. On the rear side a strong electric field is generated due to the forming electron sheath. This created electric field ionize atoms of the rear side where a contamination layer is located and the strong charge separation leads to an acceleration of ions, mostly protons. The ions and electrons expand into the vacuum behind the target as a quasi-neutral plasma cloud. This two-staged mechanism (i.e. laser energy is transferred to the electrons and these, in turn, transfer their kinetic energy to the accelerated ions) is called the target normal sheath acceleration. Such particle beams, originating from the target rear side contamination layer, have outstanding properties like ultra-low emittance and a pulse duration in the range of the laser pulse duration. This fact brought up a wide range of application ideas up to new compact particle accelerator schemes and is still subject of current research. Several experimental teams have investigated the involved processes with various laser systems and varying

parameters. But since not all characteristics of the acceleration mechanism are fully understood, it is difficult to create proton beams with controllable and reproducible properties. One drawback of the TNSA generated proton beam is the large opening angle of up to  $60^\circ$ .

The goal of this thesis is to change the initial conditions of the emitted ion beam from the TNSA source, especially the divergence angle. It aims at shaping the rear side electron sheath using specially shaped laser beams. The form of the accelerating electron sheath defines the divergence angle of the ion beam because ion acceleration is normal to the electron sheath. Creating a shaped laser beam, a ring laser focus for this thesis, can be done using specially designed helical phase plates. The result is a hollow focal spot on the target with an intensity minimum in the center. Expected changes of the ion beam for experiments with this kind of focus shape are a reduced opening angle at which the ions are emitted depending on their energy because the electron sheath can be influenced by the initial laser beam profile. The precise control of these initial parameters of a laser-accelerated ion beam is advantageous for most applications.

Therefore it was necessary to study and control the propagation of such a special laser beam through a complete laser amplification beam line. Numerical simulations were developed to assist identifying limitations on the laser beam quality and find possibilities for improvement. A part of this thesis covered therefore measurements of the beam quality (i.e. the wave-front) and its possible control using adaptive optics. Another part concerned particle-in-cell simulations to understand the effects on the TNSA mechanism. With these simulations an optimum target thickness range from  $14\ \mu\text{m}$  to  $18\ \mu\text{m}$  for the laser beam parameters available at PHELIX could be derived to be used with the shaped laser beam.

Two successful experimental campaigns (June 2012 and July 2013) on laser-driven ion acceleration as well as one dedicated beam time (September 2011) for laser wave-front improvements were carried out during this thesis. The main diagnostic for generated protons within the conducted experiments were the radiochromic films (RCF). They are widely used as a diagnostic for laser-accelerated protons because they provide easy and precise measurements of the

proton distribution. These films, combined to a stack of RCF with metal layers in-between, are able to deliver a spatially and spectrally resolved profile of the accelerated proton beam. The analysis software for these films was improved and new functions were developed to obtain 2-dimensional energy-wise resolved particle numbers. This software package yields all essential information that can be extracted of the RCF. In addition to the RCF, a new diagnostic was established that can image the reflected laser light from the laser-matter interaction on the target. It is built to filter all but the frequency tripled ( $3\omega_L$ ) laser light that is created at the critical plasma density surface due to plasma oscillation. Up to now it was assumed to have the same laser intensity distribution on the target as it was measured before a high-energy experiment. With this new implemented imaging system it was possible to image the real laser focal spot on target during the laser-matter interaction with a reasonable quality. As it is shown in this work, there is a difference between the laser focus profile before a shot and on-shot on the target surface.

Up to now, it was the first time that laser-driven ion acceleration was demonstrated with a hollow laser beam. Various effects were observed when the TNSA is driven with a hollow beam focus. First of all the reached maximum proton energy was the same or even higher in the presence of the hollow beam. The laser spot size increases nearly by a factor of two for the ring focus compared to the Gaussian focus. This leads to a decrease in the intensity by a factor of four. Therefore this high proton energies were unexpected, because based on calculations with the scaling law for a Gaussian focal spot, that the reached maximum proton energy scales with the square root of the laser intensity  $E_{protons,max} \propto \sqrt{I_{laser}}$ , lower proton energies were expected for a hollow focus. It was shown that the experiments with a ring focal spot followed the same proportionality but with a steeper slope. One explanation is, that the larger spot of the ring focus can deposit more energy inside the plasma and in turn transfer more laser energy to the electrons that drive the TNSA. More electrons are accelerated and create a stronger electric field at the target rear side. This stronger electric field in turn can accelerate the protons to higher energies that were measured in this work.

Following this scaling, a dependency on the target thickness of the used flat

gold foils was observed. It was predicted by the underlying theory, that there exists an optimum target thickness for ion acceleration with the hollow beam, in terms of envelope divergence, that can be generated at the PHELIX laser. It was experimentally found that targets in the range of  $10\ \mu\text{m}$  to  $17\ \mu\text{m}$  perform best, although the theory predicts an optimum for thicker targets in the range of  $14\ \mu\text{m}$  to  $18\ \mu\text{m}$ . Below or above this optimum target thickness, the reached maximum proton energy drops. A scaling of the maximum proton energy in case of a Gaussian focal spot could not be observed in the range of  $5\ \mu\text{m}$  to  $20\ \mu\text{m}$  target thickness. One possible explanation for the deviation from the theory in terms of target thickness is that the simulations were done in 2D with infinitely good contrast. That means that the laser beam aberrations were not included and also no pre-plasma. In reality the impinging laser creates a pre-plasma and therein the high electron density leads to a self-focusing effect. As seen in the PIC simulations, there is only one optimum target thickness range for a given hollow beam size. Smaller ring sizes prefer thinner targets and larger rings perform better with thicker targets. Therefore a ring focus, confined in a smaller area in the pre-plasma would have its optimum with thinner targets than the simulations suggest because the simulations were conducted without the pre-plasma. These findings are also supported by experiments where a larger ring focus was created or the contrast level of the laser was modified. In these cases it was observed that the reached maximum proton energy was best at the thickest targets ( $17\ \mu\text{m}$ ) that were available for the experiments. A larger ring focus preferred thicker targets and the same holds true for experiments with improved contrast, that means, the generated pre-plasma is much shorter to interact with the main laser pulse. And therefore it has to be treated in the same way as experiments with a larger ring focal spot. In a simple picture the inertial real target thickness has to be approximated by a virtual target thickness that is from the target rear side to the front critical density surface.

The theory predicted also a decrease of the envelope divergence for experiments with the hollow beam. This feature was observed for shots with all target thicknesses, not only for the optimum target range. In the case of the optimum target thickness the effect was roughly a factor two stronger. It was experimentally demonstrated that the half envelope divergence angle could be decreased

by  $(3.07 \pm 0.42)^\circ$  for the optimum target thicknesses or in other words roughly 10%. An increase in the central proton flux was not observable in the majority of the shots. It was first measured when a setting was found for the adaptive optics of the laser system, which was obviously the best situation ever achieved, in terms of the reached maximum proton energy. This successful compensation of the on-shot aberrations and further wave-front optimization finally lead to an increased overall efficiency in the TNSA regime at PHELIX. This is also supported by the higher proton temperature  $k_B T_p$  of these optimized shots.

Hot-electron spectra could be recorded during the experimental campaign. The hot-electron temperature  $k_B T_e$  revealed no obvious difference for shots with and without a hollow beam focus. Expected was, due to the reduced intensity with a hollow focus, to measure also a reduced hot-electron temperature. The absolute electron numbers were not measured within the experiments. The empirical scaling law that the maximum proton energy is approximately ten times the hot-electron temperature  $E_{protons,max} \approx 10k_B T_e$ , fits very well to the measured electron temperatures and maximum proton energies. A strong decrease in electron temperature was observed in the case of a line focus. This kind of focus was generated by an intended misalignment of the last focusing element to study an extreme case of reduced focal spot intensity distribution. It was set up to validate the effect that the protons are accelerated along the strongest gradients in the electron sheath. In a simple theory this is the laser intensity distribution in the focal plane folded with a Gaussian point-spread-function. An elongated laser focal spot generates an elongated electron sheath and the protons are accelerated perpendicular to this sheath, along the strongest gradients. In addition, this extreme case of a focal spot was used to validate the newly implemented on-shot focus diagnostic in terms of imaging quality. It images the frequency up-shifted laser light which is generated at the critical density plasma surface. With this diagnostic the real laser intensity distribution on the target during the laser-matter interaction could be recorded.

## 6.1 Perspectives

Further improvements to the PHELIX laser system beam quality could enhance the effects of laser-driven ion acceleration with a hollow beam, as described in section 5.5. It was demonstrated that the beam quality has an influence on the TNSA, in terms of maximum proton energy, and is a necessary criterion for laser-driven ion acceleration with the hollow beam. The laser beam energy was limited in the conducted experiments due to the chosen laser beam diameter for an optimized beam quality. With further optimization of the wave-front, the propagation of the hollow laser beam through the PHELIX system with larger beam diameters have to be demonstrated. Then it would be possible to extend the scaling of the maximum proton energy with the laser intensity to a higher regime.

Further investigations, experimentally as well as with complex three dimensional PIC simulations, can be based upon this work with focus on the effect of reached higher proton energies in presence of a hollow laser beam. The hot-electron spatial distribution should be measured with multiple magnetic dipole spectrometers in the rim region to validate the model of the flat proton accelerating electron sheath. A proposal is submitted to achieve a grant for a new beam time for a case study where the hollow beam will be replaced by two independent laser focal spots with varying distance. This will allow to study the observed effects in an one-dimensional case and the problem is easier comparable to the two-dimensional simulation results.

The application to the LIGHT project and its benefit to it will be studied in following beam time. If it is possible to reduce the envelope divergence even further, e.g. with an optimized target geometry, this have an influence on structural elements next in line in the sense that less particles are lost due the acceptance of the used ion optics, e.g. the solenoid in the LIGHT proton beam line.

---

## Zusammenfassung

---

Im Rahmen dieser Doktorarbeit wurde die lasergetriebene Protonenbeschleunigung im Bereich der TNSA (*target normal sheath acceleration*) untersucht. Dabei wurde der Schwerpunkt auf die Strahleigenschaften des erzeugten Protonenstrahls mittels Kontrolle des Laserstrahls gelegt. Die Experimente für diese Doktorarbeit sind an dem PHELIX Lasersystem der GSI Helmholtzzentrum für Schwerionenforschung GmbH durchgeführt worden. Mit solch einem Lasersystem und der Möglichkeit einer starken Fokussierung, können Laserintensitäten von über  $10^{18} \text{ W cm}^{-2}$  auf einem Target erzeugt werden. Solch hohe Intensitäten können leicht Atome von einem Target ionisieren und ein Plasma erzeugen. Elektronen innerhalb des Plasmas absorbieren einen Teil der Laserenergie, werden dadurch beschleunigt und können das Target durchdringen. Auf der Rückseite des Targets wird ein starkes elektrisches Feld durch die Ausprägung der Elektronenschicht erzeugt. Mittels Feldionisation werden durch dieses erzeugte elektrische Feld, Atome von den auf der Rückseite befindlichen Verunreinigungen ionisiert und anschließend durch die entstandene starke Ladungstrennung beschleunigt. Die Ionen, hauptsächlich Protonen, und Elektronen expandieren als quasineutrale Plasmawolke in das Vakuum hinter dem Target. Dieser zweischrittige Prozess, d.h. Laserenergie wird an die Elektronen übertragen welche wiederum ihre gewonnene kinetische Energie an die beschleunigten Ionen transferieren, wird *target normal sheath acceleration* genannt. Solche Teilchenstrahlen, die von den Verunreinigungen der Targetrückseite herrühren, haben herausragende Eigenschaften wie besonders kleine Emittanz und Pulslängen, die im Bereich der Laserpulsdauer liegen. Diese Tatsache eröffnete einen weiten Bereich an Anwendungsideen bis hin zu Plänen für neue und kompakte Teilchenbeschleuniger. Das Gebiet der TNSA ist noch immer Gegenstand heutiger Forschung. Mehrere Forschergruppen untersuchten

die beteiligten Prozesse mit verschiedenen Lasersystemen und unterschiedlichen Parametern. Da nicht alle Eigenheiten des verwendeten Beschleunigungsmechanismus vollständig verstanden sind, ist es schwer, Protonenstrahlen mit kontrollierbaren und reproduzierbaren Eigenschaften zu erzeugen. Ein Nachteil des durch TNSA erzeugten Protonenstrahls ist der große Öffnungswinkel von bis zu  $60^\circ$ .

Das Ziel dieser Doktorarbeit besteht darin, die anfänglichen Bedingungen des ausströmenden Ionenstrahls von der TNSA Quelle zu beeinflussen, mit besonderem Blick auf den Divergenzwinkel. Diese Arbeit zielt auf die Beeinflussung der Form der rückseitigen Elektronenschicht mit Hilfe von speziell geformten Laserstrahlen ab. Die Form der beschleunigenden Elektronenschicht definiert den Divergenzwinkel des Ionenstrahls, weil die Ionen senkrecht zu der Elektronenschicht beschleunigt werden. Das Erzeugen von geformten Laserstrahlen, wie für diese Arbeit ein Ringstrahl, kann mittels speziell ausgelegten, spiralförmigen Phasenplatten erreicht werden. Das Ergebnis ist ein ausgehöhlter Fokuspunkt auf dem Target mit einem Intensitätsminimum in der Mitte. Der erwartete Einfluss auf den Ionenstrahl, für Experimente mit dieser Art von Fokus, ist eine Reduktion des Öffnungswinkels unter welchem die Ionen energieabhängig emittiert werden. Die Elektronenschicht wird von den anfänglichen Laserparametern maßgeblich beeinflusst. Die sehr genaue Kontrolle dieser anfänglichen Parameter der lasergetriebenen Ionbeschleunigung ist vorteilhaft für die meisten Anwendungen.

Um die Ausbreitung eines solch speziellen Laserstrahls durch ein komplettes Lasersystem zu untersuchen und zu kontrollieren wurden numerische Simulationen entwickelt, um bei der Identifizierung von Schwachstellen auf die Strahlqualität zu helfen und Möglichkeiten zur Verbesserung zu finden. Ein Teil dieser Arbeit erstreckt sich auf die Messungen der Strahlqualität, d.h. der Wellenfront, und deren mögliche Kontrolle mittels adaptiver Optik. Ein anderer Teil betraf die „Teilchen in einer Zelle“ (*particle in cell*, PIC) Simulationen um den Effekt auf den TNSA Mechanismus zu verstehen. Durch diese Simulationen konnte eine optimale Targetdicke im Bereich von  $14\ \mu\text{m}$  bis  $18\ \mu\text{m}$  für die gegebenen PHELIX Laserparametern bestimmt werden.

Zwei erfolgreiche Experimentkampagnen (im Juni 2012 und Juli 2013), zur



lasergetriebenen Ionenbeschleunigung und auch eine gesonderte Strahlzeit (im September 2011) zur Verbesserung der Wellenfront, wurden während dieser Arbeit durchgeführt. Die Hauptdiagnostik für die erzeugten Protonen während der Experimente waren radiochromatische Filme (RCF). Diese sind weithin verbreitet als Diagnostik für laserbeschleunigte Protonen, weil diese eine einfache und genaue Messung der Protonenverteilung erlauben. Diese Filme, zusammengesetzt zu einem Stapel aus RCF mit Metallplättchen, ermöglichen die Erfassung der spektralen und räumlichen Verteilung der beschleunigten Protonen. Die Software zur Auswertung der Filme wurde verbessert und es wurden neue Funktionen implementiert, um die energieaufgelösten, zwei-dimensionalen Teilchenzahlen zu erhalten. Das komplette Softwarepaket liefert alle wichtigen Informationen, die aus den RCF gewonnen werden können. Zusätzlich zu den RCF wurde eine neue Diagnostik eingerichtet, mit deren Hilfe das reflektierte Laserlicht von der Laser-Materie-Wechselwirkung auf dem Target abgebildet werden kann. Diese ist so aufgebaut, dass alles außer dem frequenzverdreifachten ( $3\omega_L$ ) Laserlicht geblockt wird, welches an der kritischen Plasmadichte durch Plasmaoszillationen erzeugt wird. Bisher wurde angenommen, dass dieselbe Laserintensitätsverteilung bei einem Hochenergie-Experiment auf das Target trifft, als zuvor im Justagemodus gemessen wurde. Mit diesem neu eingebauten Abbildungssystem war es möglich den realen Laserfokus während der Laser-Materie-Wechselwirkung mit guter Qualität zu messen. Wie in dieser Arbeit gezeigt wird, besteht ein Unterschied zwischen dem Laserfokus gemessen vor einem Schuss und während eines Schusses auf dem Target.

Es war das erste Mal, dass Experimente zu lasergetriebener Ionenbeschleunigung mit einem Hohlstrahl durchgeführt wurden. Verschiedene Effekte konnten bei der TNSA mit einem Hohlstrahl beobachtet werden. Die erreichte maximale Protonenenergie war gleich oder sogar höher mit dem Hohlstrahl, obwohl die Fokusgröße sich für den Ringfokus verdoppelt im Vergleich zu einem Gaußschen Fokus. Das führt zu einer Reduktion der Intensität um einen Faktor vier. Deswegen waren diese hohen Protonenenergien unerwartet, denn ausgehend von Berechnungen mit einem Skalierungsgesetz für einen Gaußschen Fokus, dass die maximale Protonenenergie mit der Quadratwurzel der Laserintensität skaliert  $E_{protons,max} \propto \sqrt{I_{laser}}$ , wurden geringere Protonenenergien

für den Hohlstrahl erwartet. Es konnte aufgezeigt werden, dass die Experimente mit einem Ringstrahl derselben Proportionalität folgen aber eine steilere Steigung gemessen wurde. Eine Erklärung für dieses Verhalten ist, dass der größere Ringfokus mehr Energie in dem Plasma deponieren kann und daher mehr Laserenergie an die Elektronen transferieren kann. Mehr Elektronen werden beschleunigt und erzeugen somit ein stärkeres elektrisches Feld auf der Targetrückseite. Dieses stärkere elektrische Feld kann wiederum die Protonen auf höhere Energien beschleunigen, wie es in dieser Arbeit gemessen wurde.

Dieser Proportionalität folgend konnte eine Abhängigkeit von der Dicke der benutzten flachen, Goldfolien-Targets beobachtet werden. Von der zugrunde liegenden Theorie wurde vorhergesagt, dass es eine optimale Targetdicke für Ionenbeschleunigung mit dem Hohlstrahl gibt, im Sinne von optimiertem Divergenzwinkel. Experimentell bestätigt wurde, dass Targets in einem Bereich von  $10\ \mu\text{m}$  bis  $17\ \mu\text{m}$  am besten funktionieren, obwohl die Theorie das Optimum bei dickeren Targets von  $14\ \mu\text{m}$  bis  $18\ \mu\text{m}$  prognostiziert hat. Unter- oder oberhalb dieser optimalen Targetdicke, brach die maximale Protonenenergie ein. Eine Skalierung der maximalen Protonenenergie mit der Targetdicke konnte für einen Gaußschen Fokus für Targets im Bereich von  $5\ \mu\text{m}$  bis  $20\ \mu\text{m}$  nicht beobachtet werden. Eine Erklärung für die Abweichung von der Theorie bezüglich der Targetdicke ist darin begründet, dass die Simulationen in 2D mit unendlich gutem Kontrast durchgeführt wurden. Das bedeutet, dass die Aberrationen des Laserstrahls nicht berücksichtigt wurden genauso wenig wie das Vorplasma. In der Realität erzeugt der aufprallende Laser ein Vorplasma und wird durch die darin hohe Elektronendichte selbstfokussiert. Wie in den PIC Simulationen gezeigt, existiert nur ein optimaler Targetdickenbereich für eine bestimmte Hohlstrahlgröße. Kleinere Ringdurchmesser bevorzugen dünnere Targets und größere Ringe funktionieren besser mit dickeren Targets. Deshalb hat ein Ringfokus, eingeschlossen in einem kleineren Bereich im Vorplasma, auch sein Optimum bei dünneren Targets als die Simulation vorhersagt, da diese ohne Vorplasma durchgeführt wurden. Diese Erkenntnis wird ebenso durch Experimente unterstützt bei denen ein größerer Ringfokus verwendet oder das Kontrastlevel des Lasers verändert wurde. In diesen Fällen wurde die maximale Protonenenergie bei den dicksten zur Verfügung stehenden Targets ( $17\ \mu\text{m}$ )

beobachtet. Ein größerer Ringfokus bevorzugt dickere Targets und dies gilt auch für Experimente mit verbessertem Kontrastlevel. Das generierte Vorplasma, mit dem der Laserpuls wechselwirkt, ist dadurch viel kleiner. Daher kann es auf die selbe Art und Weise erklärt werden wie die Experimente mit einem größeren Ringfokus. Das kleinere Vorplasma kann den Ringstrahl nicht so stark selbstfokussieren. Bildlich gesprochen muss die anfängliche, reale Targetdicke durch eine virtuelle Targetdicke angenähert werden, die sich von der Rückseite des Targets bis zur kritischen Dichte an der Vorderseite erstreckt.

Die Theorie sagt ebenfalls eine Reduktion der Divergenz für Experimente mit dem Hohlstrahl voraus. Dieses Merkmal konnte bei allen Schüssen mit allen Targetdicken beobachtet werden und nicht nur für optimale Targetdicken. Im Falle der optimalen Targetdicken war dieser Effekt etwa doppelt so stark ausgeprägt. Es wurde experimentell gemessen, dass bei optimalen Targetdicken der halbe Öffnungswinkel um  $(3,07 \pm 0,42)^\circ$  reduziert werden konnte, was in etwa 10% entspricht. Eine Erhöhung des Protonenflusses im zentralen Bereich konnte in den meisten Schüssen nicht beobachtet werden. Dieser Effekt konnte erst gemessen werden als eine Einstellung der adaptiven Optik gefunden worden ist, die offensichtlich die jemals beste, erreichte Situation darstellt. Dies wird durch die erreichte maximale Protonenenergie belegt. Die erfolgreiche Vorkompensation zusammen mit den ständigen Verbesserungen der Wellenfront führten schlussendlich zu einer gesamt erhöhten Effizienz der TNSA an PHELIX. Das wird ebenfalls durch die höhere Protontemperatur  $k_B T_p$  dieser optimierten Schüsse unterstützt.

Spektren heißer Elektronen wurden ebenfalls während der Experimentkampagnen gemessen. Allerdings konnte kein offensichtlicher Unterschied bei den Temperaturen der heißen Elektronen  $k_B T_e$  für Schüsse mit und ohne den Hohlstrahl ermittelt werden. Es wurde erwartet, dass der Reduktion der Intensität mit einem Hohlstrahl, auch eine Reduktion der Temperatur der heißen Elektronen folgt. Die absolute Anzahl an Elektronen wurden nicht in den Experimenten gemessen. Ein empirisches Skalierungsgesetz besagt, dass die maximale Protonenenergie ungefähr zehnmals der Temperatur der heißen Elektronen entspricht  $E_{protons,max} \approx 10k_B T_e$ . Dies passt sehr gut zu den gemessenen Elektronentemperaturen und maximalen Protonenenergien. Ein starker Rückgang der

Elektronentemperatur konnte im Fall eines Linienfokus gemessen werden. Dieser Linienfokus, mittels einer beabsichtigten Schiefstellung des letzten fokussier Elements eingestellt, stellte eine extreme Situation reduzierter Fokusintensität dar. Dadurch konnte validiert werden, dass die Protonen entlang der stärksten Gradienten in der Elektronenschicht beschleunigt werden. In einer einfachen Annahme entspricht die Elektronenschicht der Laserintensitätsverteilung im Fokus gefaltet mit einer Gaußschen Punkt-Spreitz-Funktion. Ein lang gezogener Fokus erzeugt eine lang gezogene Elektronenschicht welche die Protonen senkrecht zu dieser Schicht beschleunigt, entlang der stärksten Gradienten. Zusätzlich wurde mit diesem Extremfall eines Fokus die Abbildungsqualität, der neu eingerichteten Fokusdiagnostik überprüft. Diese bildet das frequenzverdreifachte Laserlicht, welches an der kritischen Plasmadichte erzeugt wird, ab. Mithilfe dieser Diagnostik war es möglich die reale Laserintensitätsverteilung auf dem Target während der Laser-Materie-Wechselwirkung zu messen.

---

## Bibliography

---

- [1] Donna Strickland and Gerard Mourou. Compression of amplified chirped optical pulses. *Optics Communications*, 56(3):219 – 221, December 1985.
- [2] R. A. Snavely, M. H. Key, S. P. Hatchett, T. E. Cowan, M. Roth, T. W. Phillips, M. A. Stoyer, E. A. Henry, T. C. Sangster, M. S. Singh, S. C. Wilks, A. MacKinnon, A. Offenberger, D. M. Pennington, K. Yasuike, A. B. Langdon, B. F. Lasinski, J. Johnson, M. D. Perry, and E. M. Campbell. Intense high-energy proton beams from petawatt-laser irradiation of solids. *Phys. Rev. Lett.*, 85(14):2945–2948, October 2000.
- [3] Stephen P. Hatchett, Curtis G. Brown, Thomas E. Cowan, Eugene A. Henry, Joy S. Johnson, Michael H. Key, Jeffrey A. Koch, A. Bruce Langdon, Barbara F. Lasinski, Richard W. Lee, Andrew J. Mackinnon, Deanna M. Pennington, Michael D. Perry, Thomas W. Phillips, Markus Roth, T. Craig Sangster, Mike S. Singh, Richard A. Snavely, Mark A. Stoyer, Scott C. Wilks, and Kazuhito Yasuike. Electron, photon, and ion beams from the relativistic interaction of petawatt laser pulses with solid targets. *Physics of Plasmas*, 7(5):2076–2082, May 2000.
- [4] Bruce A. Remington, David Arnett, R. Paul, Drake, and Hideaki Takabe. Modeling astrophysical phenomena in the laboratory with intense lasers. *Science*, 284(5419):1488–1493, May 1999.
- [5] T. H. Maiman. Stimulated optical radiation in ruby. *Nature*, 187:493–494, August 1960.
- [6] R. Decoste and B. H. Ripin. High-energy ion expansion in laser-plasma interactions. *Phys. Rev. Lett.*, 40(1):34–37, January 1978.

- [7] G. Malka and J. L. Miquel. Experimental confirmation of ponderomotive-force electrons produced by an ultrarelativistic laser pulse on a solid target. *Phys. Rev. Lett.*, 77(1):75–78, July 1996.
- [8] C. Gahn, G. D. Tsakiris, A. Pukhov, J. Meyer-ter Vehn, G. Pretzler, P. Thirolf, D. Habs, and K. J. Witte. Multi-mev electron beam generation by direct laser acceleration in high-density plasma channels. *Phys. Rev. Lett.*, 83(23):4772–4775, December 1999.
- [9] T. E. Cowan, J. Fuchs, H. Ruhl, A. Kemp, P. Audebert, M. Roth, R. Stephens, I. Barton, A. Blažević, E. Brambrink, J. Cobble, J. Fernández, J.-C. Gauthier, M. Geissel, M. Hegelich, J. Kaae, S. Karsch, G. P. Le Sage, S. Letzring, M. Manclossi, S. Meyroneinc, A. Newkirk, H. Pépin, and N. Renard-LeGalloudec. Ultralow emittance, multi-mev proton beams from a laser virtual-cathode plasma accelerator. *Phys. Rev. Lett.*, 92(20):204801, May 2004.
- [10] L. Romagnani, J. Fuchs, M. Borghesi, P. Antici, P. Audebert, F. Ceccherini, T. Cowan, T. Grismayer, S. Kar, A. Macchi, P. Mora, G. Pretzler, A. Schiavi, T. Toncian, and O. Willi. Dynamics of electric fields driving the laser acceleration of multi-mev protons. *Phys. Rev. Lett.*, 95:195001, October 2005.
- [11] A. Pukhov. Three-dimensional simulations of ion acceleration from a foil irradiated by a short-pulse laser. *Phys. Rev. Lett.*, 86(16):3562–3565, April 2001.
- [12] S. Busold, A. Almomani, V. Bagnoud, W. Barth, S. Bedacht, A. Blažević, O. Boine-Frankenheim, C. Brabetz, T. Burris-Mog, T.E. Cowan, O. Depert, M. Droba, H. Eickhoff, U. Eisenbarth, K. Harres, G. Hoffmeister, I. Hofmann, O. Jäckel, R. Jäger, M. Joost, S. Kraft, F. Kroll, M. Kaluza, O. Kester, Z. Lecz, T. Merz, F. Nürnberg, H. Al-Omari, A. Orzhekhovskaya, G. Paulus, J. Polz, U. Ratzinger, M. Roth, G. Schumann, P. Schmidt, U. Schramm, G. Schreiber, D. Schumacher, T. Stöhlker, A. Tauschwitz, W. Vinzenz, F. Wagner, S. Yaramyshev, and B. Zielbauer. Shaping laser accelerated ions for future applications -

- The LIGHT collaboration. *Nuclear Instruments and Methods in Physics Research Section A: Accelerators, Spectrometers, Detectors and Associated Equipment*, 740:94–98, March 2014.
- [13] S. C. Wilks, A. B. Langdon, T. E. Cowan, M. Roth, M. Singh, S. Hatchett, M. H. Key, D. Pennington, A. MacKinnon, and R. A. Snavely. Energetic proton generation in ultra-intense laser–solid interactions. *Physics of Plasmas*, 8(2):542–549, 2001.
- [14] P. Mora. Plasma expansion into a vacuum. *Phys. Rev. Lett.*, 90:185002, May 2003.
- [15] M. Passoni and M. Lontano. Theory of light-ion acceleration driven by a strong charge separation. *Phys. Rev. Lett.*, 101:115001, September 2008.
- [16] E. L. Clark, K. Krushelnick, M. Zepf, F. N. Beg, M. Tatarakis, A. Machacek, M. I. K. Santala, I. Watts, P. A. Norreys, and A. E. Dangor. Energetic heavy-ion and proton generation from ultraintense laser-plasma interactions with solids. *Phys. Rev. Lett.*, 85(8):1654–1657, August 2000.
- [17] L. Robson, P. T. Simpson, R. J. Clarke, K. W. D. Ledingham, F. Lindau, O. Lundh, T. McCanny, P. Mora, D. Neely, C.-G. Wahlstrom, M. Zepf, and P. McKenna. Scaling of proton acceleration driven by petawatt-laser-plasma interactions. *Nat Phys*, 3(1):58–62, January 2007.
- [18] F. Nürnberg, M. Schollmeier, E. Brambrink, A. Blažević, D. C. Carroll, K. Flippo, D. C. Gautier, M. Geißel, K. Harres, B. M. Hegelich, O. Lundh, K. Markey, P. McKenna, D. Neely, J. Schreiber, and M. Roth. Radiochromic film imaging spectroscopy of laser-accelerated proton beams. *Review of Scientific Instruments*, 80(3):–, March 2009.
- [19] M. Zepf, E. L. Clark, F. N. Beg, R. J. Clarke, A. E. Dangor, A. Gopal, K. Krushelnick, P. A. Norreys, M. Tatarakis, U. Wagner, and M. S. Wei. Proton acceleration from high-intensity laser interactions with thin foil targets. *Phys. Rev. Lett.*, 90(6):064801, February 2003.

- [20] H. Schwoerer, S. Pfotenhauer, O. Jackel, K.-U. Amthor, B. Liesfeld, W. Ziegler, R. Sauerbrey, K. W. D. Ledingham, and T. Esirkepov. Laser-plasma acceleration of quasi-monoenergetic protons from microstructured targets. *Nature*, 439(7075):445–448, January 2006.
- [21] J. Fuchs, T. E. Cowan, P. Audebert, H. Ruhl, L. Gremillet, A. Kemp, M. Allen, A. Blažević, J.-C. Gauthier, M. Geissel, M. Hegelich, S. Karsch, P. Parks, M. Roth, Y. Sentoku, R. Stephens, and E. M. Campbell. Spatial uniformity of laser-accelerated ultrahigh-current mev electron propagation in metals and insulators. *Phys. Rev. Lett.*, 91(25):255002, December 2003.
- [22] M. Roth, E. Brambrink, P. Audebert, A. Blažević, R. Clarke, J. Cobble, T.E. Cowan, J. Fernández, J. Fuchs, M. Geissel, D. Habs, M. Hegelich, S. Karsch, K. Ledingham, D. Neely, H. Ruhl, T. Schlegel, and J. Schreiber. Laser accelerated ions and electron transport in ultra-intense laser matter interaction. *Laser and Particle Beams*, 23:95–100, October 2005.
- [23] K. Sueda, G. Miyaji, N. Miyanaga, and M. Nakatsuka. Laguerre-gaussian beam generated with a multilevel spiral phase plate for high intensity laser pulses. *Opt. Express*, 12(15):3548–3553, July 2004.
- [24] Norman Hodgson and Horst Weber. *Laser Resonators and Beam Propagation*. Springer Berlin / Heidelberg, 2 edition, 2005.
- [25] Max Born and Emil Wolf. *Principles of Optics*. Cambridge University Press, 7 edition, 2002.
- [26] E. Hecht. *Optik*. Oldenbourg Wissenschaftsverlag GmbH, 4 edition, 2005.
- [27] Jürgen Eichler and Hans Joachim Eichler. *Laser*. Springer Berlin / Heidelberg, 6 edition, 2006.
- [28] E. Wolfe and W. Marchand. Comparison of the kirchhoff and the rayleigh-sommerfeld theories of diffraction at an aperture. *J. Opt. Soc. Am.*, 54(5):587–594, 1964.



- [29] Stuart A. Collins, jr. Lens-system diffraction integral written in terms of matrix optics. *J. Opt. Soc. Am.*, 60(9):1168–1177, 1970.
- [30] F. Pedrotti, L. Pedrotti, W. Bausch, and H. Schmidt. *Optik fr Ingenieure*. Springer Berlin / Heidelberg, 3 edition, 2005.
- [31] Ram Oron, Nir Davidson, Asher A. Friesem, and Erez Hasman. Efficient formation of pure helical laser beams. *Optics Communications*, 182(1-3):205 – 208, August 2000.
- [32] Takahiro Kuga, Yoshio Torii, Noritsugu Shiokawa, Takuya Hirano, Yukiko Shimizu, and Hiroyuki Sasada. Novel optical trap of atoms with a doughnut beam. *Phys. Rev. Lett.*, 78(25):4713–4716, June 1997.
- [33] Virendra N. Mahajan. Strehl ratio for primary aberrations in terms of their aberration variance. *J. Opt. Soc. Am.*, 73(6):860–861, 1983.
- [34] J. Y. Wang and D. E. Silva. Wave-front interpretation with zernike polynomials. *Appl. Opt.*, 19(9):1510–1518, May 1980.
- [35] James C. Wyant. Basic wavefront aberration theory for optical metrology. In James C. Wyant Robert R. Shannon, editor, *Applied Optics and Optical Engineering*, volume 11. Academic Press, 1992.
- [36] Andrea Macchi. *A Superintense Laser-Plasma Interaction Theory Primer*. Springer Berlin / Heidelberg, 1 edition, 2013.
- [37] Ulrich Stroth. *Plasmaphysik*. Vieweg+Teubner Verlag, 1 edition, 2011.
- [38] Alexander Piel. *Plasma Physics*. Springer Berlin / Heidelberg, 2010.
- [39] Francis F. Chen. *Introduction to Plasma Physics and Controlled Fusion*, volume 1. Springer Science+Business Media, 2 edition, 1983.
- [40] Marius S. Schollmeier. *Optimization and control of laser-accelerated proton beams*. PhD thesis, Technische Universität Darmstadt, Germany, October 2008.

- [41] S. C. Wilks, W. L. Kruer, M. Tabak, and A. B. Langdon. Absorption of ultra-intense laser pulses. *Phys. Rev. Lett.*, 69(9):1383–1386, August 1992.
- [42] Erik Lefebvre and Guy Bonnaud. Transparency/opacity of a solid target illuminated by an ultrahigh-intensity laser pulse. *Phys. Rev. Lett.*, 74(11):2002–2005, March 1995.
- [43] A. Pukhov and J. Meyer-ter Vehn. Relativistic magnetic self-channeling of light in near-critical plasma: Three-dimensional particle-in-cell simulation. *Phys. Rev. Lett.*, 76(21):3975–3978, May 1996.
- [44] M. Borghesi, A. J. MacKinnon, L. Barringer, R. Gaillard, L. A. Gizzi, C. Meyer, O. Willi, A. Pukhov, and J. Meyer-ter Vehn. Relativistic channeling of a picosecond laser pulse in a near-critical preformed plasma. *Phys. Rev. Lett.*, 78(5):879–882, February 1997.
- [45] Scott C. Wilks and W.L. Kruer. Absorption of ultrashort, ultra-intense laser light by solids and overdense plasmas. *Quantum Electronics, IEEE Journal of*, 33(11):1954–1968, November 1997.
- [46] Peter Mulser and Dieter Bauer. *High Power Laser-Matter Interaction*. Springer Berlin / Heidelberg, 1 edition, 2010.
- [47] F. Brunel. Not-so-resonant, resonant absorption. *Phys. Rev. Lett.*, 59(1):52–55, July 1987.
- [48] D. Bauer and P. Mulser. Vacuum heating versus skin layer absorption of intense femtosecond laser pulses. *Physics of Plasmas*, 14(2):–, February 2007.
- [49] M. N. Quinn, D. C. Carroll, X. H. Yuan, P. McKenna, K. Markey, S. Kar, M. Zepf, M. Günther, K. Harres, F. Nürnberg, M. Roth, K. L. Lancaster, and D. Neely. Spatial intensity mapping of petawatt laser focus into fast electron transport. *Central Laser Facility annual report*, -:60–62, 2008.

- [50] Yong-sheng Huang, Xiao-fei Lan, Xiao-jiao Duan, Zhi-xin Tan, Nai-yan Wang, Yi-jin Shi, Xiu-zhang Tang, and Ye-xi He. Hot-electron recirculation in ultraintense laser pulse interactions with thin foils. *Physics of Plasmas*, 14(10):–, October 2007.
- [51] M. H. Key, M. D. Cable, T. E. Cowan, K. G. Estabrook, B. A. Hammel, S. P. Hatchett, E. A. Henry, D. E. Hinkel, J. D. Kilkenny, J. A. Koch, W. L. Kruer, A. B. Langdon, B. F. Lasinski, R. W. Lee, B. J. MacGowan, A. MacKinnon, J. D. Moody, M. J. Moran, A. A. Offenberger, D. M. Pennington, M. D. Perry, T. J. Phillips, T. C. Sangster, M. S. Singh, M. A. Stoyer, M. Tabak, G. L. Tietbohl, M. Tsukamoto, K. Wharton, and S. C. Wilks. Hot electron production and heating by hot electrons in fast ignitor research. *Physics of Plasmas*, 5(5):1966–1972, May 1998.
- [52] J. Fuchs, P. Antici, E. d’Humieres, E. Lefebvre, M. Borghesi, E. Brambrink, C. A. Cecchetti, M. Kaluza, V. Malka, M. Manclossi, S. Meyroneinc, P. Mora, J. Schreiber, T. Toncian, H. Pepin, and P. Audebert. Laser-driven proton scaling laws and new paths towards energy increase. *Nat Phys*, 2(1):48–54, January 2006.
- [53] P. A. Norreys, M. Santala, E. Clark, M. Zepf, I. Watts, F. N. Beg, K. Krushelnick, M. Tatarakis, A. E. Dangor, X. Fang, P. Graham, T. McCanny, R. P. Singhal, K. W. D. Ledingham, A. Creswell, D. C. W. Sanderson, J. Magill, A. Machacek, J. S. Wark, R. Allott, B. Kennedy, and D. Neely. Observation of a highly directional  $\gamma$ -ray beam from ultrashort, ultraintense laser pulse interactions with solids. *Physics of Plasmas*, 6(5):2150–2156, May 1999.
- [54] M. Roth, A. Blazevic, M. Geissel, T. Schlegel, T. E. Cowan, M. Allen, J.-C. Gauthier, P. Audebert, J. Fuchs, J. Meyer-ter Vehn, M. Hegelich, S. Karsch, and A. Pukhov. Energetic ions generated by laser pulses: A detailed study on target properties. *Phys. Rev. ST Accel. Beams*, 5:061301, June 2002.

- [55] F. Brandl, G. Pretzler, D. Habs, and E. Fill. Čerenkov radiation diagnostics of hot electrons generated by fs-laser interaction with solid targets. *EPL (Europhysics Letters)*, 61(5):632, March 2003.
- [56] J. Schreiber, M. Kaluza, F. Grüner, U. Schramm, B.M. Hegelich, J. Cobble, M. Geissler, E. Brambrink, J. Fuchs, P. Audebert, D. Habs, and K. Witte. Source-size measurements and charge distributions of ions accelerated from thin foils irradiated by high-intensity laser pulses. *Applied Physics B*, 79(8):1041–1045, October 2004.
- [57] Frank Nürnberg. *Laser-Accelerated Proton Beams as a New Particle Source*. PhD thesis, Technische Universität Darmstadt, Germany, November 2010.
- [58] M. Hegelich, S. Karsch, G. Pretzler, D. Habs, K. Witte, W. Guenther, M. Allen, A. Blažević, J. Fuchs, J. C. Gauthier, M. Geissel, P. Audebert, T. Cowan, and M. Roth. MeV ion jets from short-pulse-laser interaction with thin foils. *Phys. Rev. Lett.*, 89(8):085002, August 2002.
- [59] Matthew Allen, Pravesh K. Patel, Andrew Mackinnon, Dwight Price, Scott Wilks, and Edward Morse. Direct experimental evidence of back-surface ion acceleration from laser-irradiated gold foils. *Phys. Rev. Lett.*, 93(26):265004, December 2004.
- [60] Claudio Perego, Alessandro Zani, Dimitri Batani, and Matteo Passoni. Extensive comparison among target normal sheath acceleration theoretical models. *Nuclear Instruments and Methods in Physics Research Section A: Accelerators, Spectrometers, Detectors and Associated Equipment*, 653(1):89–93, October 2011.
- [61] M. Tampo, S. Awano, P. R. Bolton, K. Kondo, K. Mima, Y. Mori, H. Nakamura, M. Nakatsutsumi, R. B. Stephens, K. A. Tanaka, T. Tanimoto, T. Yabuuchi, and R. Kodama. Correlation between laser accelerated MeV proton and electron beams using simple fluid model for target normal sheath acceleration. *Physics of Plasmas*, 17(7):–, July 2010.

- [62] D. C. Carroll, P. McKenna, O. Lundh, F. Lindau, C.-G. Wahlström, S. Bandyopadhyay, D. Pepler, D. Neely, S. Kar, P. T. Simpson, K. Markey, M. Zepf, C. Bellei, R. G. Evans, R. Redaelli, D. Batani, M. H. Xu, and Y. T. Li. Active manipulation of the spatial energy distribution of laser-accelerated proton beams. *Phys. Rev. E*, 76(6):065401, December 2007.
- [63] M. Schollmeier, K. Harres, F. Nurnberg, A. Blažević, P. Audebert, E. Brambrink, J. C. Fernandez, K. A. Flippo, D. C. Gautier, M. Geissel, B. M. Hegelich, J. Schreiber, and M. Roth. Laser beam-profile impression and target thickness impact on laser-accelerated protons. *Physics of Plasmas*, 15(5):053101, 2008.
- [64] Joseph W. Goodman. *Introduction to Fourier Optics*. Electrical and Computer Engineering. McGraw-Hill, 2 edition, 1996.
- [65] Jason D. Schmidt. *Numerical Simulation of Optical Wave Propagation*. SPIE, 2010.
- [66] David Voelz. *Computational fourier optics*. Tutorial Texts. SPIE, 2011.
- [67] Hartmut Ruhl. Classical particle simulations with the psc code. Web, 2009. Available online, visited on January 8th 2014.
- [68] John M. Dawson. Particle simulation of plasmas. *Rev. Mod. Phys.*, 55(2):403–447, April 1983.
- [69] D. Tskhakaya, K. Matyash, R. Schneider, and F. Taccogna. The particle-in-cell method. *Contrib. Plasma Phys.*, 47(8-9):563–594, December 2007.
- [70] C. K. Birdsall and A. B. Langdon. *Plasma Physics via Computer Simulation*. Plasma Physics. Taylor & Francis, 2005.
- [71] V. Bagnoud, B. Aurand, A. Blažević, S. Borneis, C. Bruske, B. Ecker, U. Eisenbarth, J. Fils, A. Frank, E. Gaul, S. Goette, C. Haefner, T. Hahn, K. Harres, H.-M. Heuck, D. Hochhaus, D.H.H. Hoffmann, D. Javorková, H.-J. Kluge, T. Kuehl, S. Kunzer, M. Kreutz, T. Merz-Mantwill, P. Neumayer, E. Onkels, D. Reemts, O. Rosmej, M. Roth, T. Stoehlker,

- A. Tauschwitz, B. Zielbauer, D. Zimmer, and K. Witte. Commissioning and early experiments of the PHELIX facility. *Applied Physics B*, 100(1):137–150, December 2010.
- [72] Christian Brabetz. Wellenfront Kontrolle am PHELIX-Lasersystem mit adaptiver Optik. Master thesis (Diplomarbeit), Technische Universität Darmstadt, April 2010.
- [73] Bernhard Zielbauer. *Characterization and Optimization of an x-ray laser for spectroscopy of Li-like heavy-ions*. PhD thesis, Johannes Gutenberg Universität Mainz, October 2007.
- [74] Boris Ecker. Aufbau eines kompakten Röntgenlasers. Master thesis (Diplomarbeit), Johannes Gutenberg Universität Mainz, May 2009.
- [75] T. Heßling, A. Blažević, A. Frank, D. Kraus, M. Roth, G. Schaumann, D. Schumacher, T. Stöhlker, and D. H. H. Hoffmann. Time- and spectrally resolved measurements of laser-driven hohlraum radiation. *Phys. Rev. E*, 84:016412, July 2011.
- [76] A. Frank, A. Blažević, P. L. Grande, K. Harres, T. Heßling, D. H. H. Hoffmann, R. Knobloch-Maas, P. G. Kuznetsov, F. Nürnberg, A. Pelka, G. Schaumann, G. Schiwietz, A. Schökel, M. Schollmeier, D. Schumacher, J. Schütrumpf, V. V. Vatulín, O. A. Vinokurov, and M. Roth. Energy loss of argon in a laser-generated carbon plasma. *Phys. Rev. E*, 81:026401, February 2010.
- [77] F. Wagner, C.P. João, J. Fils, T. Gottschall, J. Hein, J. Körner, J. Limpert, M. Roth, T. Stöhlker, and V. Bagnoud. Temporal contrast control at the phelix petawatt laser facility by means of tunable sub-picosecond optical parametric amplification. *Applied Physics B*, 116:429–435, November 2013.
- [78] H. W. Babcock. The possibility of compensating astronomical seeing. *Publications of the Astronomical Society of the Pacific*, 65(386):229–236, October 1953.

- [79] Eugenie Dalimier and Chris Dainty. Comparative analysis of deformable mirrors for ocular adaptive optics. *Opt. Express*, 13(11):4275–4285, May 2005.
- [80] R. Kodama, Y. Sentoku, Z. L. Chen, G. R. Kumar, S. P. Hatchett, Y. Toyama, T. E. Cowan, R. R. Freeman, J. Fuchs, Y. Izawa, M. H. Key, Y. Kitagawa, K. Kondo, T. Matsuoka, H. Nakamura, M. Nakatsutsumi, P. A. Norreys, T. Norimatsu, R. A. Snavely, R. B. Stephens, M. Tampo, K. A. Tanaka, and T. Yabuuchi. Plasma devices to guide and collimate a high density of mev electrons. *Nature*, 432(7020):1005–1008, December 2004.
- [81] Galina Machavariani, Nir Davidson, Erez Hasman, Shmuel Blit, Amiel A. Ishaaya, and Asher A. Friesem. Efficient conversion of a gaussian beam to a high purity helical beam. *Optics Communications*, 209(4-6):265 – 271, August 2002.
- [82] B. Dromey, C. Bellei, D.C. Carroll, R.J. Clarke, J.S. Green, S. Kar, S. Kneip, K. Markey, S.R. Nagel, L. Willingale, P. McKenna, D. Neely, Z. Najmudin, K. Krushelnick, P.A. Norreys, and M. Zepf. Third harmonic order imaging as a focal spot diagnostic for high intensity laser-solid interactions. *Laser and Particle Beams*, 27(02):243–248, 2009.
- [83] B. Dromey, S. Kar, C. Bellei, D. C. Carroll, R. J. Clarke, J. S. Green, S. Kneip, K. Markey, S. R. Nagel, P. T. Simpson, L. Willingale, P. McKenna, D. Neely, Z. Najmudin, K. Krushelnick, P. A. Norreys, and M. Zepf. Bright multi-keV harmonic generation from relativistically oscillating plasma surfaces. *Phys. Rev. Lett.*, 99(8):085001–, August 2007.
- [84] F. Quéré, C. Thaury, P. Monot, S. Dobosz, Ph. Martin, J.-P. Geindre, and P. Audebert. Coherent wake emission of high-order harmonics from overdense plasmas. *Phys. Rev. Lett.*, 96:125004, March 2006.
- [85] M. J. V. Streeter, P. S. Foster, F. H. Cameron, M. Borghesi, C. Brenner, D. C. Carroll, E. Divall, N. P. Dover, B. Dromey, P. Gallegos, J. S. Green, S. Hawkes, C. J. Hooker, S. Kar, P. McKenna, S. R. Nagel, Z. Najmudin,

- C. A. J. Palmer, R. Prasad, K. E. Quinn, P. P. Rajeev, A. P. L. Robinson, L. Romagnani, J. Schreiber, C. Spindloe, S. Ter-Avetisyan, O. Tresca, M. Zepf, and D. Neely. Relativistic plasma surfaces as an efficient second harmonic generator. *New Journal of Physics*, 13(2):023041, February 2011.
- [86] S. V. Bulanov, N. M. Naumova, and F. Pegoraro. Interaction of an ultrashort, relativistically strong laser pulse with an overdense plasma. *Physics of Plasmas*, 1(3):745–757, March 1994.
- [87] R. Lichters, J. Meyer ter Vehn, and A. Pukhov. Short-pulse laser harmonics from oscillating plasma surfaces driven at relativistic intensity. *Physics of Plasmas*, 3(9):3425–3437, September 1996.
- [88] C. Thaury, F. Quéré, J.-P. Geindre, A. Levy, T. Ceccotti, P. Monot, M. Bougeard, F. Reau, P. d’Oliveira, P. Audebert, R. Marjoribanks, and Ph. Martin. Plasma mirrors for ultrahigh-intensity optics. *Nat Phys*, 3(6):424–429, June 2007.
- [89] S. Misra and S. K. Mishra. Focusing of dark hollow gaussian electromagnetic beams in a plasma with relativistic-ponderomotive regime. *Progress in Electromagnetics Research B*, 16:291–309, 2009.
- [90] M.S. Sodha, S.K. Mishra, and S. Misra. Focusing of dark hollow gaussian electromagnetic beams in a plasma. *Laser and Particle Beams*, 27(01):57–68, November 2009.
- [91] A. Sharma, S. Misra, S. K. Mishra, and I. Kourakis. Dynamics of dark hollow gaussian laser pulses in relativistic plasma. *Phys. Rev. E*, 87(6):063111–, June 2013.
- [92] Diana Jahn. Spektrale Untersuchung der heißen Elektronen bei der Laser-Teilchen-Beschleunigung. Bachelor thesis, Technische Universität Darmstadt, Germany, November 2013.
- [93] Tomohiro Suzuki, Chizuo Mori, Katsuo Yanagida, Akira Uritani, Hiroshi Miyahara, Kenji Takahashi, Junji Miyahara, Makoto Yoshida, and Fumiaki Takahashi. Characteristics of prompt scintillation from imaging



- plate. *Nuclear Instruments and Methods in Physics Research Section A: Accelerators, Spectrometers, Detectors and Associated Equipment*, 390(1-2):155–159, 1997.
- [94] Sabine Reinhardt. *Detection of laser-accelerated protons*. PhD thesis, Ludwig-Maximilians-Universität München, June 2012.
- [95] Azam Niroomand-Rad, Charles Robert Blackwell, Bert M. Coursey, Kenneth P. Gall, James M. Galvin, William L. McLaughlin, Ali S. Meigooni, Ravinder Nath, James E. Rodgers, and Christopher G. Soares. Radiochromic film dosimetry: Recommendations of aapm radiation therapy committee task group 55. *Medical Physics*, 25(11):2093–2115, 1998.
- [96] William L. McLaughlin, Mohamad Al-Sheikhly, D. F. Lewis, A. Kovács, and L. Wojnárovits. *Radiochromic Solid-State Polymerization Reaction*, chapter 12, pages 152–166. American Chemical Society, 1996.
- [97] D. S. Hey, M. H. Key, A. J. Mackinnon, A. G. MacPhee, P. K. Patel, R. R. Freeman, L. D. Van Woerkom, and C. M. Castaneda. Use of gafchromic film to diagnose laser generated proton beams. *Review of Scientific Instruments*, 79(5):–, May 2008.
- [98] Joseph S. Cowan, Kirk A. Flippo, and Sandrine A. Gaillard. Characterization of radiochromic film scanning techniques used in short-pulse-laser ion acceleration. *Review of Scientific Instruments*, 79(10):–, October 2008.
- [99] Frank Nürnberg. Vollständige Rekonstruktion und Transportsimulation eines laserbeschleunigten Protonenstrahls unter Verwendung von mikrostrukturierten Targetfolien und radiochromatischen filmdetektoren. Master thesis (Diplomarbeit), Technische Universität Darmstadt, Germany, November 2006.
- [100] Antje Schreiber. RGB-Farb-Kalibrierung von radiochromatischen Filmen. Bachelor thesis, Technische Universität Darmstadt, Germany, September 2012.

- [101] Daniel Kirby. *Radiation dosimetry of conventional and laser-driven particle beams*. PhD thesis, University of Birmingham, April 2011.
- [102] M. I. K. Santala, M. Zepf, F. N. Beg, E. L. Clark, A. E. Dangor, K. Krushelnick, M. Tatarakis, I. Watts, K. W. D. Ledingham, T. McCanny, I. Spencer, A. C. Machacek, R. Allott, R. J. Clarke, and P. A. Norreys. Production of radioactive nuclides by energetic protons generated from intense laser-plasma interactions. *Applied Physics Letters*, 78(1):19–21, January 2001.
- [103] I. Spencer, K.W.D. Ledingham, R.P. Singhal, T. McCanny, P. McKenna, E.L. Clark, K. Krushelnick, M. Zepf, F.N. Beg, M. Tatarakis, A.E. Dangor, P.A. Norreys, R.J. Clarke, R.M. Allott, and I.N. Ross. Laser generation of proton beams for the production of short-lived positron emitting radioisotopes. *Nuclear Instruments and Methods in Physics Research Section B: Beam Interactions with Materials and Atoms*, 183(3-4):449 – 458, 2001.
- [104] M. M. Günther, A. Britz, R. J. Clarke, K. Harres, G. Hoffmeister, F. Nürnberg, A. Otten, A. Pelka, M. Roth, and K. Vogt. Nais: Nuclear activation-based imaging spectroscopy. *Review of Scientific Instruments*, 84(7):–, 2013.
- [105] H. Alva, H. Mercado-Uribe, M. Rodríguez-Villafuerte, and M. E. Brandan. The use of a reflective scanner to study radiochromic film response. *Physics in Medicine and Biology*, 47(16):2925, August 2002.

---

## Publications

---

- C. Brabetz, U. Eisenbarth, O. Kester, T. Stöhlker, T. Cowan, B. Zielbauer, V. Bagnoud, *Hollow Beam creation with continuous diffractive phase mask at PHELIX*, in Conference on Lasers and Electro-Optics 2012, OSA Technical Digest (Optical Society of America, 2012), paper JTu1K.5.
- U. Eisenbarth, C. Brabetz, C. Lempa, T. Stöhlker, V. Bagnoud, *Reference free focal spot optimization of a petawatt laser using adaptive optics*, in Conference on Lasers and Electro-Optics 2012, OSA Technical Digest (online) (Optical Society of America, 2012), paper CM4D.7.
- V. Bagnoud, C. Brabetz, B. Zielbauer, G. Scott, H. Powell, D. Neely, *Far-field characteristics of a petawatt-class laser using plasma mirrors*, in 2013 Conference on Lasers and Electro-Optics - International Quantum Electronics Conference, (Optical Society of America, 2013), paper CG P 8.
- G.G. Scott, J.S. Green, A.P.L. Robinson, C. Spindloe, D. Neely, D.C. Carroll, D.A. MacLellan, P. McKenna, V. Bagnoud, C. Brabetz, B. Zielbauer, F. Wagner, M. Roth, *Plasma cavity enhanced ion acceleration*, Plasma Science (ICOPS), 2012 IEEE International Conference on , pp.5C-4,5C-4
- G. G. Scott, J. S. Green, V. Bagnoud, C. Brabetz, C. M. Brenner, D. C. Carroll, D. A. MacLellan, A. P. L. Robinson, M. Roth, C. Spindloe, F. Wagner, B. Zielbauer, P. McKenna, D. Neely, *Multi-pulse enhanced laser ion acceleration using plasma half cavity targets*, Applied Physics Letters **101**, 024101 (2012)

- P. A. Ni, S. M. Lund, C. McGuffey, N. Alexander, B. Aurand, J. J. Barnard, F. N. Beg, C. Bellei, F. M. Bieniosek, C. Brabetz, R. H. Cohen, J. Kim, P. Neumayer, M. Roth, B. G. Logan, *Initial experimental evidence of self-collimation of target-normal-sheath-accelerated proton beam in a stack of conducting foils*, *Physics of Plasmas* **20**, 083111 (2013)
- S. Busold, D. Schumacher, O. Deppert, C. Brabetz, S. Frydrych, F. Kroll, M. Joost, H. Al-Omari, A. Blažević, B. Zielbauer, I. Hofmann, V. Bagnoud, T.E. Cowan, M. Roth, M., *Focusing and transport of high-intensity multi-MeV proton bunches from a compact laser-driven source*, *Phys. Rev. ST Accel. Beams* **16**, 101302 (2013)
- S. Busold, A. Almomani, V. Bagnoud, W. Barth, S. Bedacht, A. Blažević, O. Boine-Frankenheim, C. Brabetz, T. Burris-Mog, T.E. Cowan, O. Deppert, M. Droba, H. Eickhoff, U. Eisenbarth, K. Harres, G. Hoffmeister, I. Hofmann, O. Jäckel, R. Jäger, M. Joost, S. Kraft, F. Kroll, M. Kaluza, O. Kester, Z. Lecz, T. Merz, F. Nürnberg, H. Al-Omari, A. Orzhekhovskaya, G. Paulus, J. Polz, U. Ratzinger, M. Roth, G. Schaumann, P. Schmidt, U. Schramm, G. Schreiber, D. Schumacher, T. Stöhlker, A. Tauschwitz, W. Vinzenz, F. Wagner, S. Yaramyshev, B. Zielbauer, *Shaping laser accelerated ions for future applications The LIGHT collaboration*, *Nuclear Instruments and Methods in Physics Research Section A: Accelerators, Spectrometers, Detectors and Associated Equipment*, 740:94-98 (2014).
- O. Deppert et al., in preparation
- C. Brabetz et al., *Hollow Beam creation with continuous diffractive phase mask at PHELIX*, GSI scientific report 2011, GSI Darmstadt (2012)
- C. Brabetz et al., *Hollow Beam creation with continuous diffractive phase mask at PHELIX*, GSI scientific report 2012, GSI Darmstadt (2013)
- C. Brabetz et al., *Laser-driven ion acceleration with a hollow beam at PHELIX*, GSI scientific report 2013, GSI Darmstadt (2014), in preparation

## Erklärung zur Dissertation

Ich versichere, dass ich diese Arbeit selbständig und nur unter Verwendung der angegebenen Quellen und Hilfsmittel angefertigt und die den benutzten Quellen wörtlich oder inhaltlich entnommenen Stellen als solche kenntlich gemacht habe. Diese Arbeit hat in gleicher oder ähnlicher Form noch keiner anderen Prüfungsbehörde vorgelegen.

Frankfurt, 2014

---

Christian Gregor Brabetz